JETP Letters, Vol. 81, No. 6, 2005, pp. 241–244. Translated from Pis'ma v Zhurnal Éksperimental'noĭ i Teoreticheskoĭ Fiziki, Vol. 81, No. 6, 2005, pp. 305–308.

Detection of Parametric X-ray Radiation from Moderately Relativistic Protons in Crystals

Yu. N. Adishchev[2], A. S. Artemov[1], S. V. Afanasiev[1], V. V. Boĭko[3], M. A. Voevodin[1], V. I. Volkov[1], A. S. Gogolev[2], V. N. Zabaev[2], A. N. Efimov[1], Yu. V. Efremov[3], A. D. Kovalenko[1], Yu. L. Pivovarov[2], A. P. Potylitsyn[2], S. V. Romanov[1], Sh. Z. Saĭfulin[1], E. A. Silaev[3], A. M. Taratin[1], S. P. Timoshenkov[4], and S. R. Uglov[2]

[1] *Joint Institute for Nuclear Research, Dubna, Moscow region, 141980 Russia*

e-mail: taratin@sunhe.jinr.ru

[2] *Nuclear Physics Institute, Tomsk Polytechnic University, pr. Lenina 2a, Tomsk, 634050 Russia*

[3] *Institute of Physico-Technical Problems, Dubna, Moscow region, 141980 Russia*

[4] *Moscow State Institute of Electronic Engineering (Technical University), Zelenograd, Moscow region, 124498 Russia*

Received February 10, 2005

The spectral maxima of parametric x-ray radiation that are emitted by moderately relativistic protons interacting with various crystals have been detected. The spectral positions of these maxima depend on the crystal orientation angle and they are consistent with the theoretical values. The measurements were carried out with silicon and graphite crystals on the 5-GeV proton beam extracted from the Nuclotron at the Laboratory of High Energies, JINR. © *2005 Pleiades Publishing, Inc.*

PACS numbers: 78.70.–g

Parametric x-ray radiation (PXR) is emitted by fast charged particles in crystals due to the diffraction of the virtual-photon field of a fast charged particle on crystallographic planes. After theoretical predictions [1–3], PXR has been detected and investigated on electron beams of various energies [4, 5].

The characteristics of PXR from the charged particle in a crystal are determined by its velocity v and they are independent of the sign of the charge and mass of the particle. The intensity of PXR must increase as Z^2 with the charge number Z of the particle [6]. The verification of these conclusions of the theory of PXR is the aim of these and designed experiments on beams of relativistic nuclei.

The energy of PXR photons is given by the expression [7]

$$E_n = n\frac{2\pi\hbar c}{d}\frac{\beta\sin\theta_B}{1-\sqrt{\varepsilon}\beta\cos\theta_D\cos\theta_y}, \qquad (1)$$

where n is the diffraction order, d is the interplanar distance, θ_B is the angle of the orientation of the crystal plane with respect to the particle velocity (see Fig. 1), θ_D and θ_y are the radiation-detection angles, $\beta = v/c$, and ε is the dielectric constant of the target material. The detector is placed at angle θ_D in the diffraction plane and is shifted by angle θ_y in the plane that is perpendicular to the diffraction plane. The diffraction plane is determined by the particle momentum and normal vector to the crystal planes. For ultrarelativistic particles ($\beta \approx 1$) in the x-ray frequency range ($\varepsilon \approx 1$), formula (1) coincides with high accuracy with the Bragg relation for the diffraction of real photons in the crystal.

The only attempt to investigate PXR from heavy charged particles was carried out in 1992 on the 70-GeV proton beam at IHEP [8]. However, since the energy resolution of the scintillation detector that was used for spectral measurements was low, a PXR line in the radiation spectrum could not be detected. Nevertheless, the dependence observed in the integral yield of radiation in the energy range under consideration on the

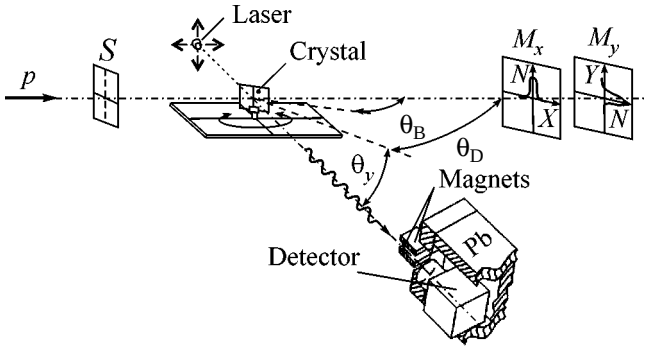

Fig. 1. Layout of the experiment: S is the ionization monitor of the beam, M_x and M_y are the ionization profilometers of the beam, θ_B is the crystal orientation angle, and θ_D and θ_y are the detection angles.

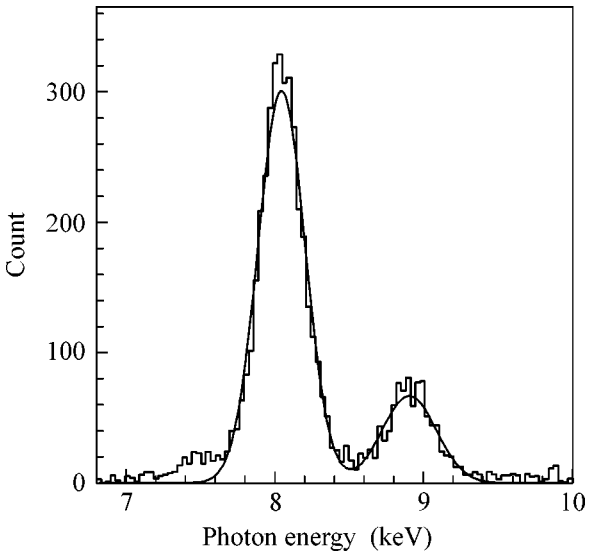

Fig. 2. Calibration spectrum with the peaks of the characteristic copper radiation that is excited in a copper target by a proton beam. The line is the approximation by the sum of two Gaussians.

photon emission angle was attributed by the authors of that work to the detection of proton PXR.

In this paper, we present conclusive evidence for the existence of PXR from heavy particles. The PXR lines have been detected in spectra from relativistic protons. The measurements were carried out on the 5-GeV proton beam from the Nuclotron at the Laboratory of High Energies, JINR.

Figure 1 shows the layout of the experiment. The proton beam was incident on the crystal whose large face was inclined to the beam axis at the angle θ_B = 22.5°. The large face of the crystal was parallel to the close-packed crystallographic planes. The crystal was placed vertically. Hence, the diffraction plane is horizontal. Photons of arising PXR were detected by a silicon detector that was placed at an angle of $\theta_D = 2\theta_B$ = 45° and a horizontal distance of L = 480 mm from the target. In addition, the detector was displaced downward from the diffraction plane by 72 mm in order to be at the maximum of the angular distribution of PXR. This maximum is displaced from the diffraction plane by an angle of $\theta_y = 1/\gamma = 0.158$, where γ is the proton relativistic factor. The working area of the detector was equal to 12 mm^2. The experiment was carried out in Bragg geometry.

The beam incident on the crystal was monitored by the ionization chamber *S*. The distribution of particles in the beam was measured by the ionization profile meters M_x and M_y. The characteristic sizes of the beam were σ_x = 3 mm and σ_y = 6 mm. At the beginning of the measurements, targets that were composed of thin aluminum and polyethylene plates were irradiated at the place of the crystal and the ionization chamber. The ionization monitor was calibrated by measuring the radioactivity induced in the targets.

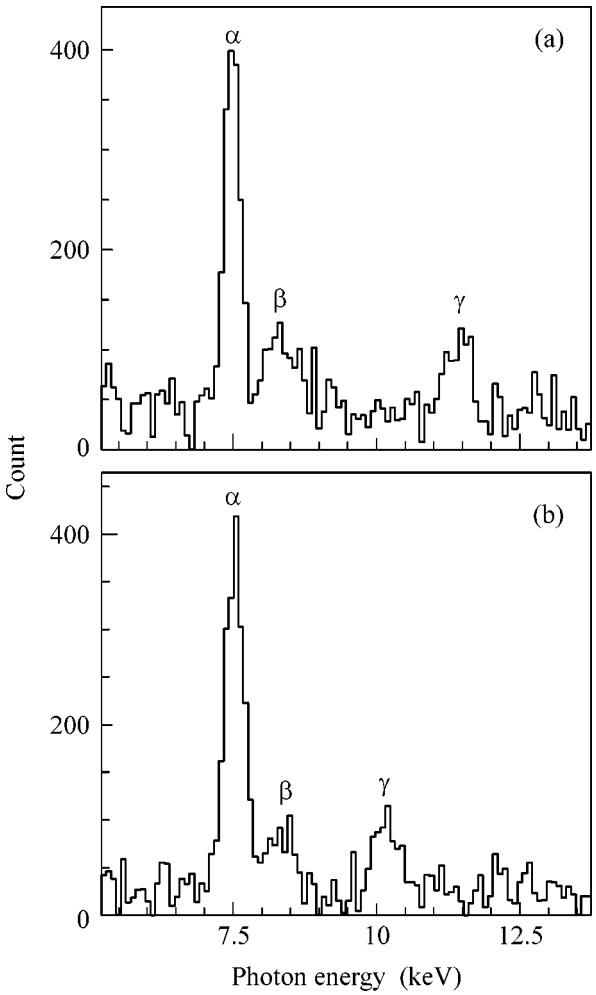

Fig. 3. Radiation spectra measured from the proton beam interacting with the (100) silicon crystal for the orientation angles θ_B = (a) 22.5° and (b) 20°.

The semiconductor detector was calibrated by using the lines of characteristic radiation excited in the copper target by the proton beam. Figure 2 shows the measured spectrum of the characteristic radiation of copper atoms. The distribution was approximated by the sum of two Gaussians. The energy resolution of the detector in the experiment for the 8.046-keV K_α line (first peak) of the characteristic radiation of copper was approximately equal to 320 eV (the energy width of the spectrometer channel was 10.67 eV).

Figure 3 shows the measured radiation spectra from the proton beam interacting with a (100) silicon crystal in the form of a circular plate 100 mm in diameter and 300 μm thick. The silicon crystalline samples that were used in the experiment were manufactured and tested at the Moscow State Institute of Electronic Engineering (Technical University). The peaks α (E_α = 7.48 keV) and β (E_β = 8.26 keV) in Fig. 3 correspond to the char-

acteristic radiation of nickel atoms that were excited in the detector case by the particles of the beam halo (protons that are scattered in matter along the transportation section and secondary particles). Figure 3a corresponds to the symmetric case $\theta_B = 0.5\theta_D = 22.5°$. The position $E_\gamma = 11.4$ keV of the peak γ is consistent with the value $E_1 = 11.15$ keV calculated by formula (1). Therefore, the peak it corresponds to proton PXR on the (400) plane of silicon. As was expected according to Eq. (1), the PXR line is shifted toward the softer range as the crystal orientation angle decreases (cf. Fig. 3b for $\theta_B = 20°$). For Fig. 3b, $E_\gamma = 10.21$ keV, and the calculated value is equal to 9.96 keV. The yield of PXR from the silicon crystal is equal to 2.25×10^{-6} and 2.05×10^{-6} photons/(proton sr), respectively. These values were obtained from the spectra after recalculation in which the attenuation of radiation on the path to the detector and the efficiency of the detector were taken into account. These values are approximately half the theoretical estimates of the PXR yield [7]. The total error that is primarily determined by the performance of the spectrometer is estimated as 40%.

In [9], PXR was measured from a 4-MeV electron beam interacting with a silicon crystal 20 μm thick. In that work, the electron relativistic factor $\gamma_e = 8.83$ was close to the value $\gamma_p = 6.33$ for protons in our case, the angles of the crystal orientation and radiation detection approximately corresponded to the respective angles in our case, but that experiment was carried out in Laue geometry that differed from the geometry of our experiment. The (110) crystallographic planes on which the virtual-photon field of the particles was diffracted were perpendicular to the large faces of the crystal. In the experiment described in [9], the yield of electron PXR that was measured at the maximum and that included a small contribution from coherent bremsstrahlung and their interference was equal to 5×10^{-6} photon/(electron sr). This yield is more than twice as large as the yield of proton PXR in our experiment. Since the conditions for the two experiments were significantly different, the above comparison is only provisional.

The width of the peaks that were measured for PXR exceeds the detector resolution and it is determined by the transverse size of the proton beam on the target, because the detector is placed quite closely to the target.

Figure 4 shows the radiation spectra measured on the 20×30-mm pyrolytic graphite crystal with a thickness of 2 mm and a mosaicity angle of about 0.4°. Here, α and β are also the peaks of the characteristic radiation of nickel atoms in the detector case. In the symmetric case (Fig. 4a), the peak γ at $E_\gamma = 9.5$ keV corresponds to the second-order maximum of proton parametric radiation on the (002) planes of graphite. Radiation corresponding to the first order of diffraction ($E_1 = 4.51$ keV) is absorbed in the air on the path to the detector. To observe the shift of the PXR peak, we increased the crystal orientation angle in order to avoid overlapping with the peak β of the characteristic radiation of nickel (see Fig. 4b for $\theta_B = 25°$). For Fig. 4b, $E_\gamma = 10.35$ keV in agreement with the calculated position $E_2 = 9.97$ keV of the PXR line.

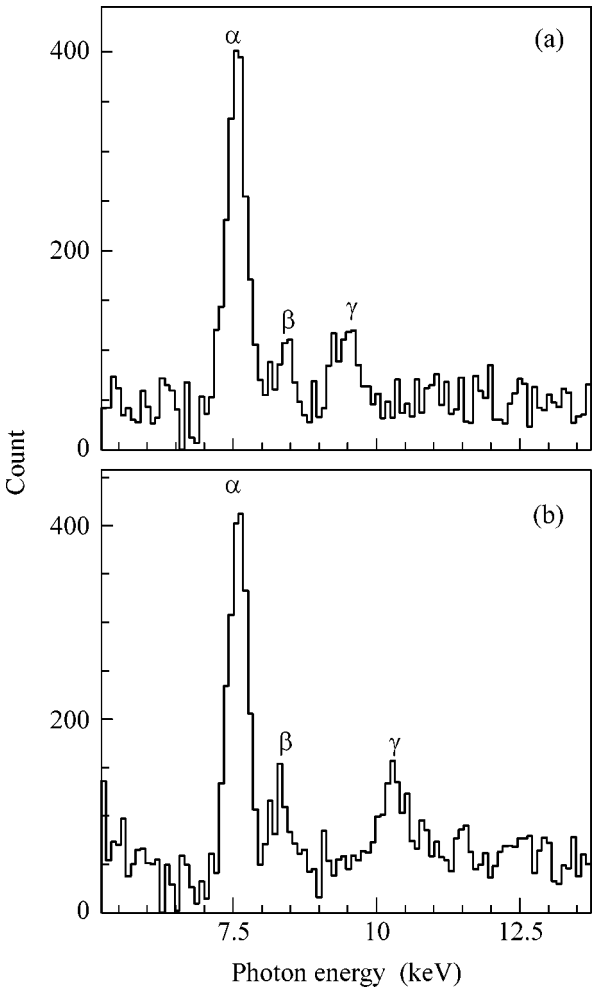

Fig. 4. Radiation spectra measured from the proton beam interacting with the graphite crystal for the orientation angles θ_B = (a) 22.5° and (b) 25°.

The detection of the spectral lines whose positions agree with the calculations for the silicon and graphite crystals, which were investigated for their various orientations in the beam, evidently indicates that PXR from moderately relativistic protons is observed in our experiment. The experimental results corroborate the theoretical conclusion that the spectral characteristics of PXR are independent of the sign of the charge and mass of the particles. The fact that the yield that is measured for PXR is lower than the theoretical estimates and experimental data for electrons [8] can be attributed to uncontrollable miscounts of the detector under high-background conditions.

The PXR yield for protons will be measured more accurately in further experiments. An experiment with

a carbon atomic beam is also designed in order to test the Z^2 dependence of the PXR yield.

We are grateful to I.G. Grigorieva and A.A. Antonov who placed the sample of a high-quality pyrolytic graphite crystal, which was manufactured at Atomgraph AG (www.optigraph.fta-berlin.de), at our disposal and to V.P. Bamblevskiy for measurements of the induced activity of targets irradiated by the proton beam, which were carried out in order to calibrate the ionization monitor. This work was supported in part by the International Science and Technology Center (project no. 2140) and the Russian Foundation for Basic Research (project no. 03-02-17578).

REFERENCES

1. M. L. Ter-Mikaelian, *High Energy Electromagnetic Processes in Condensed Media* (Wiley, New York, 1972; Akad. Nauk Arm. SSR, Yerevan, 1969).
2. G. M. Garibyan and Yan Shi, Zh. Éksp. Teor. Fiz. **61**, 930 (1971) [Sov. Phys. JETP **34**, 1756 (1971)].
3. V. G. Baryshevskiĭ and I. D. Feranchuk, Zh. Éksp. Teor. Fiz. **61**, 947 (1971) [Sov. Phys. JETP **34**, 1778 (1971)].
4. A. V. Schagin and X. K. Maruyama, in *Accelerator-Based Atomic Physics: Technique and Applications*, Ed. by S. M. Shafroth and J. C. Austin (AIP Press, New York, 1997), p. 279.
5. P. Rullhusen, X. Artru, and P. Dhez, *Novel Radiation Sources Using Relativistic Electrons* (World Sci., Singapore, 1998).
6. Yu. L. Pivovarov, Yu. P. Kunashenko, and S. A. Vorobiev, Radiat. Eff. **100**, 51 (1986).
7. H. Nitta, Phys. Rev. B **45**, 7621 (1992).
8. V. P. Afanasenko, V. G. Baryshevsky, R. F. Zuevsky, *et al.*, Phys. Lett. A **170**, 315 (1992).
9. V. V. Morokhovskyi, J. Frendenberger, H. Genz, *et al.*, Phys. Rev. B **61**, 3347 (2000).

Translated by R. Tyapaev

JETP Letters, Vol. 81, No. 6, 2005, pp. 245–248. From Pis'ma v Zhurnal Éksperimental'noĭ i Teoreticheskoĭ Fiziki, Vol. 81, No. 6, 2005, pp. 309–312.

Chiral Symmetry Breaking and Monopole Condensation in QCD¶

M. N. Chernodub [1] and I. E. Kozlov[2]

[1] *Institute of Theoretical and Experimental Physics, Moscow, 117259 Russia*
e-mail: Maxim.Chernodub@itep.ru
[2] *Department of Physics, Moscow State University, Moscow, 119899 Russia*

Received February 14, 2005

We show that, in the dual superconductor picture of the QCD vacuum, the presence of the monopole condensate inevitably leads to the breaking of the chiral symmetry. © *2005 Pleiades Publishing, Inc.*

PACS numbers: 11.30.Rd, 12.38.Aw

The origin of chiral symmetry breaking and the nature of the confinement of color charges are still unresolved puzzles in Quantum Chromodynamics (QCD). Analytical methods based on the perturbation theory cannot describe these phenomena starting from the first principles of the theory. The confinement of quarks is realized as a linear dependence of the interaction energy between a test quark and an antiquark, $V_{q\bar{q}} \sim \sigma R$, on the separation distance R. The coefficient of proportionality, $\sigma \approx 1$ GeV/fm, is called the "string tension." The confinement phenomena indicates its presence at relatively large separations, $R \gtrsim 0.2 \sim 0.3$ fm, where the QCD coupling constant is large and the perturbation theory is not applicable.

On the other hand, the effect of the chiral symmetry breaking involves a formation of the quark condensate, $\langle \bar{\psi}\psi \rangle \approx (250\ \text{MeV})^3$, which is not invariant under the chiral transformations of the quark fields, $\psi \longrightarrow \exp\{i\gamma_5\alpha\}\psi$. Both the chiral condensate and the string tension are dimensional quantities that remain nonzero in the infinitely heavy quark limit ("quenched QCD"). The last fact also illustrates the nonperturbative nature of both confinement and chiral symmetry breaking phenomena.

There are indications that the confinement and the chiral symmetry breaking phenomena are closely related to each other. For example, at sufficiently high temperatures, $T > T_c$, confinement is lost and the QCD goes from the confinement phase into the deconfinement phase. The remarkable fact is that the chiral symmetry is restored exactly at the same temperatures, $T > T_c$. Below, we discuss the relation between these phenomena within the so-called dual superconductor model of confinement.

The dual superconductor mechanism [1] of the quark confinement is based on specific monopole-like configurations of the gluonic fields. The configurations—called "Abelian monopoles"—can be identified in appropriate Abelian gauges [2]. In an Abelian gauge, the non-Abelian gauge symmetry of the QCD, which is given by the SU(3) gauge group, is fixed to an Abelian subgroup. Since the original SU(3) gauge group is compact, the residual Abelian symmetry group is compact as well. The compactness of the Abelian group guarantees the appearance of the monopoles in the vacuum of the theory.

According to the dual superconductor mechanism, the quark confinement in the low temperature phase, $T < T_c$, of the four dimensional SU(3) gauge model appears due to the condensation of the Abelian monopoles. The condensation of magnetic charges leads to the dual Meissner effect and, as a result, to the formation of the chromoelectric string between the quarks. Consequently, the quarks get confined by the string. The condensation of the monopoles was established in various numerical simulations of non-Abelian models [3]. Moreover, the Abelian monopoles make a dominant contribution to the zero temperature string tension [4] (for a review, see [5]).

At the critical temperature, the monopole condensate disappears and at higher temperatures the quarks are no longer confined. The restoration of the chiral symmetry at $T = T_c$ suggests that the chiral condensate and the monopole condensate are tightly related to each other. Numerical simulations suggest that the monopoles provide a dominant contribution to the chiral condensate in various models [6, 7]. Moreover, the monopoles are correlated with the topological charge[1] [8],

¶ This article was submitted by the authors in English.

[1] Note that the ensemble of instantons (i.e., of classical objects having a nonzero topological charge) can be used to explain the breaking of the chiral symmetry. Since the QCD instantons fail to explain the quark confinement, we do not discuss them in this paper.

0021-3640/05/8106-0245$26.00

which is known to be related to the breaking of the chiral symmetry.

The dual superconductor model for QCD is described by the Lagrangian [9]

$$\begin{aligned} L_{DGL} &= -\frac{1}{2}([n\cdot(\partial\wedge\mathbf{A})]^{\nu}[n\cdot{}^*(\partial\wedge\mathbf{B})]_{\nu} \\ &+ [n\cdot(\partial\wedge\mathbf{B})]^{\nu}[n\cdot{}^*(\partial\wedge\mathbf{A})]_{\nu} - [n\cdot(\partial\wedge\mathbf{A})]^2 \\ &- [n\cdot(\partial\wedge\mathbf{B})]^2) + \sum_{\alpha=1}^{3}[|(i\partial_\mu - g\epsilon_\alpha\mathbf{B}_\mu)\chi_\alpha|^2 \\ &- \lambda(|\chi_\alpha|^2 - v^2)^2] + \bar\psi(i\partial\!\!\!/ - eA\!\!\!/\cdot\mathbf{H} - m)\psi, \end{aligned} \tag{1}$$

where three monopole fields χ_α with $\alpha = 1, 2, 3$, are interacting with the *dual* gluon fields $\mathbf{B} = (B^3, B^8)$ by the covariant derivative (the root vectors ϵ_α of the $SU(3)$ group are: $\epsilon_1 = (1, 0)$, $\epsilon_2 = (-1/2, -\sqrt{3}/2)$, and $\epsilon_3 = (-1/2, -\sqrt{3}/2)$. The Abelian components of the original gluons, $\mathbf{A} = (A^3, A^8)$, are interacting with the dynamical quark fields ψ. The diagonal generators of the $SU(3)$ gauge group are denoted as $\mathbf{H} = (H^3, H^8)$. The magnetic (electric) charge of the monopole (quark) is e (g).

The interaction of the dual gauge field with the original gauge field is described by the Zwanziger Lagrangian [10] (the first line of Eq. (1)). The constant vector n_μ (with $n_\mu^2 = 1$) does not break the Lorentz symmetry on a quantum level provided the Dirac quantization condition, $eg = 2\pi$, is satisfied. Note that, in the Lagrangian (1), the off-diagonal components of the gluon field were ignored due to the Abelian dominance observed both for the confining [4] and the chiral properties of the vacuum [7].

In the confinement phase, the monopole condensate, $|\langle\chi_\alpha\rangle| = v$, is nonzero. Consequently, the dual gauge field $\mathbf{B}_\mu$ acquires the mass, $M_B = vg$, due to spontaneous breaking of the dual $U(1)\times U(1)$ symmetry. In order to simplify the calculations, let us consider the mean field approximation by setting $\chi_\alpha = v$. Then, the Lagrangian becomes quadratic in the gauge fields, and the integration over the dual gauge field $\mathbf{B}_\mu$ in the corresponding partition function can be performed exactly:

$$\begin{aligned} L_{DGL-mf} &= -\frac{1}{4}\mathbf{f}_{\mu\nu}\mathbf{f}^{\mu\nu} \\ &+ \frac{1}{2}\mathbf{A}^{\mu}K_{\mu\nu}\mathbf{A}^{\nu} + \bar\psi(i\partial\!\!\!/ - eA\!\!\!/\cdot\mathbf{H} - m)\psi, \end{aligned} \tag{2}$$

where $K^{\mu\nu} = M_B^2 X^{\mu\nu}/[(n\partial)^2 + M_B^2]$ and $X^{\mu\nu} = \epsilon_\lambda^{\mu\alpha\beta}\epsilon^{\lambda\nu\gamma\delta}n_\alpha n_\gamma\partial_\beta\partial_\delta$. One can see that, if the monopole condensate is absent, $v = 0$; then, $M = 0$ and the model becomes equivalent to $U(1)\times U(1)$ electrodynamics.

In the Lorentz-type gauge with the gauge fixing Lagrangian $L_{gf}(A) = (\partial_\mu\mathbf{A}^\mu)^2/2\xi$, the propagator of the gauge field A_μ is the following:

$$\begin{aligned} D_{\mu\nu} &= \frac{1}{\partial^2}\left\{g_{\mu\nu} + (\xi-1)\frac{\partial_\mu\partial_\nu}{\partial^2}\right\} \\ &- \frac{1}{\partial^2}\frac{M_B^2}{\partial^2 + M_B^2}\frac{1}{(n\partial)^2}X_{\mu\nu}. \end{aligned} \tag{3}$$

The interaction Lagrangian of the fermion fields can be calculated exactly from Eq. (2) by the Gaussian integration of the gauge field $\mathbf{A}_\mu$:

$$\begin{aligned} L_{\rm ferm}(\bar\psi,\psi) &= \bar\psi(i\partial\!\!\!/ - m)\psi - \frac{1}{2}\mathbf{j}_\mu D^{\mu\nu}\mathbf{j}_\nu, \\ \mathbf{j}_\mu &= ie\bar\psi\gamma_\mu\mathbf{H}\psi. \end{aligned} \tag{4}$$

This Lagrangian contains a free (quadratic) part and the four-fermion interaction term similarly to the Nambu–Jona–Lasinio (NJL) model. In the NJL-type models, the chiral (quark) condensate appears naturally. However, the presence or absence of the quark condensate depends on the particular form of the four-fermion interaction. In our model (4), the interaction term and, consequently, the properties of the chiral condensate depend on the value of the monopole condensate v.

Another simplification of our considerations comes from the fact that the Lagrangian (4) is invariant under the global color rotations of the fermionic triplet $\psi \equiv (\psi_1, \psi_2, \psi_3)$, which implies that $\langle\bar\psi_i\psi_j\rangle = \langle\bar\psi\psi\rangle\delta_{ij}/3$. Thus, below, we consider only one component of the quark field, the dynamics of which are described by the Lagrangian (4)—in which ψ has only one component—with the simple redefinition $e^2 \longrightarrow e^2\mathbf{H}^2 \equiv e^2/3$.

The breaking of the chiral symmetry can be conveniently investigated with the help of the generating functional

$$Z[\bar\eta,\eta] = \frac{\int \mathrm{D}\bar\psi\mathrm{D}\psi e^{-S[\bar\psi,\psi] + \int d^4x(\bar\eta\psi + \bar\psi\eta)}}{\int \mathrm{D}\bar\psi\mathrm{D}\psi e^{-S[\bar\psi,\psi]}}, \tag{5}$$

where η and $\bar\eta$ are external fermionic fields and the quark action S corresponds to Lagrangian (4).

Thus, the knowledge of the generating functional (5) allows us to find the existence of the chiral condensate, $\langle\bar\psi(x)\psi(x)\rangle = \delta^2/(\delta\eta(x)\delta\bar\eta(x))\log Z[\bar\eta,\eta]|_{\bar\eta=\eta=0}$, and, as a result, the existence of the chiral symmetry breaking.

In order to integrate over the fermionic fields in (5), we use the method proposed in Ref. [11]. First, we use the Fierz identities to write

$$(\gamma_\mu)_{rs}D_{\mu\nu}(x;\xi)(\gamma_\nu)_{tu}$$

$$= [\delta_{ru}\delta_{ts} + (i\gamma_5)_{ru}(i\gamma_5)_{ts}]\delta_{\mu\nu}D_{\nu\mu}(x;\xi)/4$$
$$+ [(i\gamma_\mu)_{ru}(i\gamma_\nu)_{ts} + (i\gamma_\mu\gamma_5)_{ru}(i\gamma_\nu\gamma_5)_{ts}]\tilde{D}_{\mu\nu}(x;\xi) \quad (6)$$
$$+ [(\Sigma_{\rho\mu})_{ru}(\Sigma_{\rho\nu})_{ts} + (i\gamma_5\Sigma_{\rho\mu})_{ru}(i\gamma_5\Sigma_{\rho\nu})_{ts}]\tilde{D}_{\mu\nu}(x;\xi)$$
$$\equiv \sum_\Delta ((K^\Delta)_{ru}, D^\Delta(x-y;\xi)(K^\Delta)_{ts}).$$

The definitions of the basis forms, K^Δ, and the propagators, $\tilde{D}$, are obvious. The indices $\Delta = S, P, V, A, T,$ and AT correspond, respectively, to the scalar, pseudoscalar, vector, tensor, and pseudotensor: $(K^S)_{ru} = \delta_{ru}$, $(K^P)_{ru} = (i\gamma_5)_{ru}$, etc.

Introducing the nonlocal hermitian variables, $[\beta(x, y)]^+ = [\beta(y, x)]$, we multiply the nominator and denominator of Eq. (5) by $\int D\beta \exp\left\{-\frac{1}{2}e^2\sum_\Delta(\beta^\Delta(y, x), D^\Delta(x-y;\xi)\beta^\Delta(x, y))\right\}$. Next, we perform the shift $\beta^\Delta(x, y) \longrightarrow \beta^\Delta(x, y) + \bar{\psi}(y)K^\Delta\psi(x)$ in the denominator of the obtained expression. The Jacobean of such a shift is unity. After the shift is preformed, the integration over the fermionic fields ψ can be taken in the explicit form:

$$Z[\bar{\eta}, \eta] = [\int D\beta \exp(-S_{\text{eff}}[\beta])]^{-1}$$
$$\times \int D\beta \exp\{-S_{\text{eff}}[\beta] + \int d^4x d^4y \bar{\eta}(x)G(x, y; [\beta])\eta(y)\}, \quad (7)$$

where the action for the variables β reads as follows:

$$S_{\text{eff}}[\beta] = -\text{TrLog}[(G^{-1})(x, y; [\beta])]$$
$$+ \frac{e^2}{2}\sum_\Delta(\beta^\Delta(y, x), D^\Delta(x-y;\xi)\beta^\Delta(x, y)). \quad (8)$$

The definition of $G(x, y; [\beta])$ is $(G^{-1})(x, y; [\beta]) = (\gamma\cdot\partial)\delta^4(x-y) + \Sigma(x, y; [\beta])$, where the quantity $\Sigma(x, y; [\beta]) = \sum_\Delta(\beta^\Delta(y, x), D^\Delta(x-y;\xi)K^\Delta(x, y))$ can be interpreted as a self-energy because $\langle\bar{\psi}(x)\psi(y)\rangle \equiv \langle G(x, y; [\beta])\rangle$.

We evaluate the functional (7), (8) by the saddle-point method. The stationary point is given by the equations

$$\beta^{S,P}(x, y) = \text{tr}[K^{S,P}G(x, y; [\beta])],$$
$$\beta_\nu^{V,A}(x, y) = \text{tr}[K_\nu^{V,A}G(x, y; [\beta])], \quad (9)$$
$$\beta_{\mu\nu}^T(x, y) = \text{tr}[K_{\mu\nu}^T G(x, y; [\beta])],$$

which are then multiplied by the corresponding matrices K^Δ and functions D^Δ. Summing them up over Δ and the vector indices, we get an equation (in momentum space) for the self-energy Σ in the matrix form:

$$\Sigma(\bar{p}, [\beta]) = e^2\int\frac{d^4\bar{q}}{(2\pi)^4}D_{\mu\nu}(\bar{p}-\bar{q})\gamma_\mu\frac{1}{i(\gamma\bar{q}) + \Sigma(\bar{q}, [\beta])}\gamma_\nu. \quad (10)$$

We choose the following anzatz for the solution:

$$\Sigma(\bar{p}, [\beta]) = i[A(\bar{p}) - 1](\gamma\bar{p}) + iC(\bar{p})(\gamma\bar{n}) + e^{i\gamma_5\theta}B(\bar{p}). \quad (11)$$

Here, $\bar{p} = (p_0, p_1, p_2, p_3)$ and the arbitrary functions A, B, and C depend on $\bar{p}^2$ and $(\bar{n}, \bar{p})$: $f(\bar{p}) \equiv f(\bar{p}^2, (\bar{p}, \bar{n}))$.

In the parameterization (11), the first two terms correspond to the chirally invariant vacuum while the third term violates the chiral symmetry. As we show below, there exists a nontrivial solution of Eq. (10) with $B \neq 0$ such that the function B does not depend on the angle θ. Therefore, there exists an infinite set of solutions (for which the effect functional of the theory is the same!) connected to each other by the transformation $B \longrightarrow B'e^{i\gamma^5\varphi}$. This corresponds to the spontaneous breaking of the chiral symmetry.

It is convenient to set $n_\mu = \delta_{\mu,0}$, and separate the integrations in Eq. (10) into "time," q_0, and "space," $\mathbf{q}$, parts. The integral over the angle part of the space momentum can be taken explicitly. The integral over the temporal variable contains a singularity $1/(p_0 - q_0)^2$, which cannot be removed by a choice of the gauge. The singularity appears to be related to the (gauge-variant!) direction of the Dirac line; therefore, this singularity is nonphysical in the sense that it should not contribute to any gauge-invariant quantity.

In order to solve equations (10), we regularize the double pole by the quantity ϵ, which has the dimension of mass, $(p_0 - q_0)^{-2} \longrightarrow [(p_0 - q_0)^2 + \epsilon^2]^{-1}$. This regularization corresponds [6] to the quark–antiquark pair creation from the vacuum and the subsequent flattening of the quark–antiquark potential at the distances $R \gtrsim R_{\text{flat}} \sim \epsilon^{-1}$, which are small compared to the dual penetration depth, M_B^{-1}, of the vacuum. Below, we study the problem in the leading order of the smallness parameter, $M_B/\epsilon \ll 1$.

In the Landau gauge, $\xi = 0$, the saddle-point equations are (all the regions of integration are $(0, \infty)$):

$$\bar{C}(p_0, p) - p_0 = \frac{\tilde{e}^2}{(2\pi)^3}$$
$$\times \int dq q^2 \frac{\bar{C}(p_0, q)}{q^2 + B^2(p_0, q)p_0 + \bar{C}^2(p_0, q)} \quad (12)$$

$$\times \frac{M_B^2}{pq}\log\frac{M_B^2+(p-q)^2}{M_B^2+(p+q)^2},$$

$$B(p_0, p)$$

$$= -\frac{\tilde{e}^2}{(2\pi)^3}\int dq q^2 \frac{B(p_0, p)}{q^2 + B^2(p_0, p^2) + \bar{C}^2(p_0, q)} \qquad (13)$$

$$\times \frac{M_B^2}{pq}\log\frac{M_B^2+(p+q)^2}{M_B^2+(p-q)^2},$$

where $\tilde{e}^2 \equiv \pi e^2/\epsilon$ and $\bar{C}(p_0, p) \equiv A(p_0, p)p_0 + C(p_0, p)$. We also used the fact that $A(p_0, p) = 1 + O((M_B/\epsilon)^4)$, which follows from Eqs. (10), (11).

Equations (12), (13) possess two types of solutions: the chirally invariant solution with $B = 0$ and the chirally broken solution with $B \neq 0$. To discriminate between them, one should compare the corresponding values of the action. The action of a classical solution is given by Eq. (8) evaluated on the anzatz (11)

$$S[A, B, C] = -\mathrm{TrLn}[(\gamma\cdot\partial)A(x-y)$$

$$+ e^{i\gamma_5\theta}B(x-y) + i(\bar{\gamma}\cdot\bar{n})C(x-y)] + \frac{e^2}{2} \qquad (14)$$

$$\times\int d^4x d^4y\{[\beta^S(y, x)\beta^S(x, y) + \beta^P(y, x)\beta^P(x, y)]$$

$$\times\tilde{D}(x-y;\xi) + \beta_\mu^V(y, x)\beta_\nu^V(x, y)\tilde{D}_{\mu\nu}(x-y;\xi)\},$$

where β^Δ are given by Eqs. (9): $Be^{i\gamma_5\theta} = e^2\tilde{D}(\beta^S + i\gamma_5\beta^P)$ and $(\gamma\cdot\partial)(A-\delta^{(4)}) + i(\bar{\gamma}\cdot\bar{n})C = e^2\tilde{D}_{\mu\nu}(i\gamma_\mu)\beta_\nu^V$. The action (14) does not depend on the angle θ.

Up to $O((M_B/\epsilon)^2)$, the corrections of the difference between the actions of $B = 0$ and $B \neq 0$ vacua are

$$\Delta S \equiv S[A_{B=0}, 0, C_{B=0}] - S[A_{B\neq 0}, B, C_{B\neq 0}]$$

$$= \int d^4x\int\frac{d^4p}{(2\pi)^4}\left\{2\log\left(1+\frac{B^2}{\bar{p}^2}\right) - \frac{2B^2}{\bar{p}^2+B^2}\right.$$

$$+ \frac{4C'_{B=0}}{p_0} - \frac{4C'_{B\neq 0}}{p_0}\frac{1}{1+\bar{g}^2B^2} + \frac{2p_0C'_{B=0}}{\bar{p}^2} \qquad (15)$$

$$\left. - \frac{2p_0C'_{B\neq 0}}{\bar{p}^2+B^2} + \frac{4p_0C'_{B\neq 0}B^2}{(\bar{p}^2+B^2)^2}\right\}[1 + O((M_B/\epsilon)^2)],$$

where $\bar{C} = p_0 + C'M_B^2$, and $C_{B=0}$ is a solution of Eq. (12) with $B = 0$, while $C_{B\neq 0}$ is a solution of Eqs. (12), (13). In the absence of the monopole condensate, $M_B^2 = 0$, the difference (15) coincides with the result of the QED [11].

The important fact is that Eq. (12) implies that $C_{B=0} > C_{B\neq 0}$. Therefore, the action difference ΔS is *always* positive due to the presence of the monopole condensate. Moreover, the concrete form of solutions of Eqs. (12), (13) does not influence this conclusion. One can show [12] with the help of both analytical and numerical tools that the $B \neq 0$ solutions of Eqs. (12), (13) do exist. Thus, the presence of the monopole condensate makes the vacuum, which is degenerate in the chiral angle θ, more energetically preferable with respect to the chirally nondegenerate vacuum. Therefore, in the scope of the dual superconductor model of the QCD vacuum, the presence of the monopole condensate implies the chiral symmetry breaking in QCD.

The work of M.N.C. is supported by the Russian Foundation for Basic Research (project no. 04-02-16079) and by the Council of the President of the Russian Federation for Support of Young Russian Scientists and Leading Scientific Schools (project no. MK-4019.2004.2).

REFERENCES

1. G. 't Hooft, *High Energy Physics: EPS International Conference, Palermo, 1975*, Ed. by A. Zichichi (Editrice Compositori, Bolognia, 1976); S. Mandelstam, Phys. Rep. **23**, 245 (1976).
2. G. 't Hooft, Nucl. Phys. B **190**, 455 (1981).
3. N. Nakamura *et al.*, Nucl. Phys. (Proc. Suppl.) **53**, 512 (1997); M. N. Chernodub, M. I. Polikarpov, and A. I. Veselov, Phys. Lett. B **399**, 267 (1997); Nucl. Phys. (Proc. Suppl.) **49**, 307 (1996); A. Di Giacomo and G. Paffuti, Phys. Rev. D **56**, 6816 (1997).
4. T. Suzuki and I. Yotsuyanagi, Phys. Rev. D **42**, 4257 (1990); G. S. Bali *et al.*, Phys. Rev. D **54**, 2863 (1996).
5. T. Suzuki, Nucl. Phys. (Proc. Suppl.) **30**, 176 (1993); M. N. Chernodub and M. I. Polikarpov, in *Confinement, Duality, and Nonperturbative Aspects of QCD*, Ed. by P. van Baal (Plenum, New York, 1998), p. 387; hep-th/9710205; R. W. Haymaker, Phys. Rep. **315**, 153 (1999).
6. H. Suganuma, S. Sasaki, and H. Toki, Nucl. Phys. B **435**, 207 (1995).
7. T. Bielefeld *et al.*, Phys. Lett. B **416**, 150 (1998); R. Wensley, Nucl. Phys. (Proc. Suppl.) **53**, 538 (1997).
8. M. N. Chernodub and F. V. Gubarev, JETP Lett. **62**, 100 (1995); S. Thurner, M. C. Feurstein, and H. Markum, Phys. Rev. D **56**, 4039 (1997); S. Sasaki and O. Miyamura, Phys. Lett. B **443**, 331 (1998).
9. S. Maedan and T. Suzuki, Prog. Theor. Phys. **81**, 229 (1989).
10. D. Zwanziger, Phys. Rev. D **3**, 880 (1971).
11. C. D. Roberts and R. T. Cahill, Phys. Rev. D **33**, 1755 (1986).
12. M. N. Chernodub and I. E. Kozlov (in preparation).

JETP Letters, Vol. 81, No. 6, 2005, pp. 249–254. From Pis'ma v Zhurnal Éksperimental'noĭ i Teoreticheskoĭ Fiziki, Vol. 81, No. 6, 2005, pp. 313–317.

Photon–Neutrino Interactions¶

G. Karl and V. Novikov[1]

Department of Physics, University of Guelph, Ontario, NIG 2W1, Canada
Guelph–Waterloo Physics Institute, Department of Physics, University of Waterloo, Waterloo, Ontario, N2L 3G1, Canada

Received February 24, 2005

We discuss the interaction of photons with neutrinos including two lepton loops. The parity violation in the $\gamma\nu \longrightarrow \gamma\nu$ channel due to two lepton loops is substantially enhanced relative to the one lepton loop contribution. However, there is no corresponding enhancement in the parity conserving amplitude in either the direct or the cross channel $\gamma\gamma \longrightarrow \nu\bar{\nu}$. © *2005 Pleiades Publishing, Inc.*

PACS numbers: 13.15.+g

1. INTRODUCTION AND SUMMARY

The photon–neutrino interaction is very weak, involving only electrically neutral external particles. The cross sections are exceedingly small. Therefore, this interaction can only be of astrophysical interest. Chiu and Morrison [1] proposed long ago that photon conversion to neutrinos may play a role in supernova cooling. Another possible application involves the propagation of light waves through a handed neutrino sea [2], which results in optical activity (birefringence). There may perhaps be effects in the cooling of the early universe. For all these reasons, there has been some small theoretical interest in this interaction [3]. We consider here the interaction at energies that are small compared to the mass of the weak bosons. At these energies, the weak interaction can be described by a Fermi type effective theory. To have $\nu\gamma$ interaction, one needs virtual leptons that couple both weakly and electromagnetically, thus, lepton loops in Feynman graphs. Contrary to intuition, a two loop graph dominates the parity violation. In this section, we summarize our results using only dimensional arguments. A more technical description is in the next sections.

For supernova cooling, the amplitude for the annihilation $\gamma\gamma \longrightarrow \nu\bar{\nu}$ is relevant, while, for photon propagation in a neutrino sea, the parity violation in the cross (scattering) channel $\gamma\nu \longrightarrow \gamma\nu$ is important. We first discuss the annihilation process where the two loop contribution turns out to be small. It is natural to expect higher order graphs to be smaller, but, as mentioned, we find a violation of this rule here. This is reminiscent of the surprise in coherent photon scattering from atoms discussed by G.E. Brown and Woodward and later Peierls [4].

The earliest estimate for the annihilation amplitude used the Fermi theory of weak interactions [1], but Gell-Mann [5] noted that, in *V–A* theory, this amplitude vanishes for a point interaction of four fermions. This can be understood physically without any detailed computation. In Fermi Theory, the annihilation amplitude is described by a triangle graph with an electron running in the triangular loop (see Fig. 1).

Two of the vertices of the triangle are electromagnetic, where the two photons couple, and the third vertex is weak, where the two neutrinos emerge. The amplitude has the magnitude $G_F\alpha(pk)$, where p and k are the four momenta of the neutrino and photon, and pk is the only nonvanishing relativistic invariant for the process (the Feynman amplitude is dimensionless which brings the factor pk). Because the two neutrinos emerge from the same space–time point, they can have no relative orbital angular momentum (*s* wave). With vector or axial vector coupling (*V–A*), the spins of the fermion–antifermion pair must be parallel. A theorem of Landau and Yang [6] forbids two free photons in a state with a total angular momentum of one. Consequently, the process is forbidden at order G_F in *V–A* theory. Gell-Mann also noted that this proof does not hold if there is a weak boson mediating the weak interaction;

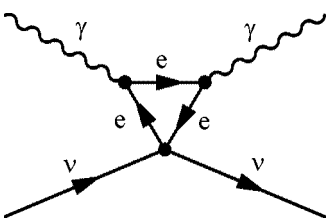

Fig. 1. $\gamma\nu$ scattering in the four-fermion Model.

¶ This article was submitted by the authors in English.

[1] On leave of absence from the Institute of Theoretical and Experimental Physics, Moscow, 117218 Russia.

0021-3640/05/8106-0249$26.00 © 2005 Pleiades Publishing, Inc.

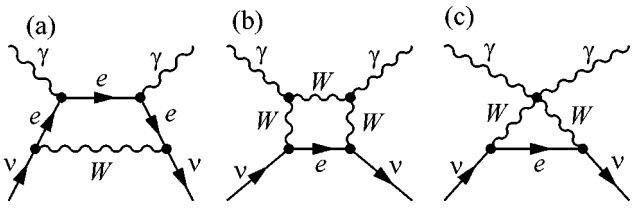

Fig. 2. γν scattering in the Standard Model.

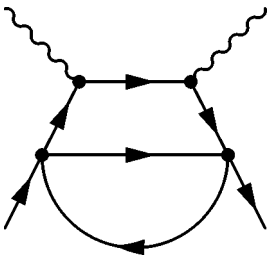

Fig. 3. A sample of two-loop contribution to γν scattering.

thus, the two neutrinos are emitted at separate space–time points.

With a weak boson to mediate the interaction, the (parity conserving) amplitude was estimated by Levine [7], and his estimate remains valid in the standard model, as noted by a number of authors [3, 8]. With the weak boson, the loop changes from a triangle to a square with the weak boson providing one of the sides (see Fig. 2).

This gives an additional factor of pk/M_W^2 to the first order in the momenta p and k. This suppression factor vanishes when the boson mass goes to infinity, in agreement with Gell-Mann's theorem. The precise cross section for the annihilation was computed by Dicus and Repko [8] to the order $(G_F\alpha)^2$:

$$d\sigma/dz = [(G_F\alpha)^2/32\pi^3][\omega^6/M_W^4][1-z^4], \qquad (1)$$

where z is $\cos\theta$ and ω is the photon energy (in the CoM system: $pk = \omega^2(1-z)$) and we have dropped logarithms. This is in agreement with the one loop Feynman amplitude described above up to a constant factor:

$$T^{(1)} = [G_F\alpha\omega^4/M_W^2] \times [\text{angular function}][\text{logarithms}]. \qquad (2)$$

The suppression factor ω^2/M_W^2 may be interpreted as a $(kR)^2$ factor associated with a d-wave for the two neutrinos. Therefore, the leading order amplitude may be thought of as anomalously small compared to the initial expectations [8].

When we go to the next order in weak interactions, there is a set of diagrams in which the two neutrinos are emitted at a separation of the order of the Compton wavelength of the electron instead of the Compton wavelength of the weak boson. The diagram remains a square with two adjacent weak (order G_F) vertices separated by an electron-neutrino loop. The two final neutrinos are emitted at the two weak vertices, and the two photons couple at the two remaining vertices (see Fig. 3).

We can estimate the Feynman amplitude associated with the two-loop graph in the lowest order using the same dimensional arguments as in the case of the one-loop result, changing the M_W with m_e in the denominator:

$$T^{(2)} = [G_F^2\alpha(pk)^3/m_e^2] = [G_F^2\alpha\omega^6/m_e^2][\text{angular function}]. \qquad (3)$$

Therefore, the ratio of the two-loop amplitude to the one loop is:

$$T^{(2)}/T^{(1)} = G_F\omega^2(M_W^2/m_e^2). \qquad (4)$$

The bracketed ratio of the two squared masses is very large $\sim 10^{10}$ so that the cross-section is dominated by the leading term $T^{(1)}$ only at low energies ($\omega < m_e$). However, at intermediate photon energies $\omega > m_e$, our estimate of the two loop contribution is no longer valid since the ratio pk/m_e^2 is no longer small. To estimate what happens at these energies, we take the limit where this ratio is large; then, we expect m_e^2 to be replaced by pk. Then, the ratio of the two loop contribution to the one loop contribution becomes of order $G_F M_W^2$, which is a small number (of order 10^{-2}) independent of energy. Therefore, there is no enhancement of the annihilation amplitude due to the two loop diagrams. This is in accord with expectations.

We come now to the parity violating amplitude in the cross channel. This was first studied by Royer [2] using a triangle graph. His result was criticized by Stodolsky [2] on the basis of Gell-Mann's theorem. More recently, estimates have been proposed using the standard model [3] and the one lepton loop graph for both real and virtual photons. Here, we show that these one loop estimates are all negligible when compared to the two lepton loop estimate for real photons.

In the cross channel, the parity violating amplitude has to be odd under inversion of the coordinates. The precise form is discussed in section 2 and given below. As a result, parity violation appears dimensionally as a two loop effect even for a one loop amplitude. Consequently, it is natural to consider two loop terms together with one loop terms.

The estimate of the parity violating Feynman amplitude in the standard model can be written in the form [3]:

$$T_{pv}^{(1)} = C\frac{G_F\alpha(pk)^2}{\sqrt{2}M_W^2}\epsilon_{\mu\nu\alpha\beta}\epsilon_\mu(k)\epsilon_\nu^*(k)\left(\frac{p_\alpha k_\beta}{M_W^2}\right) \sim 194 G_F\alpha\omega^2\left(\frac{\omega^4}{M_W^4}\right), \quad (5)$$

where C is a constant involving logarithms [3], and, in the second line, we evaluate the magnitude of the first expression in the forward direction for photons of energy ω where $pk = 2\omega^2$. This formula should apply for $\omega < M_W$.

With two lepton loops, the corresponding parity violating Feynman amplitude has the form (for $\omega < m_e$)

$$T_{pv}^{(2)} = \frac{3G_F^2\alpha(pk)^2}{32\pi^3}\epsilon_{\mu\nu\alpha\beta}\epsilon_\mu(k)\epsilon_\nu^*(k)\frac{p_\alpha k_\beta}{m_e^2} \sim 0.025 G_F^2\alpha\omega^6/m_e^2. \quad (6)$$

If we compare the two lepton loop to the one lepton loop result, we find

$$T_{pv}^{(2)}/T_{pv}^{(1)} \sim (10^{-4})G_F M_W^2[M_W^2/m_e^2]. \quad (7)$$

This ratio is quite large and independent of the photon energy below $m_e \sim 500$ keV; its value is approximately 2×10^5. Physically, this reflects the fact that the two final neutrinos are separated in the two loop Feyn–Man graph by an intermediate electron and a neutrino, hence, a distance of an electron Compton wavelength. Even for photon energies above 1 MeV, the corresponding graph with a muon loop enhances the amplitude for photon–muon–neutrino scattering by a factor of 5. Should such an effect be observed, it would indicate a violation of CPT and Lorentz invariance [9]. Attempts to observe such an effect have been unsuccessful [10]. Why is the situation different with the parity violation in the forward amplitude in the scattering channel? The answer is simple. This amplitude must be odd under parity and therefore be at least cubic in kp. Thus, we need an extra factor of kp and this comes (in the one-loop case) with its own denominator M_W^2 for dimensional reasons. Therefore, the parity violating amplitude, even in the one loop diagram, is formally of order G_F^2 and, consequently, on par with the two loop diagram. However, it should be emphasized that, even with this large enhancement factor, the effect remains extremely small.

For real photons $k^2 = 0$, the two loop estimates are as explained above, dominant. Therefore, estimates of the rotatory power of the neutrino sea in the literature [3] have to be multiplied by a factor of 2×10^5 to make them correct. In particular, using Eq. (31) of Abbasabadi and Repko [3] and applying this correction, we get, for the rotatory power ϕ/L, the formula:

$$\phi/L = 0.015 G_F^2\alpha\omega^2 T_\nu^2(N_\nu - N_{\bar\nu})/m_e^2, \quad (8)$$

which should only apply in the range discussed by Abbasabadi and Repko [3] (where T_ν is the neutrino Fermi energy).

For off-mass shell photons the situation is different, since the Landau–Yang theorem does not apply to off-mass shell photons. Therefore, even the lowest triangle graph is viable, as was realized by Nieves *et al.* [3]. At low photon energy, their one loop estimate remains dominant, while, at higher photon energies, the two loop estimate dominates. The transition between Low and High photon energies ω^* is given by the equation $\omega^* E_\nu > 30$ eV^2, where E_ν is the neutrino energy in the rest frame of the sea. For a standard sea of energy of a few degrees Kelvin, the transition occurs in the $\omega \sim$ 100 keV region. However, for an unconventional sea of Fermi Energy 100 eV [11], the two loop estimate will dominate even for visible photons. For radio waves, the one loop estimate dominates for virtual photons.

2. EFFECTIVE LAGRANGIAN

For a systematic study of neutrino–photon interaction, it is useful to work with effective Lagrangians.

The simplest example of the effective Lagrangian is the four-fermion interactions of neutrinos ν with electrons e. For fermions with momenta much smaller than the intermediate bosons mass, one can integrate the degrees of freedom associated with W and Z and write the effective Lagrangian only for fermionic degrees of freedom:

$$L_{\text{eff}} = \frac{G_F}{\sqrt{2}}(\bar\nu\gamma_\alpha\nu)(\bar e\Gamma_\alpha e), \quad (9)$$

where $\Gamma_\alpha = g_V\gamma_\alpha + g_A\gamma_\alpha\gamma_5$. In the Standard Model (SM), one finds $g_V = \frac{3}{2} - 2\sin^2\theta_W$, $g_A = \frac{3}{2}$. For small momenta, this effective Lagrangian is as good as the fundamental Lagrangian of the SM.

Consider now the process $\nu(p) + \gamma(k) \longrightarrow \nu(p) + \gamma(k)$ at momenta smaller than the intermediate bosons mass or even smaller than the mass of an electron m_e. Interaction between neutrinos and photons occurs only through the interaction of photons with charged virtual particles in loops. Loop diagrams are numerous and a bit complicated. For small momenta $pk/m_W^2 \ll 1$, one can expand $\nu(p) + \gamma(k) \longrightarrow \nu(p) + \gamma(k)$ amplitudes in the power series in this small parameter. The lowest terms of this expansion can be represented as a matrix

element of the appropriate operators, i.e., of the particular terms of the effective Lagrangian.

Each term of the effective Lagrangian has to be a Lorenz-invariant combination of the gauge-invariant electromagnetic field tensor $F_{\mu\nu}$ and the left-handed neutrino field $\nu_L = \frac{1}{2}(1+\gamma_5)\nu$ and their derivatives. The effective Lagrangian has dimension four: $[L] \sim [m]^4$. The operators may have higher dimensions D. To preserve the correct dimension, the coefficients in front of these operators should be proportional to the appropriate power of $1/m$, where m is the scale of mass walking inside the loops. The actual calculation of the diagrams gives numerical a coefficient in front of the operator.

This line of reasoning is very similar to the naive dimensional arguments given in the Introduction. The only advantage of the effective Lagrangian is that, within that more advanced approach, we get a more clear understanding of the structure of the operators (i.e., of the scattering amplitudes).

2.1. P-even Scattering Amplitude

2.1.1. One-loop approximation. Consider the effective Lagrangian for P-even $\nu\gamma$ scattering. The photon's part of the amplitude should be even under parity, i.e., be the same for right-handed photons and left-handed photons. One has to construct appropriate Lorenz invariant operators from the fields $F_{\mu\nu}$ and ν_L. The combination of the fields that satisfies all these conditions looks as follows:

$$L_{\text{eff}} \sim \frac{e^4}{m^4}[F_{\mu\alpha}F_{\mu\beta}]\bar{\nu}\gamma_\alpha\partial_\beta(1+\gamma_5)\nu + \text{h.c.} \qquad (10)$$

It has the dimension $D = 8$. The matrix element of L_{eff} for forward scattering gives the amplitude

$$T \sim \frac{e^4}{m^4}(pk)^2\epsilon(k)^*\epsilon(k). \qquad (11)$$

If we identify the parameter m in Eq. (11) with the largest mass in the diagrams (i.e., with m_W), we reproduce the well known result [7] up to the numerical constant.

From this exercise, it is absolutely clear that nonzero $\gamma\nu$ scattering appears only in the second order in the photon momenta, i.e., in the order $(pk)^2$. Thus, one immediately concludes that any results of zero order in k, i.e., of order $(G_F\alpha) \sim \alpha^2/m_W^2$ (e.g., such as in [1, 2]), are erroneous.

There is no way to violate the Gell-Mann theorem within effective Lagrangians. To get the amplitude of the order $G_F\alpha$, one needs an operator with $D = 6$. By direct inspection, one finds that there is no gauge invariant operator with $D = 6$.

2.1.2. Two-loop approximation. Now, consider two-loop amplitudes with light particles (i.e., electrons and neutrinos) in an intermediate state between two external neutrino vertices. We expect that these diagrams are proportional to $G_F^2\alpha/m_e^2$. Thus, to preserve the correct dimension in the effective Lagrangian, we need an operator of dimension $D = 10$. The appropriate effective Lagrangian is

$$L_{\text{eff}} \sim \frac{G_F^2\alpha}{m_e^2}[F_{\mu\alpha}(\partial_\gamma F_{\mu\beta})][\bar{\nu}\gamma_\alpha\partial_\beta\partial_\gamma(1+\gamma_5)\nu] + \text{h.c.} \qquad (12)$$

For this L_{eff}, the scattering amplitude is of the third order in (pk)

$$T \sim C\frac{G_F^2\alpha}{m_e^2}(pk)^3\epsilon(k)\epsilon^*(k). \qquad (13)$$

Thus, for P-even scattering, second order loops give a correction of the order $G_F M_W^2 (pk/m_e^2)$, i.e., a small correction to the one-loop result.

2.2. Optical Activity. P-odd Scattering Amplitude

Now, let us come back to the P-odd effects in $\nu\gamma$ scattering and find the appropriate operators in L_{eff} responsible for optical activity. The Lagrangian of dimension $D = 8$ that depends on P-odd combinations of photon polarizations has the form

$$L_{\text{eff}} \sim \frac{1}{m_W^4}[F_{\mu\alpha}\tilde{F}_{\mu\beta}][\bar{\nu}\gamma_\alpha\partial_\beta(1+\gamma_5)\nu] + \text{h.c.}, \qquad (14)$$

where $\tilde{F}_{\mu\nu} = \frac{1}{2}\epsilon_{\mu\nu\alpha\beta}F_{\alpha\beta}$.

The surprise is that this operator does not work in our case. One can check that the matrix element of $F_{\mu\alpha}\tilde{F}_{\mu\beta}$ between photons with the same momenta and polarization (forward scattering) is identically zero and this operator of $D = 8$ does not contribute into P-odd forward scattering. Thus, the P-odd effects are zero in the $(pk)^2/m_W^4$ order. The first nonzero effect is of the third order $\sim(pk)^3$. The birefringence of the neutrino sea is strongly suppressed!

To find the effect in the next order, we have to look for the operators of higher dimension $D = 10$. One of these operators looks similar to the following:

$$L_{\text{eff}} \sim \frac{1}{m^6}[F_{\mu\alpha}(\partial_\gamma\tilde{F}_{\mu\beta})][\bar{\nu}\gamma_\alpha\partial_\beta\partial_\gamma(1+\gamma_5)\nu] + \text{h.c.} \qquad (15)$$

With this L_{eff}, the forward scattering amplitude for a photon with momentum k and for a neutrino with momentum p is equal to

$$T = C(e^4/8\pi^2)(pk/m^2)^2 \times \epsilon_{\mu\nu\alpha\beta}\epsilon_\mu(k)\epsilon_\nu^*(k)(p_\alpha k_\beta/m_W^2). \quad (16)$$

This amplitude makes a different contribution to the left-handed and right-handed photon scattering: $T_{LL} = -T_{RR}$.

3. ACTUAL CALCULATIONS

3.1. One-Loop Calculations: Real Photons

The actual calculation of the coefficient C has been performed in one loop-approximation in [3] with the results

$$T = C\left(\frac{e^4}{8\pi^2 s^2}\right)\left(\frac{pk}{m_W^2}\right)^2 \epsilon_{\mu\nu\alpha\beta}\epsilon_\mu(k)\epsilon_\nu^*(k)\left(\frac{p_\alpha k_\beta}{m_W^2}\right), \quad (17)$$

where

$$C = 4/3(\ln(m_W^2/m^2) - 11/3), \quad (18)$$

in the third reference in [3] and

$$C = 4/3(\ln(m_W^2/m^2) - 8/3), \quad (19)$$

in the fourth one [3]. The reason for that discrepancy is unknown. Though numerically Eqs. (18) and (19) differ by only a few per cent, it would be interesting to understand whether there is a correct one-loop calculation.

On the other hand, we find, for a P-odd effect, two-loop diagrams many orders of magnitude larger than the one-loop contribution. Thus, we can neglect any one-loop results.

3.2. One-Loop Calculations: Off-shell Photons

The optical activity for off-shell photons was first considered by Mohanty, Nieves, and Pal in [3]. They noticed that the Gell-Mann prohibition theorem does not work for the off-shell photons. Thus, one can expect that the off-shell amplitude is of the first order in $1/m_W^2$. Indeed,

$$T = (e^4/8\pi^2 s^2)\epsilon_{\mu\nu\alpha\beta}\epsilon_\mu(k) \times \epsilon_\nu^*(k)(p_\alpha k_\beta/m_W^2)(k^2/6m_e^2), \quad (20)$$

where $s = \sin\theta_W$.

Equation (20) differs from the original result of [3] by a factor of 1/2. The reason is that the triangle diagram was missing there. (This is the triangle diagram with Z boson and two photons. For real photons $k^2 = 0$, the triangle diagrams cancel each other in the SM, since the SM is anomaly free. However, for off-shell photons, each triangle diagram makes a contribution proportional to k^2/m^2. The sum of all triangles is nonzero, and the main contribution comes from the electron loop. This contribution has to be taken into account.)

3.3. Two-Loop Calculation

The physical reason for the dominance of the two-loop diagrams under the one-loop in P-odd amplitudes is simple. To escape Gell-Mann's restriction, one needs nonlocal interactions in order to include the higher orbital momenta of the pair $\nu\bar{\nu}$ into the annihilation process. In the one loop approximation, the expected value of the orbital momentum of the neutrino pair is $\sim p/m_W$. The factor $1/m_W$ measures the shortest separation of two neutrinos during interaction (nonlocality).

In the two-loop approximation, the expected value of the neutrino pair orbital moment is $\sim p/m_e$. The factor $1/m_e$ is due to $(e^-e^+\nu)$ in the intermediate states.

Kinematically, P-odd amplitudes are of the order of $(pk)^3$ (see Section 2.2). On dimensional grounds, we conclude that two-loop amplitudes are of the same order $(pk)^3$ (see Section 2.1.2). Thus, the one-loop P-odd amplitude has the same dependence on pk as the two-loop P-odd amplitude. Moving to the next order in the electroweak interaction, we loose a small factor of $\alpha/2\pi$ but win a great factor of m_W^2/m_e^2. The net effect is

$$T^{(2)}/T^{(1)} \sim (\alpha/2\pi)(m_W^2/m_e^2) \sim 10^7. \quad (21)$$

The actual calculation is rather lengthy. The result is

$$T^{(2)} = (13/27)(G^2e^2/64\pi^4)(g_V^2 + g_A^2)(pk)^2 \times \epsilon_{\mu\nu\alpha\beta}\epsilon_\mu(k)\epsilon_\nu^*(k)(p_\alpha k_\beta/m_e^2). \quad (22)$$

Thus, the enhancement factor is

$$T^{(2)}/T^{(1)} = (\alpha/64\pi\sin^2\theta_W)(m_W^2/m_e^2) \times (13/27C)(g_V^2 + g_A^2) \sim 10^5, \quad (23)$$

where C is a one-loop coefficient from Eq. (8). We have lost two orders of magnitude compared with the naive estimate in Eq. (10), mainly due to the large logarithmic coefficient C in the one-loop amplitude. Still, the enhancement factor is very large $\sim 10^5$!

This research was supported by the NSERC Canada and by the Russian Foundation for Basic Research (project no. 00-15-96562).

REFERENCES

1. H. Y. Chiu and P. Morrison, Phys. Rev. Lett. **5**, 573 (1960); S. G. Matinyan and N. N. Tsilosuni, Sov. Phys. JETP **14**, 1195 (1961).
2. J. Royer, Phys. Rev. **174**, 1719 (1968); G. Karl, Can. J. Phys. **54**, 568 (1976).

3. S. Mohanty, J. F. Nieves, and P. Pal, Phys. Rev. D **58**, 093007 (1998); Ali Abbasabadi and W. W. Repko, Phys. Rev. D **64**, 113007 (2001); Phys. Rev. D **67**, 073018 (2003); G. Karl and V. A. Novikov, hep-ph/0009012; V. B. Bezerra, H. J. Mosquera Cuesta, and C. N. Ferreira, Phys. Rev. D **67**, 084011 (2003); V. B. Bezerra, C. N. Fereira, and J. A. Helayel-Neto, hep-th/0405181; Yashar Aghababaie and C. P. Burgess, Phys. Rev. D **63**, 113006 (2001).
4. R. E. Peierls, *Surprises in Theoretical Physics* (Princeton Univ. Press, Princeton, N.J., 1975; Nauka, Moscow, 1988).
5. M. Gell-Mann, Phys. Rev. Lett. **6**, 70 (1961).
6. L. D. Landau, Dokl. Akad. Nauk SSSR **60**, 207 (1948); C. N. Yang, Phys. Rev. **77**, 242 (1950).
7. M. J. Levine, Nuovo Cimento A **48**, 67 (1967).
8. D. A. Dicus and W. W. Repko, Phys. Rev. D **48**, 5106 (1993).
9. S. Coleman and S. Glashow, hep-ph/9812418; R. Jackiw and V. A. Kostelecky, Phys. Rev. Lett. **82**, 3572 (1999).
10. J. N. Clarke, G. Karl, and P. J. S. Watson, Can. J. Phys. **60**, 1561 (1982).
11. V. M. Lobashev, V. N. Aseev, A. I. Belesev, *et al.*, Phys. Lett. B **460**, 227 (1999).

JETP Letters, Vol. 81, No. 6, 2005, pp. 255–259. From Pis'ma v Zhurnal Éksperimental'noĭ i Teoreticheskoĭ Fiziki, Vol. 81, No. 6, 2005, pp. 318–322.

Modulation Instability of Stokes Wave → Freak Wave¶

A. I. Dyachenko[1] and V. E. Zakharov[1, 2]

[1] *Landau Institute for Theoretical Physics, Russian Academy of Sciences, Moscow, 117940 Russia*
e-mail: alexd@landau.ac.ru

[2] *Department of Mathematics, University of Arizona, Tucson, AZ 857201, USA*

Received February 24, 2005

Formation of waves of large amplitude (freak waves, killer waves) at the surface of the ocean is studied numerically. We have observed that freak waves have the same ratio of the wave height to the wave length as limiting Stokes waves. When a freak wave reaches this limiting state, it breaks. The physical mechanism of freak wave formation is discussed. © *2005 Pleiades Publishing, Inc.*

PACS numbers: 02.60.Cb, 47.15.Hg, 92.10.–c

1. INTRODUCTION

Waves of extremely large size, which are alternatively called freak, rogue, or giant waves, are a well-documented hazard for mariners (see, for instance [1–4]). These waves are responsible for the loss of many ships and human lives. There are no doubts that freak waves are essentially nonlinear objects. They are very steep. In the last stage of their evolution, their steepness becomes infinite, thus, forming a wall of water. Before this moment, the steepness is higher than for the limiting Stokes wave. Moreover, a typical freak wave is a single event (see [5]). Before breaking, it has a crest three to four (or even more) times higher than the crests of neighboring waves. A freak wave is preceded by a deep trough, or hole in the sea. The characteristic life time of a freak wave is short—ten wave periods or so. If the wave period is fifteen seconds, this is just a few minutes. Freak waves appears almost instantly from a relatively calm sea. Certainly, these peculiar features of freak waves cannot be explained by a linear theory. The focusing of ocean waves creates only the preconditions for formation of freak waves, which are a strongly nonlinear effect.

It is natural to associate the appearance of freak waves with the modulation instability of Stokes waves. This instability is usually named after Benjamin and Feir; however, it was first discovered by Lighthill in [6]. The theory of instability was developed independently in [7] and in [8]. Feir (see [9]) was the first to observe the instability experimentally in 1967.

A slowly modulated weakly nonlinear Stokes wave is described by the nonlinear Shrödinger equation (NLSE), which is derived in [10]. This equation is integrable (see [11]) and is just the first term in the hierarchy of envelope equations describing packets of surface gravity waves. The second term in this hierarchy was calculated by Dysthe in [12], and the next one was found a few years ago in [13]. The Dysthe equation was solved numerically by Ablovitz and his collaborates (see [14]).

Since the first work of [1], many authors have tried to explain freak wave formation in terms of NLSE and its generalizations such as the Dysthe equation. A vast amount scientific literature is devoted to this subject. The list presented below is long but incomplete: [13–23]. A survey of the different possible mechanisms of freak wave formation is given in [24, 25].

One cannot deny some advantages achieved by the use of the envelope equations. The results of many authors agree on one important point: nonlinear development of modulation instability leads to concentration of wave energy in a small spatial region. This is a clue about the possible formation of freak waves. On the other hand, it is clear that the freak wave phenomenon cannot be explained in terms of envelope equations. Indeed, NLSE and its generalizations are derived by expansion in series on powers of the parameter $\lambda \simeq (Lk)^{-1}$, where k is the wave number and L is the length of the modulation. For a real freak wave, $\lambda \sim 1$, and any slow modulation expansion fails. However, the analysis of the NLS-type equations gives some valuable information about the formation of freak waves.

Modulation instability leads to the decomposition of an initially homogeneous Stokes wave into a system of envelope quasi-solitons [26, 27]. This state can be called quasi-solitonic turbulence. In this model, solitons can merge, thus, increasing the spatial intermittency and leading to the establishment of chaotic intense modulations of energy density. So far, this model cannot explain the formation of freak waves with $\lambda \sim 1$.

Freak wave phenomenon could be explained if the envelope solutions of a certain critical amplitude are unstable and can collapse. While, in the framework of

¶ This article was submitted by the authors in English.

1D focusing NLSE solitons are stable, the improved model must have some threshold in amplitude for soliton stability. The instability of a soliton of large amplitude and its further collapse could be a proper theoretical explanation of the origin of freak waves.

This scenario was observed in a numerical experiment using the heuristic one-dimensional Maida–McLaughlin–Tabak (MMT) model (see [28]) of one-dimensional wave turbulence [27]. In the experiments described in the cited paper, the instability of a moderate amplitude monochromatic wave leads first to the creation of a chain of solitons, which merge due to inelastic interaction into one soliton of large amplitude. This soliton sucks energy from neighboring waves and becomes unstable and collapses up to $\lambda \sim 1$, thus, producing a freak wave.

In our experiments, a different scenario is observed. Namely, a freak wave appears inside of a slightly modulated wave train. A freak wave looks like the development of some defect on the periodic grid, which is a Stokes wave train.

The most direct way to prove the validity of the scenario outlined above for freak wave formation is a straight numerical solution of the Euler equation describing the potential oscillations of an ideal fluid with a free surface in a gravitational field. This solution can be found using the method published in several articles [29–31]. This method is applicable in 2 + 1 geometry; it includes conformal mapping of a fluid bounded by the surface to the lower half-plane together with an optimal choice of variables, which guarantees the well-posedness of the equations [32].

In the present article, we perform experiments for wave trains of steepness $\mu \simeq 0.15$. This experiment can be considered as a simulation of a realistic situation. If the typical steepness of a swell is $\mu \simeq 0.06$–0.07, in a caustic area, it could easily be two to three times more. In the experiments, we start with the Stokes wave train perturbed by a long wave with twenty times less amplitude. We observe the development of modulation instability and, finally, the explosive formation of a freak wave that is pretty similar to the waves observed in nature.

2. BASIC EQUATIONS

Suppose that an incompressible fluid covers a two-dimensional domain

$$-\infty < y < \eta(x, t), \tag{1}$$

where $\eta(x, t)$ is the shape of the surface. The flow is potential; hence,

$$V = \nabla\phi, \quad \Delta V = 0, \quad \nabla^2\phi = 0. \tag{2}$$

Let $\psi = \phi|_{y=\eta}$ be the potential at the surface and $H = \mathcal{T} + U$ be the total energy. The terms

$$\mathcal{T} = -\frac{1}{2}\int_{-\infty}^{\infty}\psi\phi_n dx, \quad U = \frac{g}{2}\int_{-\infty}^{\infty}\eta^2(x, t)dx, \tag{3}$$

are, correspondingly, the kinetic and potential parts of the energy, where g is the gravity acceleration and ϕ_n is the normal velocity at the surface. The variables ψ and η are canonically conjugated; in these variables, the Euler equation of the hydrodynamics reads

$$\frac{\partial\eta}{\partial t} = \frac{\delta H}{\delta\psi}, \quad \frac{\partial\psi}{\partial t} = -\frac{\delta H}{\delta\eta}. \tag{4}$$

One can perform a conformal transformation to map the domain that is filled with fluid

$$-\infty < x < \infty, \quad -\infty < y < \eta(x, t), \quad Z = x + iy$$

in the Z plane to the lower half-plane

$$-\infty < u < -\infty, \quad -\infty < v < 0, \quad w = u + iv$$

in the w plane. After the conformal mapping, it is convenient to introduce, along with the conformal mapping $Z(w, t)$, the complex velocity potential $\Phi(w, t)$. Next, in [33], equations (4) were transformed into a simple form, which is convenient both for the numerical simulation and analytical study. Namely, by introducing the new variables

$$R = \frac{1}{Z_w}, \quad V = i\Phi_z = i\frac{\Phi_w}{Z_w} \tag{5}$$

one can transform system (4) into the following one:

$$\begin{aligned} R_t &= i(UR_w - RU_w), \\ V_t &= i(UV_w - RB_w) + g(R - 1). \end{aligned} \tag{6}$$

Now, the complex transport velocity U and B

$$U = \hat{P}(V\bar{R} + \bar{V}R), \quad B = \hat{P}(V\bar{V}). \tag{7}$$

In (7), $\hat{P}$ is the projector operator generating a function that is analytical in a lower half-plane. Here, we have omitted all the details, which can be found in [29, 33].

3. NUMERICAL APPROACH

Many numerical schemes have been developed for the solution of Euler equations describing the potential flow of a free-surface fluid in a gravity field. Most of them use integral equations that solve the boundary-value problem for a Laplace equation [34–36]. A survey of the method can be found in [37].

In this article, we study the modulation instability of Stokes waves. As the initial condition, we use a slightly modulated stationary nonlinear wave train. This train is unstable with respect to growing long-scale modulation. This remarkable fact was first established in [6], where the authors calculated the growth-rate of insta-

bility in the limit of long-wave perturbation. As far as Lighthill's growth-rate coefficient was proportional to the wave number of the perturbation length, the result was in principle incomplete: somewhere at short scales, the instability must be arrested. The complete form of the growth-rate coefficient was found independently in [7, 8, 10].

We apply the spectral code to solve equations (6). We should mention that conformal mapping is a routine approach for studying a stationary Stokes wave. The equations for the Fourier coefficients were solved numerically by many authors (see, for instance [38]). The idea to implement conformal mapping for simulation of essentially nonstationary wave dynamics emerged in the beginning of the eighties (see [39]). Since equations (6) were not derived at that time, the authors used the quasi-Lagrangian approach to fluid dynamics. After some experiments and discussion of their results, the idea to use the conformal mapping was abandoned for the following reason: conformal mapping is not good for resolution of wedge-type singularities naturally appearing on the free surface of a fluid. This reason is important if the spatial mesh is sparse. However, modern computers make it possible to use very fine meshes consisting of more than a million points or spectral modes. Thus, this argument is not pertinent any more.

Our recent experiments are sufficiently accurate: we use 10^5 to 2×10^6 harmonics. We solve equations (6) in the periodic domain $0 < x < 2\pi$, putting $g = 1$. The initial data are chosen as a combination of the exact Stokes wave (wave number $k = 10$; steepness $ka = \mu = 0.15$) and a long monochromatic wave with the wave number $k = 1$ and a moderate amplitude 5×10^{-2}. This relatively high level of perturbation is deliberately chosen to make the period of exponential instability growth that is not interesting for us shorter. At given conditions, the maximum growth-rate is

$$\gamma_{\max} \simeq \frac{\sqrt{10}}{2} \times 0.15^2 \simeq 0.035$$

and $\gamma_{\max}^{-1} \simeq 28.6$. The period of the initial wave is $T_0 = 2\pi/\sqrt{10}$. The simulation is continued until $T \simeq 458.842$, that is, until more than sixteen inverse growth-rates have been completed. We performed the computations with double precision with the number of modes doubled as far as the amplitude of the last mode reached 10^{-15}. The maximum number of modes was two millions.

We observed a short period of exponential growth of perturbation, then, some intermediate regime of intensive modulation, which ends up with explosive formation of one single freak wave. Pictures of the surface shape before breaking at the times $T = 442$ and $T = 458.56$ are presented in Fig. 1 and Fig. 2.

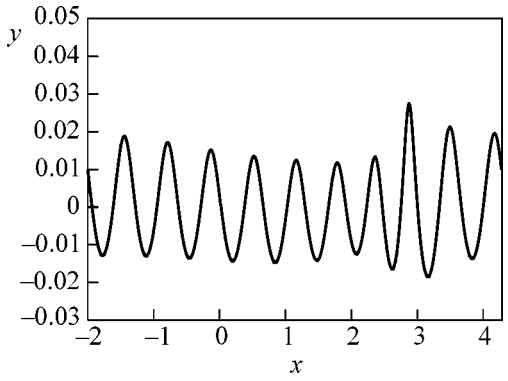

Fig. 1. The shape of the surface at $T = 422$.

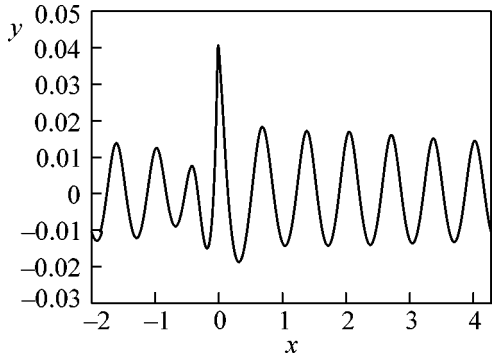

Fig. 2. The shape of the surface at $T = 458.56$.

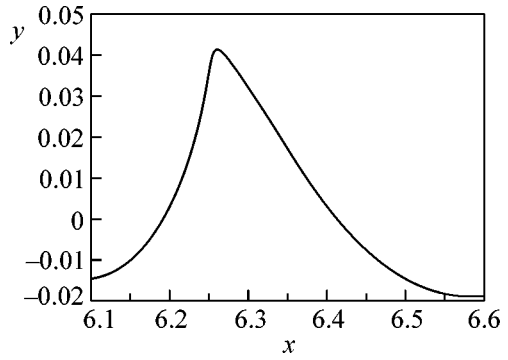

Fig. 3. The shape of the surface near the wave crest at $T = 458.61$.

The time interval from $T = 442$ to $T = 458.56$ contains seven periods of the initial wave only. One can see fast, nonmonotonic formation of the freak wave. At this moment, the freak wave is more steep than the Stokes wave of limiting amplitude. The amplitudes of the waves preceding the freak wave are relatively small (three times less). One can see a trough just ahead of the freak wave. This is the so-called hole in the water (marine folklore) that precedes a freak wave. Figure 3

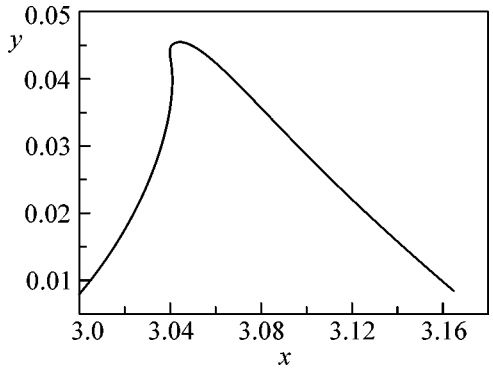

Fig. 4. The shape of the surface near the wave crest at T = 458.842.

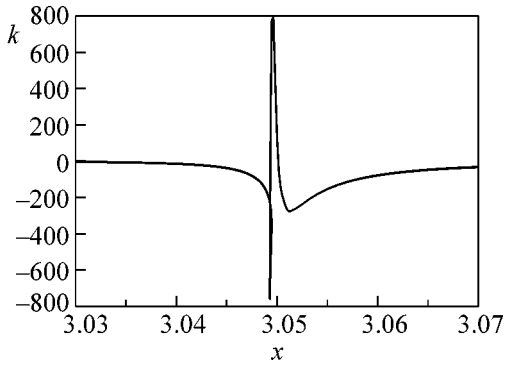

Fig. 5. Curvature (k) of the surface at T = 458.842.

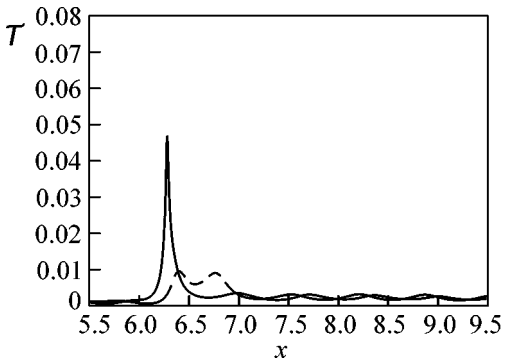

Fig. 6. The density of the kinetic energy just before breaking at T = 456 (dashed line) and at the moment of breaking at T = 458.5 (solid line).

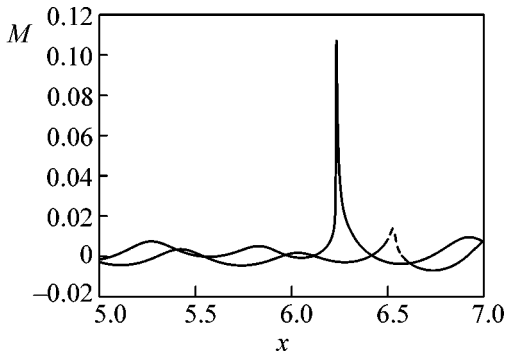

Fig. 7. Distribution of momentum (M) before (dashed line) and after (solid line) breaking.

demonstrates the fine structure of the surface shape near the wave crest.

We managed to continue our simulation until the moment T = 458.842. The zoomed shape of the surface at that time is presented in Fig. 4.

One can see that, near the crest, the front face of the wave is very steep. This is really a wall of water. In some regions, the steepness is even negative. The curvature of the shape is plotted in Fig. 5.

This is actually a breaking wave. Moreover, in all our experiments, at the moment of breaking, we observed that the ratio of the wave height to the wavelength is practically the same and close to that of the limiting Stokes wave, 0.141.

Note that the maximum value of the freak wave height is three times higher than the height of the initial wave. The growing of the wave height up to this level from the level of insignificant wave height takes less than ten wave periods. This is a really fast process; it is three times faster than the development of modulation instability.

Figure 6 displays the evolution of the spatial density of the kinetic energy (in the domain [5.5–9.5]) where the breaking takes place.

One can see that this evolution is nonmonotonous. The density oscillates in time and finally condensates in one very narrow wave crest. In general, the whole process of freak wave formation is nonmonotonous. We can say that the freak wave runs over wave crests until it reaches an extremely high amplitude. This behavior can be easily explained by the difference of the phase and group velocities: the energy propagates with a group velocity that is twice less than the phase velocity. Figure 7 demonstrates the distribution of the horizontal momentum before and after breaking at T = 455 and T = 456. One can see that the process of momentum concentration in a moving but localized area is monotonous. Definitely, this behavior can be explained by the fact that momentum is a conserved quantity.

4. CONCLUSIONS

Let us summarize our numerical experiments. Certainly, they reproduce the most apparent features of freak waves: single wave crests of very high amplitude,

exceeding of the significant wave height by more than three times, appearing from nowhere and reaching full height in a very short time, less than ten periods of surrounding waves. A singular freak wave is proceeded by an area of diminished wave amplitudes. The final fate of a freak wave is breaking. The ratio of the freak wave height to its wavelength is practically the same, being close to the limiting Stokes wave, 0.141. A freak wave moves with the group velocity.

In our experiments, the freak wave appears as a result of the development of modulation instability (if the threshold of the instability is not exceeded, no freak waves appear at all). Then, it takes a long time for the onset of instability to create a freak wave. Meanwhile, a freak wave appears only after the fifteenth inverse growth rate of instability. What happens after the development of instability but before the formation of a freak wave? This stage could be considered as the development of some defect on the periodic grid. This grid is just the initial Stokes wave train. A similar picture was observed in [40], where the breaking of a wave in the group was studied.

We thank E.A. Kuznetsov for helpful discussions. This work was supported by the Russian Foundation for Basic Research (project no. 03-01-00289), the Program "Mathematical Problems in Nonlinear Dynamics" of the RAS Presidium, by the grant for Leading Scientific Schools of Russia, by the United States Army (grant DACA, no. 42-00-C-0044), and by the NSF (under DMS grant no. 0072803).

REFERENCES

1. R. Smith, J. Fluid Mech. **77**, 417 (1976).
2. R. G. Dean, in *Water Wave Kinetics*, Ed. by A. Torum and O. T. Gudmestad (Kluwer Academic, Dordrecht, 1990), p. 609.
3. I. V. Lavrenov, Nat. Hazards **17**, 117 (1998).
4. G. A. Chase, http://bell.mma.edu/achase/NS-221-BigWave.html (2003).
5. V. D. Divinsky, B. V. Levin, L. I. Lopatikhin, *et al.*, Dokl. Earth Sci. **395**, 438 (2004).
6. M. J. Lighthill, J. Inst. Math. Appl. **1**, 269 (1965).
7. T. B. Benjamin and J. E. Feir, J. Fluid Mech. **27**, 417 (1967).
8. V. E. Zakharov, Zh. Éksp. Teor. Fiz. **51**, 668 (1966) [Sov. Phys. JETP **24**, 455 (1967)].
9. J. E. Feir, Proc. R. Soc. London, Ser. A **299**, 54 (1967).
10. V. E. Zakharov, J. Appl. Mech. Tech. Phys. **9**, 190 (1968).
11. V. E. Zakharov and A. B. Shabat, Sov. Phys. JETP **34**, 62 (1972).
12. K. B. Dysthe, Proc. R. Soc. London, Ser. A **369**, 105 (1979).
13. K. Trulsen and K. B. Dysthe, Wave Motion **24**, 281 (1996).
14. M. I. Ablovitz, D. Hammack, J. Henderson, and C. M. Scholder, Phys. Rev. Lett. **84**, 887 (2000); Physica D (Amsterdam) **152–153**, 416 (2001).
15. M. Onorato, A. R. Osborne, M. Serio, and T. Damiani, in *Rogue Waves 2000: Proceedings of a Workshop, Brest, France, 2000*, Ed. by M. Olagnon and G. A. Athanassoulis (Ifremer, Plouzanu, France, 2001), p. 181.
16. M. Onorato, A. R. Osborne, and M. Serio, Phys. Lett. A **275**, 386 (2000).
17. M. Onorato, A. R. Osborne, M. Serio, and S. Bertone, Phys. Rev. Lett. **86**, 5831 (2001).
18. M. Onorato, A. R. Osborne, and M. Serio, Phys. Fluids **14**, L25 (2002).
19. D. H. Peregrine, J. Aust. Math. Soc. B, Appl. Math. **25**, 16 (1983).
20. D. H. Peregrine, D. Skyner, M. Stiassnie, and J. W. Dold, in *Proceedings of 21st International Conference on Coastal Engineering* (1988), Vol. 1, Chap. 54, p. 732.
21. K. Trulsen and K. B. Dysthe, in *Proceedings of 21st Symposium on Naval Hydrodynamics* (1997), p. 550; http://www.nap.edu/books/0309058791/html/550.html.
22. K. Trulsen, in *Rogue Waves 2000: Proceedings of a Workshop, Brest, France, 2000*, Ed. by M. Olagnon and G. A. Athanassoulis (Ifremer, Plouzanu, France, 2001), p. 265.
23. K. Trulsen, I. Kliakhandler, K. B. Dysthe, and M. G. Velarde, Phys. Fluids **24**, 32 (2000); D. Clamond and J. Grue, C. R. Acad. Sci., Ser. Mec. **330**, 575 (2002).
24. C. Kharif and E. Pelinovsky, Eur. J. Mech. B/Fluids **22**, 603 (2003).
25. A. A. Kurkin and E. N. Pelinovsky, *Freak Waves: Facts, Theory and Modeling* (Nizhni Novgorod Univ., 2004).
26. V. E. Zakharov and E. A. Kuznetsov, JETP **86**, 1035 (1998).
27. V. E. Zakharov, F. Dias, and A. N. Pushkarev, Phys. Rep. **398**, 1 (2004).
28. A. Majda, D. McLaughlin, and E. Tabak, J. Nonlinear Sci. **7**, 9 (1997).
29. A. I. Dyachenko, E. A. Kuznetsov, M. D. Spector, and V. E. Zakharov, Phys. Lett. A **221**, 73 (1996).
30. V. E. Zakharov, A. I. Dyachenko, and O. A. Vasilyev, Eur. J. Mech. B/Fluids **21**, 283 (2002).
31. V. E. Zakharov, Am. Math. Soc. Trans., Ser. 2 **182**, 167 (1998).
32. A. I. Dyachenko, in *Proceedings of the II International Conference on Frontiers of Nonlinear Physics* (Nizhny Novgorod–St. Petersburg, Russia, 2004).
33. A. I. Dyachenko, Dokl. Math. **63**, 115 (2001).
34. J. W. Dold and D. H. Peregrine, in *Proceedings of 20th International Conference on Coastal Engineering* (1986), Vol. 1, Chap. 13, p. 163.
35. D. G. Dommermuth and D. K. P. Yue, J. Fluid Mech. **184**, 267 (1987).
36. J. W. Dold, J. Comput. Phys. **103**, 90 (1992).
37. W. Tsai and D. Yue, Annu. Rev. Fluid Mech. **28**, 249 (1996).
38. J. A. Zufiria and P. G. Saffman, Stud. Appl. Math. **74**, 259 (1986).
39. D. Meison, S. Orzag, and M. Izraely, J. Comput. Phys. **40**, 345 (1981).
40. J. Song and M. L. Banner, J. Phys. Oceanogr. **32**, 2541 (2002).

JETP Letters, Vol. 81, No. 6, 2005, pp. 260–263. Translation from Pis'ma v Zhurnal Éksperimental'noĭ i Teoreticheskoĭ Fiziki, Vol. 81, No. 6, 2005, pp. 323–326.

Superhard Superconducting Materials Based on Diamond and Cubic Boron Nitride

G. A. Dubitskiy[1], V. D. Blank[1], S. G. Buga[1], E. E. Semenova[1], V. A. Kul'bachinskiĭ[2]*, A. V. Krechetov[2], and V. G. Kytin[2]

[1] *Technology Institute of Superhard and New Carbon Materials, Ministry of Education and Science of the Russian Federation, Troitsk, Moscow region, 142190 Russia*

[2] *Moscow State University, Vorob'evy gory, Moscow, 119992 Russia*

** e-mail: kulb@mig.phys.msu.ru*

Received February 11, 2005

Superhard superconducting samples with a critical temperature of T_c = 12.6 K are obtained when synthetic diamond powders that were preliminarily coated with a niobium film are sintered at a pressure of 7.7 GPa and a temperature of 1973 K. Superhard superconductors with T_c = 9.3 K are obtained when diamond and molybdenum powders are sintered at a pressure of 7.7 GPa and a temperature of 2173 K. Superconducting samples with T_c = 36.1–37.5 K have been obtained in the systems diamond–MgB_2 and cubic boron nitride–MgB_2. © *2005 Pleiades Publishing, Inc.*

PACS numbers: 62.20.–x, 74.25.–q

INTRODUCTION

Superhard materials with superconducting properties are of considerable interest for the creation of high-pressure devices for investigating the electric and superconducting properties of various materials under pressure. Moreover, engineering applications are possible in the form of high-strength superconducting contacts and cryogenic electrical machines. The development of high-pressure cryogenic equipment requires the production of superhard superconducting materials. One of the possibilities of solving this problem is the sintering of small-crystalline diamond powders with metal powders (Nb, Mo) at high static pressure and temperature. Interacting with diamond, these metals form carbides that bond diamond crystallites into a united compact material and that have relatively high critical temperatures of the transition to the superconducting state.

Superconducting composites consisting of hard superconductors and normal metals that are in thermal and electrical contacts with each other make it possible to satisfy very conflicting requirements imposed on superconducting materials for the production of large superconducting magnetic systems [1].

The production of materials combining such properties as superconductivity, superhardness, and high strength is of both scientific and applied interest. One of the applications is the creation of a superhard material for the production of anvils of high-pressure devices.

Reports on superconducting diamonds appeared recently [2–4]. Prins reported [2] on the observation of a phenomenon that was treated as a new type of superconductivity in experiments with *n*-type diamonds at room temperature. Additional experimental data, as well as the theoretical explanation of the observed phenomenon, are evidently necessary. Ekimov *et al.* [3] presented experimental and calculation data on the superconductivity of polycrystalline diamond aggregates highly doped with boron. The transition to the superconducting state started at $T_c \approx 4$ K, and zero electric resistance was reached at $T \approx 2.3$ K. It was concluded that superconductivity was of the bulk type, and it was attributed to the doped diamond particles. Superconductivity was also found in diamond films strongly doped with boron [4]. The transition to the superconducting state starts at T_c = 7.4 K and ends at 4.2 K.

In this work, superhard superconducting materials have been synthesized on the basis of the systems diamond–Nb, diamond–Mo, diamond–MgB_2, and cubic boron nitride–MgB_2, and the microhardness and superconducting properties of these materials have been investigated.

PROCEDURE FOR PREPARING SAMPLES

The samples of the materials were obtained at high static pressures and temperatures. The experiments were carried out using high-pressure chambers of the type "anvils with cavities" [5]. Pressure was calibrated by resistance jumps in the reference metals Ba (5.5 GPa) and Bi (2.5, 2.7, 7.7 GPa) at phase transitions. The temperature graduation of the chambers was performed using Pt/Pt–10% Rh and W/Re thermocouples.

The initial components were placed into a tantalum-foil shell 0.1 mm thick. Samples were heated by ac current flowing through a graphite heater, tantalum shell, and sample. The experiments were carried out at a pressure of 7.7 GPa and temperatures of (diamond–MgB_2, cubic boron nitride) 1373, (diamond–niobium) 1973, and (diamond–molybdenum) 2173 K for 60–90 s. The samples were quenched under high pressure at a rate of 200° per second. After the pressure decreased to atmospheric pressure, the samples were extracted from the high-pressure cell. They were 4.5 and 3.5 mm in diameter and height, respectively. After grinding and polishing, $3.9 \times 2.51 \times 1.54$-mm parallelepiped samples were obtained.

The phase content of the samples was determined by the x-ray method using an HZG-4A diffractometer and monochromatic 0.1541-nm CuK_α radiation. The resistance of the resulting samples was measured using the standard four-contact method. The electrical contacts were produced using conducting silver paste. The temperature dependence of the resistance was measured in the interval $4.2 < T < 300$ K. The magnetic field was created by a superconducting solenoid.

RESULTS AND DISCUSSION

1. Diamond–Niobium System

Synthetic diamond with 80–100-μm crystallites on whose surfaces a niobium film was deposited by sputtering in vacuum was used as the initial material. The total amount of niobium in the initial material was 24 wt %. The experiments were carried out at a pressure of 7.7 GPa and a temperature of 1973 K for 60 s.

The diffraction patterns primarily exhibit peaks associated with diamond and NbC monocarbide. Peaks of lower intensities belong to Nb_2C. It was found that NbC monocarbide that was synthesized at the boundaries of crystallites had an fcc lattice with the lattice parameter $a_0 = 0.447$ nm. This value is consistent with data obtained for NbC by another method [6]. Carbide Nb_2C has a hexagonal structure with the lattice parameters $a_0 = 0.312$ nm and $c_0 = 0.492$ nm.

Vickers microhardness was measured using a PMT-3 device at an indenter load of 5.5 N. The hardness values are in the range 35–95 GPa. According to [6], the Vickers hardness of NbC is approximately equal to 17 GPa, which is much less than the results obtained in our work for microdomains enriched in NbC. The hardness of such microdomains is high apparently due to the effect of the boundaries of diamond crystallites, which have a much higher hardness (100–150 GPa along different faces and depend on the quality of the crystals).

The temperature of the transition to the superconducting state in all the measurements is fixed at the onset of the transition. According to an analysis of the temperature dependence of the resistance, the critical temperature of the transition of the synthesized samples to the superconducting state is equal to $T_c \approx 12.6$ K (Fig. 1a), which is characteristic of an NbC compound with high stoichiometry [7–9]. Nonstoichiometric NbC compounds have lower T_c or superconductivity is absent in them altogether. The characteristic feature of the synthesized samples is a quite narrow superconducting transition, $\Delta T \approx 1.5$ K. The measured dependence of the resistance of a sample on the external magnetic field (Fig. 1b) is characteristic of a compound whose stoichiometry is very close to that of NbC. The second critical field $H_{c2} = 1.25$ T (at $T = 4.2$ K) corresponds to H_{c2} for NbC films obtained by the laser-evaporation method [8]. Thus, one can assume that, on the surface of diamond crystallites undergoing sintering, NbC is formed with an almost perfect crystal lattice and a low concentration of defects, whose presence also reduces the temperature of the superconducting transition that can even disappear [10].

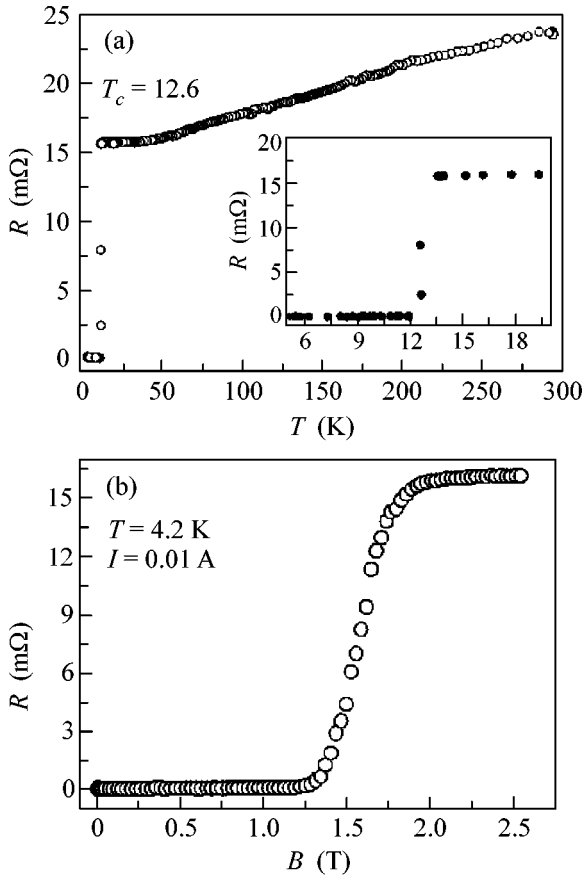

Fig. 1. (a) Temperature and (b) magnetic-field dependences of the resistance for the sample obtained in the diamond–niobium system.

2. Diamond–Molybdenum System

In this system, a synthetic-diamond powder with a granularity of 40–100 μm and a molybdenum powder

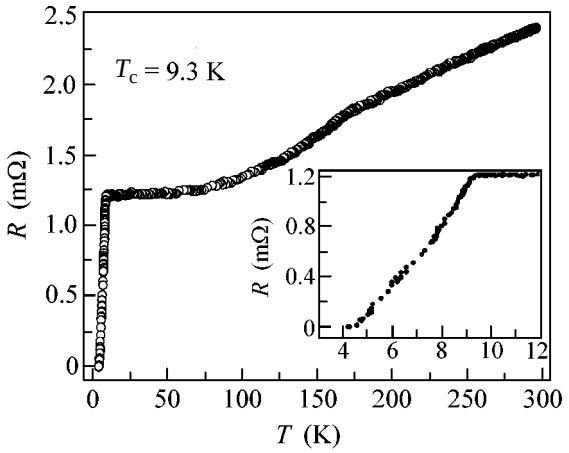

Fig. 2. Temperature dependence of the resistance for the sample obtained in the diamond–molybdenum system.

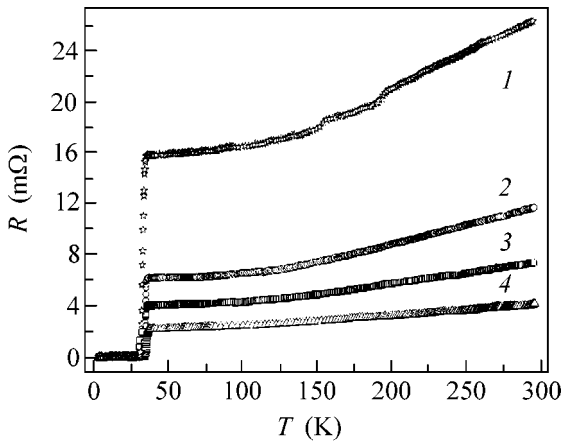

Fig. 3. Temperature dependence of the resistance for the composite samples obtained in the systems (*1*) cubic boron nitride–MgB_2, T_c = 36.1 K; (*2*) diamond–MgB_2, T_c = 36.9 K; (*3*) MgB_2, T_c = 37 K; and (*4*) diamond–niobium–MgB_2, T_c = 37.5 K.

with a particle size of 1–5 μm are used as the initial material consisting of 60 wt % diamond and 40 wt % molybdenum. A compact material was obtained by holding at a pressure of 7.7 GPa and a temperature of 2173 K for 90 s. The phase content of the samples was determined by the same method as used for the diamond–Nb system.

The following phases were identified in the samples: the α-MoC diamond phase with a cubic lattice with the parameter a_0 = 0.427 nm (B1 type), the η-MoC hexagonal phase with the crystal-lattice parameters a_0 = 0.300 nm and c_0 = 1.452 nm, and traces of the γ-MoC hexagonal phase (WC type) with the parameters a_0 = 0.290 nm and c_0 = 0.282 nm. The crystal-lattice parameters that were determined for the molybdenum–carbon compounds are consistent with published data [6]. The Vickers microhardness of the samples lies in the range 27–83 GPa.

The composites that were obtained due to the interaction of diamonds with molybdenum are superconductors with characteristic features. First, the temperature of the transition to the superconducting state is equal to T_c = 9.3 K, which is slightly lower than the T_c values for molybdenum carbide obtained by sintering powders of molybdenum and graphite [11]. Second, the transition width $\Delta T \approx 5$ K is larger than that for the diamond–niobium system. Figure 2 shows the temperature dependence of the resistance of these composites.

3. The Systems Diamond–MgB_2 and Cubic Boron Nitride–MgB_2

Magnesium diboride, whose bulk superconductivity was discovered recently [12, 13], has higher critical temperature T_c = 39 K than niobium carbide and molybdenum carbide.

Many works were devoted to the study of the effect of the conditions under which MgB_2 was obtained and treated at high pressures and temperatures on the superconducting properties of MgB_2 with various dopants [14–20]. It is of interest to obtain a superconducting composite material in which diamond or cubic boron nitride is used as the superhard component and MgB_2 is used as the superconducting component. As the initial material, we used MgB_2 industrial powders in which the content of the basic product was equal to 98.5%. The particle size was reduced to 5–10 μm by additional powdering. The prepared mixtures consisted of 80 wt % of the superhard component and 20 wt % of MgB_2. The granularity of the diamond and cubic boron nitride powders was equal to 40–100 and 28–40 μm, respectively. The assembly of the high-pressure cells and experimental procedure were the same as those used for the diamond–molybdenum system. In one of the experiments, a niobium-coated diamond powder was used. The samples were obtained by holding at a pressure of 7.7 GPa and a temperature of 1373 K for 60 s.

The Vickers microhardness of the diamond–MgB_2 and cubic boron nitride–MgB_2 samples varies in the range 25–78 and 24–57 GPa, respectively. According to [15], the microhardness of MgB_2 samples that were synthesized at 2 GPa and 1073 K from elements with the addition of 2 wt % of a tantalum powder was equal to 12.79 GPa.

The temperature dependence that was measured for the resistance of the samples shows that the temperature of the transition to the superconducting state is equal to $T_c \approx 37$ K, which is close to the value known for MgB_2 [12]. This closeness indicates that MgB_2 plays a key role in the superconductivity of these composite materials, and the matrix consisting of cubic boron nitride or diamond insignificantly changes the T_c.

The mechanical properties of such a superconducting material are much higher than those of compacted MgB_2. Figure 3 shows the results.

CONCLUSIONS

A composite superhard superconducting material in the form of the diamond matrix and superconducting NbC channels that have the perfect crystal structure and $T_c = 12.6$ K has been obtained in the diamond–niobium system at high pressures and temperatures.

A composite material consisting of a diamond matrix and superconducting channels primarily of MoC with $T_c = 9.3$ K has been obtained in the diamond–molybdenum system. Parts of various devices can be made of such composites.

Composite materials consisting of the superhard matrices (80 wt %) and superconducting channels of MgB_2 with $T_c = 36.1$–37.5 K have been obtained in the systems diamond–MgB_2 and cubic boron nitride–MgB_2.

The microhardness of samples obtained in the systems under investigation indicates that the composite matrix (consisting of cubic boron nitride or diamond) occupying the major part of the volume of the samples has a microhardness of 57–95 GPa. Such microhardness values are characteristic of superhard compact polycrystalline materials based on cubic boron nitride and diamond that are used to produce various abrasive and cutting tools [21]. Thus, the method used in this work allows the production of high-strength superhard superconducting materials.

This work was supported by the Russian Foundation for Basic Research (project no. 05-02-17368a).

REFERENCES

1. A. V. Gurevich, R. G. Mints, and A. L. Rakhmanov, *Physics of Composite Superconductors* (Nauka, Moscow, 1987) [in Russian].
2. J. F. Prins, Semicond. Sci. Technol. **18**, 131 (2003).
3. E. A. Ekimov, V. A. Sidorov, E. D. Bauer, *et al.*, Nature **428**, 542 (2004).
4. Y. Takano, M. Nagao, K. Kobayashi, *et al.*, in *Abstract Book of 15th European Conference on Diamond, Diamond-like Materials, Carbon Nanotubes, Nitrides and Silicon Carbide (Diamond 2004)* (Riva del Garda, Italy, 2004), No. 4.4.
5. V. N. Narozhnyĭ, G. N. Stepanov, G. A. Dubitskiy, *et al.*, Fiz. Tekh. Vys. Davlenii **27**, 88 (1988).
6. L. Toth, *Transition Metal Carbides and Nitrides* (Academic, New York, 1971; Mir, Moscow, 1974).
7. Yu. S. Karimov and T. G. Utkina, Pis'ma Zh. Éksp. Teor. Fiz. **51**, 468 (1990) [JETP Lett. **51**, 528 (1990)].
8. N. P. Shabanova, S. I. Krasnosvobodtsev, V. S. Nozdrin, and A. I. Golovashkin, Fiz. Tverd. Tela (St. Petersburg) **38**, 1969 (1996) [Phys. Solid State **38**, 1085 (1996)].
9. S. I. Krasnosvobodtsev, N. P. Shabanova, E. V. Ekimov, *et al.*, Zh. Éksp. Teor. Fiz. **108**, 970 (1995) [JETP **81**, 534 (1995)].
10. W. E. Pickett, B. M. Klein, and R. Zeller, Phys. Rev. B **34**, 2517 (1986).
11. R. H. Willens, E. Buehler, and B. T. Matthias, Phys. Rev. **159**, 327 (1967).
12. J. Nagamatsu, N. Nakagawa, T. Muranaka, *et al.*, Nature **410**, 63 (2001).
13. Y. Zenitani and J. Akimitsu, AAPPS Bull. **13**, 26 (2003).
14. C. U. Jung, Min-Seok Park, W. N. Kang, *et al.*, Appl. Phys. Lett. **78**, 26 (2001).
15. T. A. Prikhna, W. Gawalek, A. B. Surzhenko, *et al.*, Physica C (Amsterdam) **1543**, 372 (2002).
16. W. Pachla, P. Kovac, R. Diduszko, *et al.*, Supercond. Sci. Technol. **16**, 7 (2003).
17. A. Tampieri, G. Celotti, S. Sprio, *et al.*, Physica C (Amsterdam) **97**, 400 (2004).
18. P. Toulemonde, N. Musolino, and R. Flukiger, Supercond. Sci. Technol. **16**, 231 (2003).
19. Y. Zhao, C. H. Cheng, X. F. Rui, *et al.*, Appl. Phys. Lett. **83**, 2916 (2003).
20. S. X. Dou, W. K. Yeoh, J. Horvat, and M. Ionescu, Appl. Phys. Lett. **83**, 4996 (2003).
21. A. A. Shul'zhenko, B. I. Ginzburg, N. I. Khovakh, *et al.*, Sverkhtverd. Mater., No. 1, 23 (1987).

Translated by R. Tyapaev

JETP Letters, Vol. 81, No. 6, 2005, pp. 264–266. Translated from Pis'ma v Zhurnal Éksperimental'noĭ i Teoreticheskoĭ Fiziki, Vol. 81, No. 6, 2005, pp. 327–329.

Magnetic Properties of Copper as a Constituent of Nanobridges Formed between Spatially Fixed Deoxyribonucleic Acid Molecules

V. N. Nikiforov[1]*, V. D. Kuznetsov[2], Yu. D. Nechipurenko[1, 3], V. I. Salyanov[3], and Yu. M. Yevdokimov[3]

[1] *Moscow State University, Vorob'evy gory, Moscow, 119899 Russia*
** e-mail: nvn@lt.phys.msu.su*
[2] *Mendeleev University of Chemical Technology, Miusskaya pl. 9, Moscow, 125047 Russia*
[3] *Engelhardt Institute of Molecular Biology, Russian Academy of Sciences, ul. Vavilova 32, Moscow, 119991 Russia*
Received February 11, 2005

The number of copper ions as constituents of a nanobridge that links two deoxyribonucleic acid (DNA) molecules that are fixed in a particle of a liquid-crystalline dispersion has been evaluated from the measurements of the magnetic susceptibility of particles in the liquid-crystalline dispersion of DNA. It has been shown that the experimental data are consistent with both theoretical assumptions on the possible structure of a nanobridge and a thermodynamic model that describes the formation of these bridges. © *2005 Pleiades Publishing, Inc.*

PACS numbers: 75.75.+a

INTRODUCTION

One of the strategies for producing nanoconstructions containing double-stranded nucleic acid molecules is based on the use of liquid-crystalline dispersions rather than single nucleic acid molecules. The liquid-crystalline dispersions of nucleic acids result from the phase exclusion of these molecules from aqueous polymer solutions. In this case, the problem is reduced to the formation of nanobridges between neighboring nucleic acid molecules fixed at a distance of 25–40 Å in the structure of liquid-crystalline dispersion particles. According to the model proposed previously [1–3], nanobridges such as [–Cu^{2+}–daunomycin–Cu^{2+}–…–Cu^{2+}–daunomycin–Cu^{2+}–] can link the nearest neighboring molecules of nucleic acids. Thus, the nanobridges crosslink neighboring nucleic acid molecules to form a rigid nanoconstruction (Fig. 1).

The aim of this work was to determine the number of Cu^{2+} ions incorporated into nanobridges. To this end, we found the contribution of paramagnetic Cu^{2+} centers to the total magnetic susceptibility of liquid-crystalline dispersions. It is well known that, when chelate bridges with four reactive oxygen atoms are formed, copper ions occur in the d^9 state [4], which exhibits a nonzero magnetic moment.

EXPERIMENTAL PROCEDURE

Double-stranded deoxyribonucleic acid (DNA) from calf thymus (Sigma) with a molecular weight of $(7–8) \times 10^5$ amu was used for the sample preparation. Commercial daunomycin, $CuCl_2$, NaCl, and sodium phosphates from Sigma were used without additional purification. A nanoconstruction that was based on double-stranded DNA was formed in accordance with the three-stage procedure described in [5]. The nanoconstruction was centrifuged (5000 rpm, 40 min, 15°C), and the resulting sediment was washed with distilled water to remove the excess of $CuCl_2$, placed in a test tube, and used for the subsequent analysis. Magnetic and EPR-spectroscopic studies were performed with the resulting washed and dried liquid-crystalline dispersions.

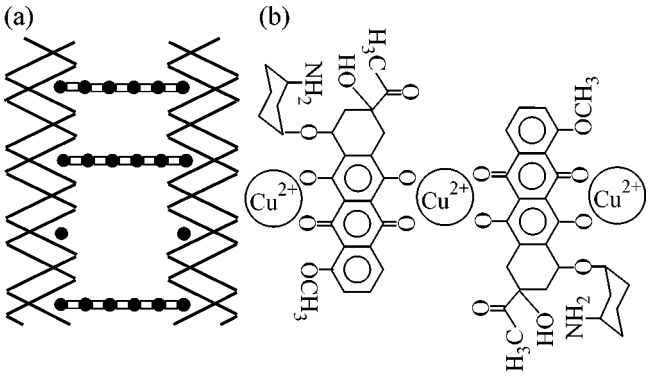

Fig. 1. Schematic diagram of the formation of bridges between two DNA molecules. (a) Bridges between two DNA molecules fixed in the structure of the liquid-crystalline dispersion (filled circles indicate copper ions, and open boxes indicate daunomycin molecules). (b) The central part of a bridge shown on an enlarged scale.

0021-3640/05/8106-0264$26.00

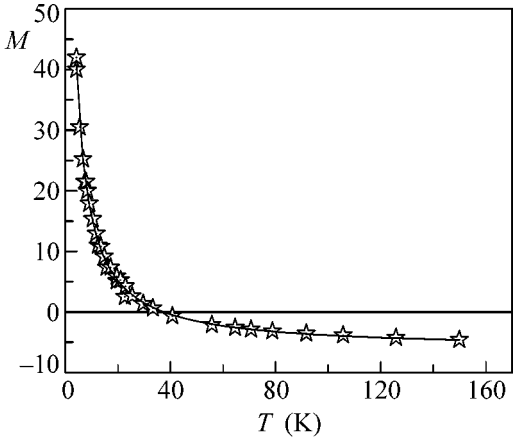

Fig. 2. Temperature dependence of the number of quanta M, which is proportional to the magnetic flux generated by the magnetized sample. The number M is proportional to the magnetic moment (P_m) of the test sample.

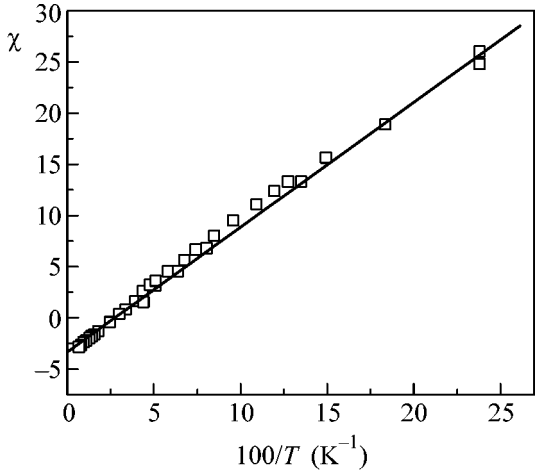

Fig. 3. Temperature dependence of the magnetic susceptibility χ. The value of χ is expressed in ~10^{-8} emu/Oe (1 CGS unit Oe^{-1}).

Low-temperature magnetic susceptibility measurements were performed on a SQUID magnetometer [6] in a magnetic field of 71.29 mT at temperatures ≥4.2 K. Cooling to helium temperatures was performed in a zero field; then, the magnetic field was introduced and the temperature was increased to 100 K. Next, cooling to helium temperatures was performed but in the magnetic field. We measured the number of quanta (M), which is proportional to the magnetic flux generated by a magnetized sample.

RESULTS AND DISCUSSION

Figure 2 demonstrates the temperature dependence of the number of quanta, which is proportional to the magnetic flux of the sample. The number M is proportional to the magnetic moment (P_m) of the test sample. Using the experimental data on the temperature dependence of the magnetic moment, we calculated the magnetic susceptibility of the sample as follows:

$$\chi = P_m/H,$$

where H is the applied magnetic field. The history of cooling and introducing the magnetic field had no effect on the results obtained.

It can be seen in Fig. 2 that both paramagnetic centers and a diamagnetic component contribute to the magnetic susceptibility. In this case, only Cu^{2+} ions are the paramagnetic centers. The main diamagnetic contribution is due to water and the benzene rings of daunomycin. The magnetic susceptibility is positive at low temperatures, whereas it is negative at high temperatures. Consequently, there are two contributions to the total magnetic moment: a positive paramagnetic contribution from doubly ionized Cu^{2+} ions and a negative diamagnetic contribution due to the presence of both water and daunomycin, which contains benzene rings, in the sample. We separated these two contributions by the mathematical treatment of the experimental temperature dependence of the magnetic susceptibility using the Curie–Weiss law with a constant term χ_0

$$\chi = \chi_0 + C_{CW}/(T - T_C),$$

where C_{CW} is the Curie–Weiss constant and T_C is the paramagnetic Curie temperature.

The resulting experimental functions $\chi(T)$ allowed us to perform important estimations. Let us assume that m_{DNA} is the mass of a single DNA molecule. In the test sample, the mass of a DNA molecule is approximately equal to 8×10^5 amu or $m_{DNA} = 1.34 \times 10^{-18}$ g. The concentration of the DNA in the solution is C_{DNA} = 0.00005 g/cm^3, and the volume of the solution from which the sample of the DNA nanoconstruction was obtained is equal to 80 cm^3. From these data, it follows that the total mass of DNA in the sample is M_{DNA} = 0.004 g. Consequently, the number of DNA molecules in the sample is $N_{DNA} = M_{DNA}/m_{DNA} = 3 \times 10^{15}$.

The effective magnetic moment was evaluated using an EPR experiment. The g-factor value was 2.09 at room temperature.

The effective magnetic moment of one Cu^{2+} atom in the sample can be estimated as follows:

$$\mu_{eff} = g\mu_B\sqrt{j(j+1)} = 1.82\mu_B.$$

From the temperature dependence of the magnetic moment (Fig. 3), we found $C_{CW} = 1.47 \times 10^{-6}$ erg K Oe^{-1}.

Let us denote the number of paramagnetic centers in the sample by N. The Curie–Weiss constant is related to N by the well-known equation (e.g., see [7])

$$C_{CW} = (\mu_{eff})^2 N/3k,$$

where k is the Boltzmann constant. Thus, we obtain

$$N = 3kC_{CW}/(\mu_{eff})^2.$$

From the above relationship, we estimate that $N = 1.96 \times 10^{18}$. Consequently, there are approximately $N/N_{DNA} = 716$ Cu^{2+} atoms per DNA molecule.

The number of coils in a DNA molecule is $(8 \times 10^5)/(6.6 \times 10^3) = 120$. Consequently, there are 716/120 = 5.9 (~6) copper atoms per DNA coil. If all these copper atoms participate in the formation of a nanobridge, six copper atoms are the constituents of a nanobridge between the coils of neighboring DNA molecules. This estimate is consistent with the results of theoretical calculations [3], according to which the bridge includes four to six copper atoms. Note that the calculations and models developed previously [3] are based on the assumption that all the bridges are formed in a quasi-nematic plane of the liquid-crystalline dispersion (see Fig. 1). If some bridges are out of this plane and the total number of bridges is higher than the number of DNA coils in the sample, the number of copper ions that are the constituents of a single bridge is less than six.

The diamagnetic contribution of the sample can also be evaluated from the experimental dependence. Approximation gives the total diamagnetic contribution of the magnetic moment $P_{diam} = -2.7 \times 10^{-5}$ emu. Both daunomycin and water contribute to diamagnetism. However, based on the experimental data, we cannot quantitatively separate these contributions.

Thus, the results of magnetometric measurements indicate that both the structural model of nanobridges developed previously [1–3] and the nanostructure based on double-stranded DNA molecules seem realistic. Note that the structure of regularly arranged nanobridges in a liquid-crystalline dispersion of DNA is similar to a spin lattice (Fig. 1), and it can be of considerable interest in nanotechnologies.

We are grateful to A.N. Vasil'ev and Yu.A. Koksharov for helpful discussions and their assistance in EPR experiments.

REFERENCES

1. Yu. M. Evdokimov, V. I. Salyanov, Yu. D. Nechipurenko, *et al.*, Mol. Biol. (Moscow) **37**, 340 (2003) [Mol. Biol. **37**, 293 (2003)].
2. Yu. D. Nechipurenko, M. A. Zakharov, V. I. Salyanov, and Yu. M. Yevdokimov, Biofizika **47**, 600 (2002) [Biophysics **47**, 557 (2002)].
3. Yu. D. Nechipurenko, V. F. Ryabokon', S. V. Semenov, and Yu. M. Yevdokimov, Biofizika **48**, 802 (2003) [Biophysics **48**, 594 (2003)].
4. A. Wells, *Structural Inorganic Chemistry* (Clarendon, Oxford, 1984; Mir, Moscow, 1988), Vol. 3, pp. 223–286.
5. Yu. M. Yevdokimov, V. I. Salyanov, B. V. Mchedlischvili, *et al.*, Nucleoside Nucleotides Nucleic Acids **19**, 1355 (2000).
6. V. D. Kuznetsov, Prib. Tekh. Éksp., No. 4, 196 (1985).
7. S. V. Vonsovskiĭ, *Magnetism* (Nauka, Moscow, 1971; Wiley, New York, 1974).

Translated by V. Makhlyarchuk

JETP Letters, Vol. 81, No. 6, 2005, pp. 267–271. Translated from Pis'ma v Zhurnal Éksperimental'noĭ i Teoreticheskoĭ Fiziki, Vol. 81, No. 6, 2005, pp. 330–334.

Magnetic-Field-Induced Singularity in the Tunneling Current Through an InAs Quantum Dot

Yu. N. Khanin and E. E. Vdovin

Institute of Microelectronics Technology and High Purity Materials, Russian Academy of Sciences, Chernogolovka, Moscow region, 142432 Russia

e-mail: vdovin@ipmt-hpm.ac.ru

Received February 15, 2005

The tunneling transport through a GaAs/(AlGa)As/GaAs single-barrier heterostructure with self-assembled InAs quantum dots is studied experimentally at low temperatures. An anomalous increase in the tunneling current through the quantum dots is observed in magnetic fields both parallel and perpendicular to the current. This result cannot be understood in the framework of the single-electron approximation. The proposed explanation of the phenomenon is based on the modified Matveev–Larkin theory, which predicts the appearance of a singularity in the tunneling current through the zero-dimensional state in a magnetic field because of the interaction between the tunneling electron and the spin-polarized three-dimensional electron gas in the emitter. The absence of spin splitting in the experimental resonance peaks is caused by the complete spin polarization of the emitter in relatively weak magnetic fields. © *2005 Pleiades Publishing, Inc.*

PACS numbers: 71.55.Eq, 73.21.–b, 73.40.Gk

Quantum dots are nanoobjects in which the electron motion is restricted in three spatial directions. As a result, a quantum dot is characterized by a set of discrete electron energy levels similar to an atomic spectrum. The resonant tunneling through zero-dimensional states was studied earlier, and the behavior of such systems at very low temperatures (in the millikelvin range) often could not be explained in terms of the single-electron approximation. This is not surprising, because the effects caused by the electron–electron interaction, such as the Coulomb blockade [1], the Kondo effect [2], and the Fermi-edge singularity (FES) [3–9], manifest themselves at low temperatures and strongly affect the tunneling current. However, the recently observed effect seems surprising: the FES in the tunneling current through InAs quantum dots was considerably enhanced in a strong magnetic field parallel to the current [10], whereas no such enhancement of the FES occurred in a magnetic field perpendicular to the current [11].

In this paper, we report on the observation of an anomalous increase in the tunneling current through quantum dots in magnetic fields both parallel and perpendicular to the current and interpret it as a manifestation of the FES. We present the results of studying the tunneling transport through a heterostructure consisting of a single $Al_{0.4}Ga_{0.6}As$ barrier with self-assembled InAs quantum dots embedded into it at its center. The current–voltage characteristics, $I(V)$, of this sample exhibit a sharp increase in the tunneling current through a quantum dot in the magnetic field. This result cannot be explained in terms of the single-electron approximation. We propose an explanation of the phenomenon on the basis of the modified Matveev–Larkin theory, which predicts the appearance of a singularity in the tunneling current through a zero-dimensional state as a result of the strong interaction of a tunneling electron with the electron gas in the emitter. An analysis of the temperature dependence of the tunneling current confirms that the anomalous increase in the resonant current is attributed to its multiparticle component.

The experimental samples were asymmetric $GaAs/Al_{0.4}Ga_{0.6}As/GaAs$ single-barrier heterostructures containing a thin InAs layer at the barrier center (1.8 monolayer (ML)). The original heterostructure was grown by molecular beam epitaxy on substrates with the (100) surface orientation. The doping impurity was silicon, whose concentration in the substrates was 2×10^{18} cm^{-3}. The self-assembled InAs quantum dots were formed in the process of the growth of strained InAs epitaxial layers by the Stransky–Krastanov method. The typical size of the quantum dots and their surface concentration were determined by scanning tunneling spectroscopy of samples grown under the same conditions as the experimental samples and were found to be ~10 nm and 2×10^{11} cm^{-2}, respectively. The dot geometry was determined by transverse transmission electron microscopy for the sample used in the tunneling transport measurements. The dot height was found to be ~2–3 nm. The additional InAs monolayer, whose thickness was smaller than the critical thickness (1.2 ML) necessary for the formation of self-assembled quantum dots, was grown near the $Al_{0.4}Ga_{0.6}As$ barrier for studying the process of tunneling from the two-

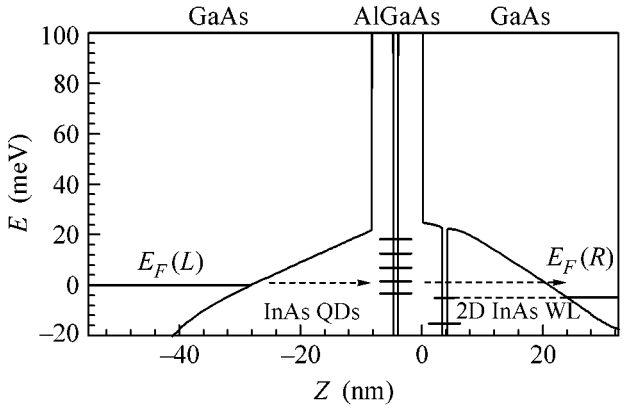

Fig. 1. Calculated potential profile of the active part of the experimental structure at a positive bias voltage of 5 meV. The arrows indicate the direction of the electron current.

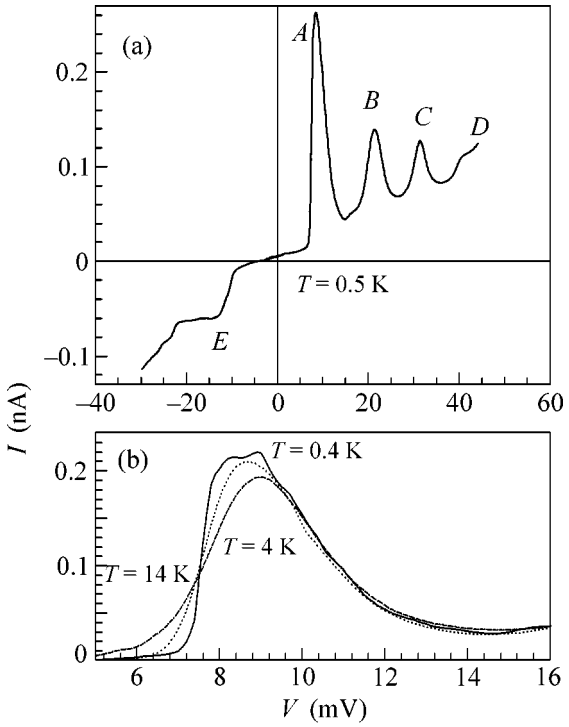

Fig. 2. Current–voltage characteristic of the (a) experimental sample at $T = 0.5$ K and (b) first resonance peak at temperatures of (solid curve) 0.5, (dotted curve) 1.4, and (dash–dotted curve) 4 K.

dimensional InAs (WL) layer to InAs quantum dots (these processes are not considered in this work). The ohmic contacts were fabricated by the sequential deposition of AuGe/Ni/Au layers with a subsequent annealing at $T = 400$°C. To obtain a mesostructure with a diameter of 20–100 μm, we used a standard chemical etching procedure. Figure 1 shows the bottom profile calculated for the conduction band of our heterostructure at the bias voltage $V = 5$ mV. The presence of InAs quantum dots in the barrier leads to the formation of a set of discrete zero-dimensional electron states. In the absence of bias, electrons diffuse from the doped GaAs contacts to the states of the two-dimensional InAs quantum well (WL), and the negative charge accumulated there causes a depletion of the layers adjacent to the $Al_{0.4}Ga_{0.6}As$ barrier (see Fig. 1). When the bias voltage is applied, the electron tunneling from the three-dimensional (3D) GaAs emitter to the discrete electron states in the quantum dots gives rise to peaks in the current–voltage characteristic. A peak appears in the current when the energy of the quantum dot coincides with the Fermi energy of the emitter. In what follows, we consider the bias voltage as positive when the electron tunneling occurs from the substrate through the quantum dots in the barrier, from left to right, as shown in Fig. 1. The current–voltage characteristics were obtained by the standard measuring technique with a noise level below 30 fA. The measurements were performed in the temperature range from 370 mK to 4.2 K and in magnetic fields up to 12 T.

Figure 2a shows the current–voltage characteristic of the experimental sample at $T = 0.5$ K. The curve exhibits a series of sharp peaks in the voltage interval from 8 to 50 mV at positive bias voltages. These peaks marked as *A*, *B*, *C*, and *D* are manifestations of the resonant electron tunneling through InAs quantum dots in the (AlGa)As barrier. The curve also has step *E* caused by the Coulomb blockade at a negative bias. The positions of the peaks and their heights are different for different samples, but they are completely reproducible for every single sample even after its thermal cycling. The difference in the shape of the resonance features that are observed for different directions of bias voltage is explained by the asymmetry of the barrier region in the heterostructure under study. Since the growth of quantum dots begins from the middle of the barrier layer and the dots have a finite height (~2–3 nm), the tunneling layer under a quantum dot (i.e., to the right of the InAs layer in Fig. 1) proves to be somewhat thicker than the tunneling layer above the dot. Hence, at a positive bias, the electron tunneling from the emitter to the quantum dot occurs much slower than the electron tunneling from the dot to the collector; i.e., $\Gamma_R \gg \Gamma_L$.

In what follows, we restrict our consideration to the behavior of the first peak (*A*), because it is the region where we observed the singularity of the tunneling current at a low temperature in a relatively strong magnetic field. Figure 2b shows the temperature dependence of resonance *A*. The shape of the resonance feature arising in the current–voltage characteristic due to the tunneling through the zero-dimensional state (0D) is determined by the dimension of the emitter [12]. A sharp threshold-type increase in the tunneling current occurs at a bias voltage V_0 at which the energy E_{QD} of the quantum dot state coincides with the Fermi energy E_F of the emitter. As the bias increases further, the resonant current decreases and vanishes at a voltage V_1 at which E_{QD}

coincides with the conduction-band bottom E_C in the emitter. Thus, the triangular shape of the resonant current feature with a sharp front should be observed in the case of the 0D–3D tunneling in the voltage interval between V_0 and V_1. Owing to nonzero temperature, the resonance front is smeared and the tunneling current is determined by the expression [13]

$$I \sim \frac{V_1 - V}{1 + \exp(\alpha e(V_0 - V)/kT)} \quad (V \le V_1), \qquad I = 0 \quad (V > V_1), \tag{1}$$

where α is the bias voltage-to-energy conversion factor. From the comparison of the experimental curves obtained at different temperatures with formula (1), we derive $\alpha \approx 0.44$ (see Fig. 2b). This α value agrees well with the value obtained from self-consistent calculations of the potential profile along the experimental structure in the voltage range 0–50 mV of interest. A self-consistent solution of the set of Poisson and Schrödinger equations was obtained by a numerical method similar to that described in [14]. As a result, these calculations allowed us to determine the Fermi energy of the emitter in the first resonance region as $E_F = \alpha(V_2 - V_1) = 2.4$ meV.

Now, we consider the transport characteristics of the experimental heterostructure in the magnetic field. Figure 3 shows the current–voltage characteristics of the sample in a magnetic field of 8 T perpendicular to the current for two different temperatures. The $I(V)$ curve obtained at $T = 3$ K exhibits four resonance features corresponding to tunneling through different states of quantum dots, as in the absence of the magnetic field. A decrease in temperature to 0.5 K drastically sharpens the edge of resonance A, which occurs at a bias voltage of 8 mV and corresponds to the threshold of tunneling through the lowest zero-dimensional state, but only slightly increases the heights of other resonance peaks. Such a small increase in the peak currents that are observed at 20, 30, and 40 mV can be explained by a decrease in the temperature broadening of the Fermi distribution for electrons in the emitter. However, the appearance of singularity in the current at a bias voltage of ~8 mV cannot be attributed only to the decrease in the aforementioned temperature broadening. The FWHM of this peak is as small as 0.3 mV, which corresponds to 130 μeV on the energy scale. This singularity represents a sharp growth of the tunneling current and its subsequent slower decrease with increasing bias. As we show below, this unexpected growth of the current in the magnetic field can be attributed to a manifestation of the Fermi-edge singularity in the tunneling through the localized state. A similar singularity was also observed in the magnetic field whose direction was parallel to the current (for the sake of brevity, we do not present here the corresponding curve). Again, we note that the singularity was not observed in the absence of the magnetic field even at the lowest temperature of ~0.4 K achieved in our experiments (see Fig. 2b).

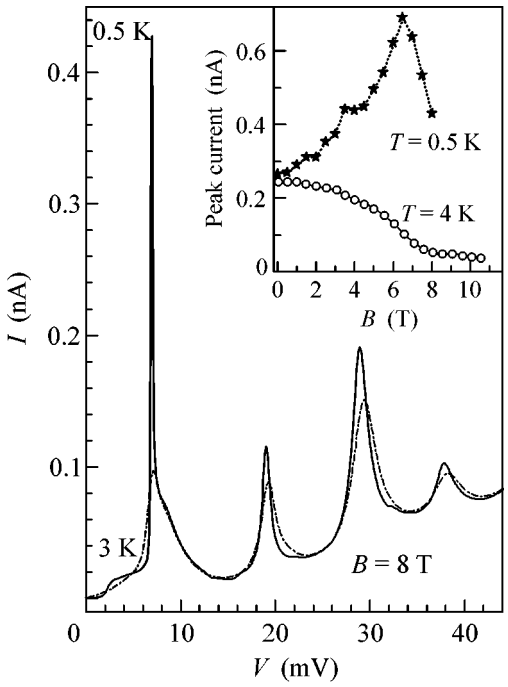

Fig. 3. Current–voltage characteristic of the experimental sample in a magnetic field of 8 T at two temperatures T = (solid curve) 0.5 and (dash–dotted curve) 3 K. The inset shows the peak current of peak A versus the magnetic field perpendicular to the current for the temperatures of (circles) 4 and (asterisks) 0.5 K.

Beyond the tunneling threshold, the $I(V)$ curve obtained at 0.4 K has only weak features, which are presumably associated with mesoscopic fluctuations of the density of electron states in the emitter [15].

The inset in Fig. 3 shows the dependence of the peak current of resonance A on the magnetic field B perpendicular to the tunneling current for temperatures of 4.2 and 0.5 K. The decrease in the peak current with increasing B may be attributed to the well-known effect that can be understood in terms of the single-particle model of electron tunneling in the magnetic field perpendicular to the current. This effect provides the basis of the method of visualization of electron wave functions in quantum dots with the use of magnetic tunneling spectroscopy and is described in detail in [16–18]. Peak value A at $T = 4$ K strongly depends on the orientation of the magnetic field in the growth plane (not shown in this paper). On the contrary, the amplitude of peak A at $T = 0.5$ K is virtually isotropic. This property is the result of the manifestation of an additional tunneling channel with electron–electron interaction at very low temperatures. The dependence of the efficiency of this channel on the magnitude and direction of the perpendicular magnetic field differs from the corresponding dependence characterizing the single-particle channel. For this reason, the shape of the wave functions of quantum dots cannot be measured in the same way as at ~4 K.

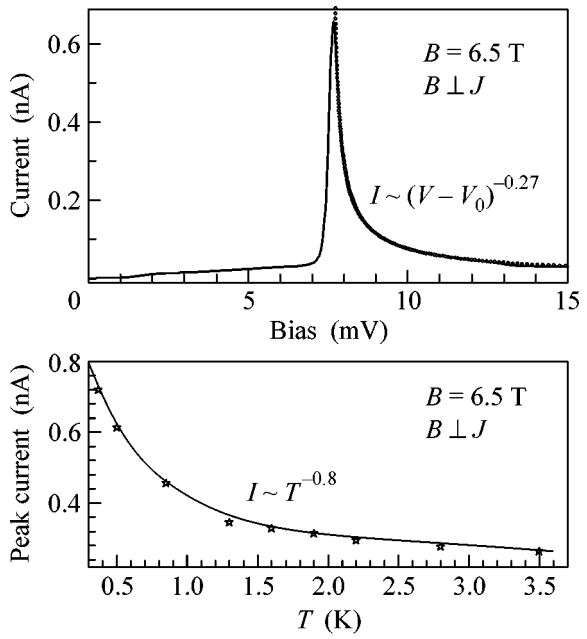

Fig. 4. (a) Current–voltage characteristic of the experimental sample in the first resonance region in a perpendicular magnetic field of 6.5 T at $T = 0.5$ K. The dotted curve shows the dependence $I \sim (V - V_0)^{-\gamma}$ with the exponent $\gamma \sim 0.77$. (b) The temperature dependence of the FES peak current (asterisks). The solid line represents the power-law dependence of the peak current $I_0 \sim T^{-\gamma}$ with the exponent $\gamma \sim 0.8$.

To determine the nature of the multiparticle current observed in our experiments, we analyzed the shape of the resonance features. Figure 4a shows in more detail the first (in voltage) resonance feature, i.e., peak *A*, observed in the perpendicular magnetic field $B = 8$ T at $T = 0.5$ K. We believe that the total current in Fig. 4a is predominantly determined by the tunneling channel with electron–electron interaction, because, as is clearly seen in the inset in Fig. 3, the single-electron current is suppressed by the magnetic field. This property allows us to analyze the shape of the experimental resonance feature and to compare it with theoretical predictions [3, 4]. The shape of the experimental peak, i.e., the sharp growth of the tunneling current and its subsequent decrease according to the exponential law $I \sim (V - V_0)^{-\gamma}$, where V_0 is the voltage corresponding to the peak current, is typical of a Fermi-edge singularity [3, 4]. For the curve shown in Fig. 4a and obtained at $B = 8$ T and $T = 0.5$ K, we obtain $\gamma = 0.77$, which far exceeds the value theoretically predicted for a similar experimental structure [3] in the absence of the magnetic field and is slightly higher than the γ value obtained in [10, 11] for the magnetic field $B = 28$ T applied in the direction parallel to the tunneling current.

The nature of the anomalous increase in the tunneling current through a quantum dot can also be determined by analyzing the temperature dependences of the current–voltage characteristics. According to [7], the increase in the area under the $I(V)$ curve in the resonance region when the temperature decreases unambiguously testifies to the multiparticle nature of the phenomenon. Our experimental curves clearly demonstrate this kind of behavior (see Fig. 3). In addition, an experimental study of the temperature dependences of the tunneling characteristics provides another possibility for determining the exponent γ [6, 10]. As is seen in Fig. 4b, the amplitude of peak *A* decreases as $I \sim T^{-\gamma}$ with $\gamma \sim 0.8$ when the temperature increases. Within the accuracy of the experiment, this value coincides with the γ value obtained from the shape of the resonance features of the current–voltage characteristics in the region of $V > V_0$. Thus, the analysis of the temperature dependences additionally and independently confirms the conclusion that the anomalous increase in the tunneling current with decreasing temperature and increasing magnetic field is associated with the manifestation of the interaction between the tunneling electron and the electron gas in the emitter (i.e., with the FES).

However, it should be noted that the very high exponent $\gamma \sim 0.8$ cannot be explained in terms of the existing FES theory (which is applicable only for $\gamma \ll 1$ [3] when the γ value is determined by the Fermi energy and tunneling length) without its modification. An enhancement of the FES similar to that recorded by us was recently observed in very strong magnetic fields parallel to the current for tunneling through InAs quantum dots in single-barrier heterostructures [10, 11]. In this work, a modified model of the FES has been proposed and it has been shown that the interaction between the localized charge in a quantum dot and the electrons in the 3D emitter can lead to a considerable Fermi-edge singularity if only the last spin-degenerate Landau level is filled with electrons. Such an interaction gave rise to an FES with $\gamma \sim 0.5$ in strong magnetic fields (~30 T). In our experiments, the Fermi energy in the 3D emitter at bias voltages near peak *A* was equal to 2.4 meV, which was approximately one sixth of the corresponding value in [10, 11]. Thus, the 3D emitter in our heterostructure at 8 T proved to be completely spin-polarized, and we could observe the FES with $\gamma \sim 0.8$ in relatively weak magnetic fields. Note that the complete spin polarization of electrons in the emitter prevented the observation of the Zeeman splitting of zero-dimensional states in our experiments.

Finally, we stress that a strong FES has been observed in both parallel and perpendicular magnetic fields. Although the 3D emitter is quantized in magnetic fields of both directions, the theoretical description of the FES for the perpendicular field should presumably be somewhat different from that proposed in [10, 11]. In our opinion, this issue requires further detailed investigation.

Thus, we observed an anomalous increase in the tunneling current through quantum dots in a magnetic field. This increase cannot be explained in terms of the single-electron approximation. We proposed an expla-

nation of the phenomenon on the basis of the modified Matveev–Larkin theory, which predicts the appearance of a singularity in the tunneling current through the zero-dimensional state as a result of the interaction between the tunneling electron and the electron gas in the emitter.

We are grateful to M. Henini and Prof. L. Eaves for placing heterostructures at our disposal and to A.V. Khaetskii, I.A. Larkin, and Yu.V. Dubrovskii for numerous discussions and their interest in our work. This work was supported in part by the Russian Foundation for Basic Research (project nos. 03-02-17693 and 04-02-16869).

REFERENCES

1. L. P. Kouwenhoven, C. M. Marcus, P. L. McEuen, *et al.*, in *Mesoscopic Electron Transport*, Ed. by L. L. Sohn, L. P. Kouwenhoven, and G. Schon (Kluwer, Dordrecht, 1997), p. 105.
2. D. Goldhaber-Gordon, J. Cores, M. A. Kastner, *et al.*, Nature **391**, 156 (1998); S. M. Cronenwett *et al.*, Science **281**, 540 (1998).
3. K. A. Matveev and A. I. Larkin, Phys. Rev. B **46**, 15337 (1992).
4. G. E. W. Bauer, Surf. Sci. **305**, 358 (1994).
5. A. K. Geim, P. C. Main, N. La Scala, Jr., *et al.*, Phys. Rev. Lett. **72**, 2061 (1994).
6. D. H. Cobden and B. A. Muzykantskii, Phys. Rev. Lett. **75**, 4274 (1995).
7. C. Zhang, D. J. Fisher, and S. M. Stewart, Surf. Sci. **361/362**, 231 (1995).
8. K. A. Benedict, A. S. G. Thornton, T. Ihn, *et al.*, Physica B (Amsterdam) **256/258**, 519 (1998).
9. D. A. Abanin and L. S. Levitov, Phys. Rev. Lett. **93**, 126802 (2004).
10. I. Hapke-Wurst, U. Zeitler, H. Frahm, *et al.*, Phys. Rev. B **62**, 12621 (2000).
11. I. Hapke-Wurst, Dissertation (Univ. Hannover, 2002).
12. H. C. Liu and G. C. Aers, J. Appl. Phys. **65**, 4908 (1989).
13. T. Suzuki, Y. Haga, K. Nomoto, *et al.*, Solid-State Electron. **42**, 1303 (1998).
14. I-H. Tan, G. L. Snider, L. D. Chang, and E. L. Hu, J. Appl. Phys. **68**, 4071 (1990).
15. T. Schmidt, R. J. Haug, V. I. Fal'ko, *et al.*, Phys. Rev. Lett. **78**, 1540 (1997).
16. E. E. Vdovin, A. Levin, A. Patane, *et al.*, Science **290**, 122 (2000).
17. E. E. Vdovin, Yu. N. Khanin, A. V. Veretennikov, *et al.*, JETP Lett. **74**, 41 (2001).
18. A. Patanè, R. J. A. Hill, L. Eaves, *et al.*, Phys. Rev. B **65**, 165308 (2002).

Translated by E. Golyamina

JETP Letters, Vol. 81, No. 6, 2005, pp. 272–276. Translated from Pis'ma v Zhurnal Éksperimental'noĭ i Teoreticheskoĭ Fiziki, Vol. 81, No. 6, 2005, pp. 335–340.

Magnetoelectric Effects in Gadolinium Iron Borate $GdFe_3(BO_3)_4$

A. K. Zvezdin[2], S. S. Krotov[1], A. M. Kadomtseva[1], G. P. Vorob'ev[1], Yu. F. Popov[1], A. P. Pyatakov[1], L. N. Bezmaternykh[3], and E. A. Popova[1]

[1] *Moscow State University, Vorob'evy gory, Moscow, 119992 Russia*
e-mail: Kadomts@plms.phys.msu.ru
[2] *Institute of General Physics, Russian Academy of Sciences, Moscow, 119991 Russia*
[3] *Kirenskiĭ Institute of Physics, Siberian Division, Russian Academy of Sciences, Akademgorodok, Krasnoyarsk, 660036 Russia*

Received February 16, 2005

Magnetoelectric interactions have been investigated in a single crystal of gadolinium iron borate $GdFe_3(BO_3)_4$, whose macroscopic symmetry is characterized by the crystal class 32. Using the results of this study, the interplay of magnetic and electric orderings occurring in the system has been experimentally revealed and theoretically substantiated. The electric polarization and magnetostriction of this material that arise in spin-reorientation transitions induced by a magnetic field have been investigated experimentally. For $H \parallel c$ and $H \perp c$, H–T phase diagrams have been constructed, and a strict correlation between the changes in the magnetoelectric and magnetoelastic properties in the observed phase transitions has been ascertained. A mechanism of specific noncollinear antiferroelectric ordering at the structural phase transition point was proposed to interpret the magnetoelectric behavior of the system within the framework of the symmetry approach in the entire temperature range. This ordering provides the conservation of the crystal class of the system when the temperature decreases to the antiferroelectric ordering point. The expressions that have been obtained for the magnetoelectric and magnetoelastic energy describe reasonably well the behavior of gadolinium iron borate observed experimentally. © *2005 Pleiades Publishing, Inc.*

PACS numbers: 75.80.+q

INTRODUCTION

In recent years, magnetoelectric materials (also known as multiferroics) have attracted much attention. These materials have been known for more than half a century, but they have been of only academic interest until recently, because the magnetoelectric effect that was observed in them was very weak. Only recently, new interesting materials have been found in which this effect is sufficiently strong [1–3]. In addition, recent investigations have revealed another manifestation of magnetoelectric interactions, namely, the possibility of controlling the magnetic state of a substance by an electric field and vice versa [4–9]. In particular, electric domains in such materials as $TbMnO_3$ and $GdMnO_3$ were switched by a magnetic field [4–6]. These new effects provide promising prospects for applications, but many fundamental questions concerning the nature of these effects have not been clarified so far.

Among new multiferroics, gadolinium iron borate $GdFe_3(BO_3)_4$ [10–20] (one of the representatives of a new family of multiferroics—rare-earth iron borates $RFe_3(BO_3)_4$) is of considerable interest. Its crystal structure is characterized by the space group $R32$ (D_3^7). At $T_C = 156$ K, a structural phase transition is observed in gadolinium iron borate at which the translational symmetry of the crystal changes presumably without a change in the crystal symmetry class. This transition is accompanied by characteristic dielectric anomalies [20], which may serve as indirect evidence for the occurrence of antiferroelectric ordering in the crystal.

According to [18], Fe^{3+} spins in gadolinium iron borate are ordered antiparallel in the basal plane at $T < T_N = 38$ K (AF1 phase). At $T_R = 10$ K, another phase transition occurs at which the Fe^{3+} spins are reoriented from the easy plane (AF1) to the easy axis c (AF2). For this reason, we expected a substantial manifestation of magnetoelectric interactions and their transformations in phase transitions accompanied by a change in the magnetic symmetry in gadolinium iron borate, which has a noncentrosymmetric symmetry group. Since information on this aspect in the behavior of rare-earth iron borates is unavailable in the literature, the magnetoelectric and magnetoelastic properties of $GdFe_3(BO_3)_4$ in phase transitions induced by a magnetic field have been studied both experimentally and theoretically in this work.

EXPERIMENTAL RESULTS

The longitudinal electric polarization and magnetostriction of a $GdFe_3(BO_3)_4$ single crystal were measured in magnetic fields up to 100 kOe for $H \parallel c$ and $H \perp c$ in the temperature range 4.2–50 K by the proce-

dure described in [21]. It was found that the magnetic field below T_N induced the rearrangement of the magnetic structure in this compound that was accompanied by the occurrence of the magnetoelectric effect and magnetoelastic deformations. The field dependences of the electric polarization and magnetostriction were drastically different for $H \parallel c$ and $H \perp c$. Thus, the magnetoelectric effect and magnetostriction for $H \parallel c$ were observed only at temperatures of $T < 10$ K, vanishing in the temperature range 10 K < T < 38 K. This presumably indicates that a change in the symmetry occurred near T_R. For $H \perp c$, anomalies in the magnetoelectric effect and magnetostriction were observed for all temperatures below T_N.

The field dependences of the longitudinal magnetostriction and electric polarization in the low-temperature region for $H \parallel c$ are presented in Fig. 1. It is evident that jumps in the electric polarization $P_C(H_C)$ and magnetostriction $\lambda_C(H_C)$ occur in the vicinity of 5 K at a certain critical field H_C^{crit} = 8 kOe, where a magnetic field-induced spin reorientation from the c axis to the easy plane was observed according to [16]. With increasing temperature, the threshold fields decrease and they vanish at T_R. For temperatures 10 K < T < 38 K, the longitudinal electric polarization and magnetostriction along the c axis exhibit no anomalies and depend monotonically (quadratically) on the field. The H_C^{crit}–T phase diagrams that are obtained from measurements of the magnetoelectric and magnetoelastic properties (Fig. 2) are in good agreement, which indicates that these properties evidently correlate with each other. For $H \perp c$, the character of the field dependences of the electric polarization and magnetostriction changes qualitatively.

The field dependences of the longitudinal magnetostriction and electric polarization for $H \parallel a$ are presented in Fig. 3. It is seen that, at T = 4.5 K, the electric polarization and magnetostriction in low fields depend weakly on the magnetic field. Then, they increase abruptly at H_C^{crit} = 37 kOe, and the polarization jump at 4.5 K for $H \parallel a$ exceeds the polarization jump for $H \parallel c$ by a factor of 20. With increasing temperature from 4.2 K to T_R, the threshold fields for the AF2 ⇒ AF1 transition decrease strongly. Starting with T_R up to T_N, when the Fe^{3+} spins lie in the basal plane, the electric polarization and magnetostriction increase abruptly already in a relatively weak magnetic field of ~2 kOe and, then, vary monotonically when the field increases.

The H_a^{crit}–T phase diagrams for $H \perp c$ (Fig. 4) that are plotted using the electric polarization and magnetostriction isotherms (Fig. 3) in the same way as for $H \parallel c$ (Fig. 2) are in good agreement with each other. This indicates that the magnetoelectric and magnetoelastic properties that are measured for the $H \parallel c$ and $H \perp c$ orientations of the magnetic field strictly correlate with each other. The experimental results indicate that jumps arise in the electric polarization vector **P** when the magnetic field reorients the $GdFe_3(BO_3)_4$ single crystal from the AF2 to AF1 phase. This behavior certainly points to the occurrence of ferroelectric properties in this crystal.

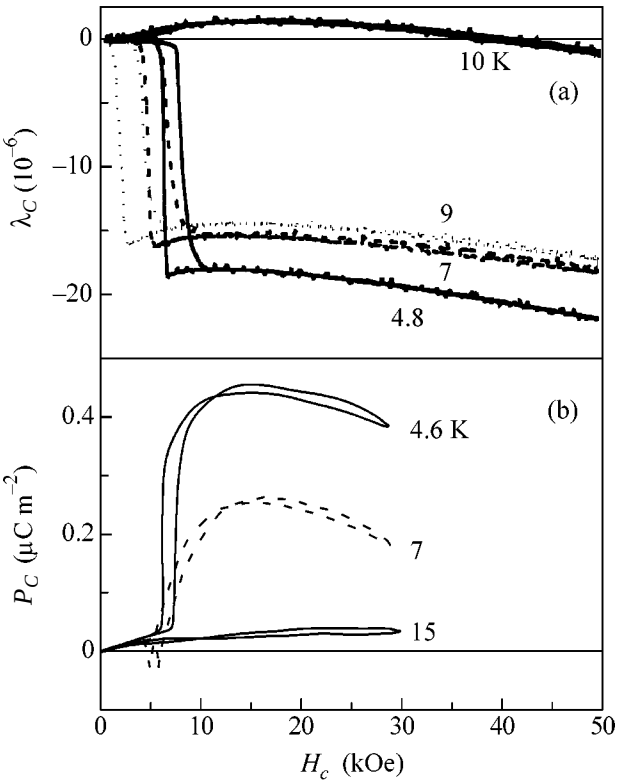

Fig. 1. Isotherms of longitudinal (a) magnetostriction and (b) electric polarization vs. the magnetic field directed along the c axis for the $GdFe_3(BO_3)_4$ single crystal.

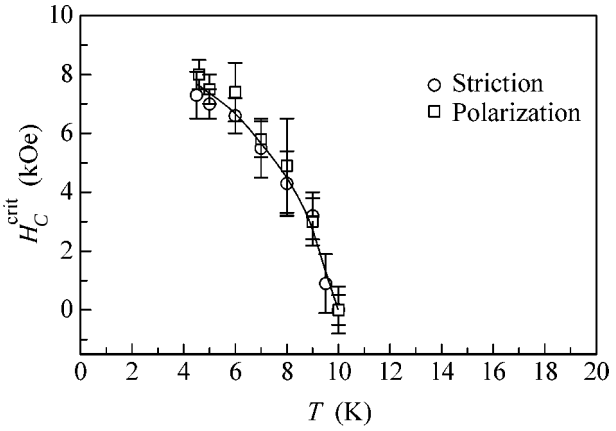

Fig. 2. *H–T* phase diagram obtained from measurements of magnetostriction and electric polarization in the $GdFe_3(BO_3)_4$ single crystal for $H \parallel c$.

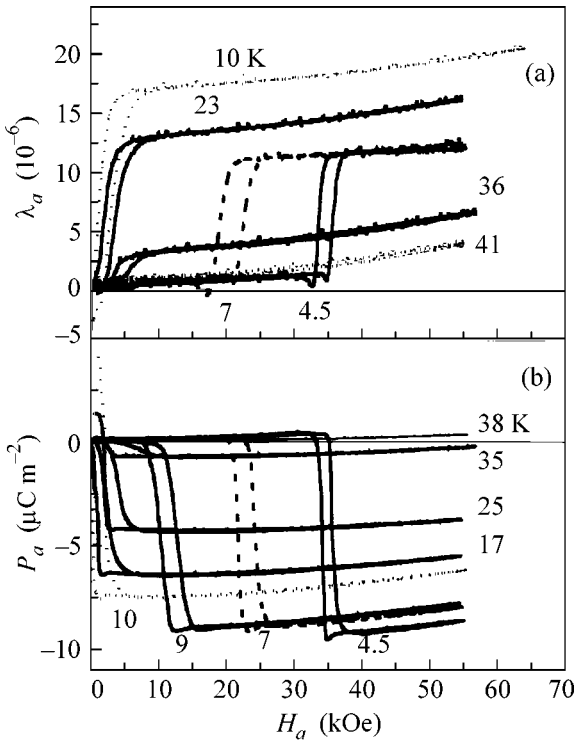

Fig. 3. Same as in Fig. 1 but for the magnetic field directed along axis *a*.

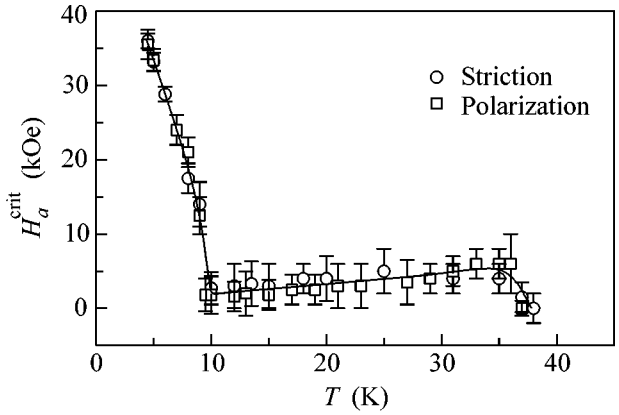

Fig. 4. Same as in Fig. 2 but for $H \parallel a$.

THEORETICAL PART

In this work, a theoretical model for the magnetoelectric structure of gadolinium iron borate is proposed to qualitatively explain the observed magnetoelectric properties of the material. Magnetic measurements and measurements of the antiferromagnetic resonance spectra [18] allow the conclusion that an antiferromagnetic collinear structure that is characterized by the antiferromagnetic vector **L** is realized in this material at $T < T_N$. Therefore, we will take the model proposed in [18] for the magnetic structure of gadolinium iron borate as the basis for the subsequent analysis. Because the vector **L** for $T_R < T < T_N$ lies in the basal plane, the crystallographic symmetry in this case changes evidently due to the spin–orbit interaction. Actually, if **L** is parallel to a second-order axis, the third-order axis (element 3) is eliminated from the set of the class 32 symmetry elements. As a result, class 32 changes to monoclinic class 2 characterized by the point group with a second-order symmetry axis as the generator. If **L** departs from the second-order axis, symmetry element 2 also disappears. As a result, class 2 passes into trivial class 1. Both these classes (2 and 1), as distinct from 32, allow the occurrence of a polar vector, and this gives a clue to the problem of the magnetoelectricity of gadolinium iron borate.

At the same time, the dielectric anomaly at the point T_C (namely, the jump in the dielectric constant when passing through T_C in the direction of decreasing temperature but with the retention of the crystal class 32) points to the possibility of realizing a compensated ferroelectric state for $T < T_C$, i.e., forming an antiferroelectric structure.

A natural model describing the mechanism of the occurrence of electric polarization upon magnetic ordering is the decompensation of zero total electric polarization ($\mathbf{P}_S = \mathbf{P}_1 + \mathbf{P}_2 + \mathbf{P}_3 \neq 0$) of the antiferroelectric (triangular) state (when $\mathbf{P}_S = 0$ for $T_N < T < T_C$). Here, $\mathbf{P}_1$, $\mathbf{P}_2$, and $\mathbf{P}_3$ are the polarization vectors of neighboring atomic layers spaced by one third of the vertical lattice constant. These vectors appear at the point T_C, and they are directed along the corresponding axes 2. This decompensation is very small due to the smallness of the spin–orbit interaction in the system of Fe^{3+} ions (which are *s* ions; i.e., their orbital angular momentum in the ground state equals zero). It can be responsible for the small increase observed in the dielectric constant of gadolinium iron borate when *T* decreases from T_N to T_R [20]. It is reasonable to expect that P_s increases with increasing the absolute value of **L**, which is the case when decreasing *T*. For $T < T_R$, a spin-reorientation transition to the $\mathbf{L} \parallel c$ phase occurs [17]. This phase is characterized by the point crystal group 32, in which the polar vector **P** is absent. Therefore, it may be expected that the magnetic field-induced transitions AF2 ⟶ AF1 will be accompanied by jumps in the electric polarization (and in the dielectric constant).

For deeper insight into the nature of the magnetoelectric interactions, the interplay between the electric polarization and the vector **L**, and the magnetic structure and orientational phase transitions of gadolinium iron borate, we consider the transformation properties of vector **L** and other quantities under the transformations of class 32. Note that the magnetic unit cell of gadolinium iron borate (in the direction of the *c* axis) is twice as large as the crystallographic one. This circumstance distinguishes the material under consideration

from typical objects in the symmetry theory of antiferromagnetism [22, 23], in which these cells are assumed to coincide. The evident way of overcoming this difficulty is to consider an extended (doubled) crystal unit cell of gadolinium iron borate and thus to return to the conventional approach. Following it, let us reduce the initial space group, assuming that the translations by the unit cell constants in the basal plane and the doubled translations along the c axis are equal to the identity transformation E. As a result, the reduced group $\tilde{G}_{32}$ can be characterized by the following generators: C_3, 2_x, and T_z where T_z is translation on the period of the unit cell along the c axis. The absolute values and orientations of these generators are completely determined by the state of the iron ions, because the other magnetic subsystem consisting of the Gd^{3+} ions is supposed to be paramagnetic. The generator T_z is odd; that is, this generator transforms one magnetic sublattice of the antiferromagnet into the other one $T_z\mathbf{L} = -\mathbf{L}$. At the same time, 2_x and C_3 are even; that is, they interchange atoms of the same sublattice $2_x\mathbf{L} = \mathbf{L}$, $C_3\mathbf{L} = \mathbf{L}$.

The transformation properties of the above reduced group offer the possibility of determining the symmetry of the magnetoelectric interaction and the desired interrelations between the magnetic structure and physical properties of the crystal. In Turov's terminology, the magnetic structure of gadolinium iron borate can be characterized by the code T_z^-, 3_z^-, 2_x^+. Note a certain analogy (but not the isomorphism!) of the structure under consideration with the magnetic structure of Cr_2O_3 with the code I^-, 3_z^-, 2_x^+ [22, 23], which has been comprehensively studied in the theory of antiferromagnetism.

The magnetoelectric interaction energy of the iron ion subsystem can be represented in the form[1]

$$E_{ME} = c_1L_z(P_xL_y - P_yL_x) + c_2[P_x(L_x^2 - L_y^2) + 2P_yL_xL_y] + c_3P_zL_xL_z(L_x^2 - 3L_y^2), \quad (1)$$

where c_1, c_2, and c_3 are the thermodynamic parameters of the symmetry theory. From Eq. (1), we will obtain the following equations determining the electric polarization vector $\mathbf{P}_s$, which spontaneously appears at the antiferromagnetic ordering point:

$$P_{sx} = c_1L_yL_z + c_2(L_x^2 - L_y^2) = C_1L^2\sin\theta\cos\theta\sin\varphi + C_2L^2\sin^2\theta\cos2\varphi, \quad (2a)$$

$$P_{sy} = -c_1L_xL_z + 2c_2L_xL_y = -C_1L^2\sin\theta\cos\theta\cos\varphi + C_2L^2\sin^2\theta\sin2\varphi, \quad (2b)$$

$$P_{sz} = c_3L_xL_z(L_x^2 - 3L_y^2) = C_3L^4\sin^3\theta\cos\theta\cos3\varphi, \quad (2c)$$

where θ and φ are the polar and azimuth angles of the vector $\mathbf{L}$.

According to the $\tilde{G}_{32}$ symmetry, the linear magnetoelectric effect is forbidden in gadolinium iron borate, which is confirmed experimentally [19]. We emphasize a certain similarity (and distinctions!) between Eq. (2c) and the equation for P_z in the case of Cr_2O_3 [21], which reflects the similarity and distinction between the corresponding magnetic structures and between the groups 32 and $\bar{3}m$.

A symmetry analysis also provides the following expression for the magnetoelastic energy:

$$\begin{aligned}\Delta\Phi_{\text{Mel}} &= \gamma_1u_{zz}L_z^2 + \gamma_2u_{zz}(L_X^2 + L_Y^2)\\ &+ \gamma_3[(u_{XX} - u_{YY})(L_X^2 - L_Y^2) + 2u_{XY}L_XL_Y]\\ &+ \gamma_4(2u_{XZ}L_XL_Z + u_{YZ}(L_X^2 - L_Y^2))\\ &+ \gamma_5(L_YL_Z(u_{XX} - u_{YY}) + u_{XY}L_XL_Z)\\ &+ \gamma_6(L_XL_Zu_{XZ} + L_YL_Zu_{YZ})\\ &+ \gamma_7u_{ZZ}([L_X^2 - L_Y^2] + 2L_x^2)L_YL_Z,\end{aligned} \quad (3)$$

from which the following formulas for magnetostriction can readily be obtained:

$$\begin{aligned}u_{zz} &= \gamma_1L_z^2 + \gamma_2(L_X^2 + L_Y^2) + \gamma_7([L_X^2 - L_Y^2] + 2L_X^2)L_YL_Z;\\ u_{XX} - u_{YY} &= \gamma_3(L_X^2 - L_Y^2) + \gamma_5L_YL_Z;\\ u_{XY} &= 2\gamma_3L_XL_Y + \gamma_5L_XL_Z;\\ u_{XZ} &= \gamma_42L_XL_Y + \gamma_6L_XL_Z;\\ u_{YZ} &= \gamma_6L_YL_Z + \gamma_4(L_X^2 - L_Y^2).\end{aligned} \quad (4)$$

Note that linear piezomagnetism, that is, the linear coupling between the elastic deformations and the external magnetic field, is forbidden in space group 32.

The above mechanism of symmetry breaking through magnetic ordering offers another view on Eqs. (2) for spontaneous electric polarization. Namely, the electric polarization in a crystal can be considered as a result of the double action: the spontaneous magnetostriction $u_{ik} = \delta_{iklm}L_lL_m$ and the piezoelectric effect $P_\alpha = \pi_{\alpha i}u_{ik}$, where δ_{iklm} and $\pi_{\alpha ik}$ are the magnetoelastic and piezoelectric tensors, respectively. Both tensors differ from zero in the crystals of class 32.

The multiplication of the tensors δ_{iklm} and $\pi_{\alpha ik}$ results in formulas for P_x and P_y that coincide with those given by Eqs. (2). Certainly, this coincidence does not mean that the coefficients are equal to the

[1] Rare-earth ions are paramagnetic and, in principle, do not change the equations given below (for $T \gg T_{\text{RN}}$, where T_{RN} is the ordering temperature of rare-earth elements). The inclusion of these ions leads only to the renormalization of coefficients. Therefore, having in mind a qualitative interpretation of the experiment, we will not complicate the equations by taking into account the rare-earth subsystem. Such a situation is typical for many *d–f* compounds with an antiferromagnetic *d* subsystem [24].

products of the components of the tensors π and δ. These coefficients can also depend on intrinsic microscopic magnetoelectric interactions. The component P_z in this "piezoelastic" consideration is naturally equal to zero, because this component, according to more detailed Eqs. (2), is determined by the terms of the fourth order in **L**; i.e., it is a small value (in the spin–orbit coupling constant) as compared to P_x and P_y, and this relation is manifested experimentally.

Another fourth-order combination of the components L_i is $((L_x^2 - L_y^2) + 2L_x^2)L_yL_z = L^4\sin^3\theta\cos\theta\sin 3\varphi$. This combination is an invariant of the group $\tilde{G}_{32}$; that is, it transforms by the representation Γ_1. It is linear in L_z. Therefore, the spins in the AF1 phase can be departed from the basal plane at a small angle (because the corresponding invariant is of the fourth order in L_i). This fact in combination with Eq. (2c) can be used to explain the small jump in the P_z component of the electric polarization upon the AF2 $\longrightarrow$ AF1 reorientation.

The above consideration was mainly devoted to the magnetic ordering (and magnetic field) effect on the electric polarization in gadolinium iron borate. However, Eqs. (2) allow an interesting generalization to the reverse crossing effects, that is, the electric field effects on magnetism and magnetic transformations [7–9]. Actually, substituting E_i for P_i in Eq. (1), which is evidently allowed by symmetry, we obtain the energy of interaction between the external electric field and vector **L**. The new effects arising in this case will be considered in a separate paper.

Thus, the magnetic symmetry of gadolinium iron borate and the model of the collinear antiferromagnetic structure proposed in [18] offer the possibility of explaining the jumps observed in the electric polarization and magnetostriction as a manifestation of spin-reorientation transitions induced by the magnetic field in this material. Expression (3) for the magnetoelastic interaction in gadolinium iron borate has been obtained using symmetry theory.

We are grateful to A.N. Vasil'ev and M.N. Popova for their interest in this work and useful discussions. This work was supported by the Russian Foundation for Basic Research, project nos. 04-02-16592, 04-02-81046-Bel2004-a, 05-02-16997-a, and 05-02-17719-a.

REFERENCES

1. J. Wang, H. Zheng, V. Nagarajan, *et al.*, Science **299**, 1719 (2003).
2. J. Li, J. Wang, M. Wuttig, *et al.*, Appl. Phys. Lett. **84**, 5261 (2004).
3. F. Bai, J. Wang, M. Wuttig, *et al.*, Appl. Phys. Lett. **86**, 1 (2005).
4. T. Kimura, T. Goto, H. Shintani, *et al.*, Nature **426**, 55 (2003).
5. T. Goto, T. Kimura, G. Lawes, *et al.*, Phys. Rev. Lett. **92**, 257201 (2004).
6. A. M. Kadomtseva, Yu. F. Popov, G. P. Vorob'ev, *et al.*, Pis'ma Zh. Éksp. Teor. Fiz. **81**, 22 (2005) [JETP Lett. **81**, 19 (2005)].
7. A. K. Zvezdin, Kratk. Soobshch. Fiz. (2005) (in press).
8. A. K. Zvezdin, Kratk. Soobshch. Fiz. (2005) (in press).
9. A. G. Zhdanov, A. K. Zvezdin, T. B. Kosykh, and A. P. Pyatakov, Fiz. Tverd. Tela (St. Petersburg) (2005) [Phys. Solid State (2005)] (in press).
10. D. A. Keszler, Solid State Mater. Sci. **1**, 204 (1996).
11. M. H. Bartl, K. Gatterer, E. Cavalli, *et al.*, Spectrochim. Acta A **57**, 1981 (2001).
12. A. M. Kalashnikova, V. V. Pavlov, R. V. Pisarev, *et al.*, Pis'ma Zh. Éksp. Teor. Fiz. **80**, 339 (2004) [JETP Lett. **80**, 293 (2004)].
13. A. G. Gavrilyuk, S. A. Kharlamova, I. S. Lyubutin, *et al.*, Pis'ma Zh. Éksp. Teor. Fiz. **80**, 482 (2004) [JETP Lett. **80**, 426 (2004)].
14. J. A. Campa, C. Cascales, E. Gutierrez-Puebla, *et al.*, Chem. Mater. **9**, 237 (1997).
15. Y. Hinatsu, Y. Doi, K. Ito, *et al.*, J. Solid State Chem. **172**, 438 (2003).
16. A. D. Balaev, L. N. Bezmaternykh, I. A. Gudim, *et al.*, J. Magn. Magn. Mater. **258–259**, 532 (2003).
17. R. Z. Levitin, E. A. Popova, R. M. Chtsherbov, *et al.*, Pis'ma Zh. Éksp. Teor. Fiz. **79**, 531 (2004) [JETP Lett. **79**, 423 (2004)].
18. A. I. Pankrats, G. A. Petrakovskiĭ, L. N. Bezmaternykh, and O. A. Baĭkov, Zh. Éksp. Teor. Fiz. **126**, 887 (2004) [JETP **99**, 766 (2004)].
19. A. M. Kadomtseva, Yu. F. Popov, S. S. Krotov, *et al.*, Fiz. Nizk. Temp. (2005) (in press).
20. A. N. Vasil'ev, private communication.
21. D. V. Belov, G. P. Vorob'ev, A. K. Zvezdin, *et al.*, Pis'ma Zh. Éksp. Teor. Fiz. **58**, 603 (1993) [JETP Lett. **58**, 579 (1993)].
22. E. A. Turov, Usp. Fiz. Nauk **164**, 325 (1994) [Phys. Usp. **37**, 303 (1994)].
23. E. A. Turov, A. V. Kolchanov, V. V. Men'shenin, I. F. Mirsaev, and V. V. Nikolaev, *Symmetry and Physical Properties of Antiferromagnetics* (Fizmatlit, Moscow, 2001) [in Russian].
24. K. P. Belov, A. K. Zvezdin, A. M. Kadomtseva, and R. Z. Levitin, *Orientational Transitions in Rare-Earth Magnets* (Nauka, Moscow, 1979) [in Russian].

Translated by A. Bagatur'yants

JETP Letters, Vol. 81, No. 6, 2005, pp. 277–283. From Pis'ma v Zhurnal Éksperimental'noĭ i Teoreticheskoĭ Fiziki, Vol. 81, No. 6, 2005, pp. 341–347.

Variable-Range Cotunneling and Conductivity of a Granular Metal¶

M. V. Feigel'man and A. S. Ioselevich

Landau Institute for Theoretical Physics, Russian Academy of Sciences, Moscow, 119334 Russia
e-mail: feigel@landau.ac.ru; iossel@landau.ac.ru

Received February 21, 2005

The Efros–Shklovskii (E–S) law for the conductivity of granular metals is interpreted as a result of a variable-range cotunneling process. The cotunneling between distant resonant grains is predominantly elastic at low $T \le T_c$, while it is inelastic (i.e., accompanied by creation of electron-hole pairs on a string of intermediate nonresonant grains) at $T \ge T_c$. The corresponding E–S temperature T_{ES}, in the latter case, is slightly (logarithmically) T dependent. The magnetoresistance in the two cases is different: it may be relatively strong and negative at $T \ll T_c$, while, at $T > T_c$, it is suppressed due to inelastic processes, which destroy the interference. © *2005 Pleiades Publishing, Inc.*

PACS numbers: 73.23.Hk, 73.43.Qt, 73.63.–b

INTRODUCTION

The low-temperature conductivity of most granular metals (both three-dimensional samples and thin films) exhibits a typical insulating behavior, which is characterized by the Efros–Shklovskii (E–S) law

$$\sigma \sim e^{-\sqrt{T_{ES}/T}}. \quad (1)$$

In samples with low room-temperature conductivity, this law is observed in the whole range of T (from room temperature down to liquid helium temperatures) [1–3]. Two ingredients are known to be necessary [4, 5] for the existence of the behavior (1) in usual doped semiconductors with localized impurity centers: (i) soft Coulomb gap in the electron density of states, and (ii) long-range electron tunneling between distant centers of their localization. The original idea on the building of the Coulomb gap as presented in [4] was recently adapted to granular arrays in [6]. It was argued that the principal source for this gap is random background charges, and the physical mechanisms behind these charges were discussed in detail. Feature (ii) is quite natural for doped semiconductors, as it follows from exponential decay of wave functions of localized electrons. It is much less trivial for granular media, where each grain is typically connected by tunnel junctions to its nearest neighbors only; therefore, the very origin of long-range tunneling needs some special explanation.

In this Letter, we demonstrate that the variable-range hopping in a granular metal involves the so-called cotunneling process [7] (either elastic or inelastic). Elastic cotunneling is effective if the temperature is low enough (namely, for $T < T_c \sim \mathcal{L}^{-1}(\delta E_C)^{1/2}$, where δ is the characteristic level spacing in the grains, E_C is the characteristic charging energy, and $\mathcal{L} \sim 10$ is a large logarithmic factor; see below). At $T > T_c$, the conductivity is dominated by inelastic cotunneling processes. We directly show this for the case of a granular metal with poor room-temperature conductivity (small intergrain conductances $g \equiv (h/e^2R) \ll 1$). We expect that the same is also true for samples with moderately good conductivity (cf., e.g., [8, 9]) with properly renormalized T_{ES}, but this more delicate issue will be discussed in a separate publication. Experimentally, the relative role of elastic verses inelastic cotunneling processes could be detected by the presence of noticeable low-field magnetoresistance in the hopping regime, while elastic cotunneling is expected to lead to negative magnetoresistance as was predicted for doped semiconductors [10–13]. Inelastic cotunneling is intrinsically incoherent, and the whole effect of the magnetic field upon conductivity is localized within individual grains and can, therefore, be only observed in very high fields $H \gtrsim 10$ T.

Cotunneling as a key mechanism of low-temperature charge transfer was proposed [7] and extensively discussed (cf., e.g., [14] for a review) with regard to transport via quantum dots. A quantum dot situated between two bulk metal reservoirs is characterized by its charing energy E_C and dimensionless conductances $g_{R,L}$. The semiclassical orthodox theory of Coulomb blockade [15] predicts exponential suppression of conductance through quantum dots at temperatures of $T \ll E_C$, i.e., $G_{\text{orth}} \propto \min(g_L, g_R)\exp(-E_C/T)$, due to the low probability of creation of a real state of dots with extra electron charge. The cotunneling process, on the other hand, occurs in the next order of perturbation theory in (small) tunneling amplitudes $t_{R,L}$ but does not contain

¶ This article was submitted by the authors in English.

an exponential suppression factor $\exp(-E_C/T)$, since the dot state with extra charge occurs as a virtual state only. One should distinguish two kinds of cotunneling processes: elastic and inelastic ones. The elastic process occurs when tunneling in and out of the dot deals with the same intradot electron eigenstate α; thus, it leaves the dot in exactly the same quantum state as it was before. In contrast, inelastic cotunneling leaves behind an excited electron-hole pair (since one electron tunnels in the dot and populates some eigenstate h, whereas another electron tunnels out of the dot from another pth eigenstate). Elastic cotunneling contributes to the conductance scales as $G_{\rm el} \propto g_L g_R \delta/E_C$, whereas the contribution from inelastic cotunneling is $G_{\rm inel} \propto g_L g_R (T/E_C)^2$; cf. [7, 14]. Thus, upon temperature decrease, first, inelastic cotunneling prevails over the classical conduction given by $G_{\rm orth}$; then, at $T_* \sim \sqrt{E_C \delta}$, it gives way to elastic cotunneling. Below, we generalize the above ideas to the situation of variable-range hopping in granular arrays.

In the spirit of the standard variable-range hopping (VRH) theory, we consider a charge transfer between two distant grains i and j with anomalously small energies ε_i, $\varepsilon_j \ll E_C$ of the charged ground state (i.e., the states with an extra electron or an extra hole; for an explicit definition of the energy ε and a detailed discussion of the corresponding density of ground states see [6]). Such a transfer between distant grains proceeds via a string of intermediate grains, where, typically, the energy of a state with an extra electron is high ($\varepsilon \sim E_C$). As in the case of a standard single-particle tunneling via resonant impurity states, the entire process is realized as a coherent sequence of local hops between adjacent grains in the string. There is an important difference, however. For the single-particle problem, where the same electron has to tunnel sequentially through all the impurities in the string (starting from the first one and ending with the last), the order of these local hops is fixed. In our case, there are many electrons in each grain, all these electrons being ready to tunnel to an adjacent grain at any time; consequently, the sequence of local hops in such a cotunneling process can be arbitrary. As a result, the states with a number of excited electrons and holes on different grains appear as intermediate virtual states of the cotunneling process and the number of charged grains in these intermediate states can be larger than one. In the final state, however, all the charges of the intermediate grains should be compensated for and the only extra charge is transferred between the two terminal grains of the string. The long-range hopping process involves many intermediate grains; in general, the cotunneling through some of them will be of the elastic type and, through others, it will be of the inelastic type. We will see below that elastic cotunneling dominates the variable-range hopping at rather low temperatures $T < T_c$, where T_c is significantly lower than in the case of a single intermediate quantum dot.

Note also that, in the case of not extremely low temperatures $T \gg \delta$ (when the spectrum of electrons in grains can be treated as a quasi-continuous one), one does not need to invoke phonons to ensure the energy conservation: the energy can be taken from the fermionic thermostat via the inelastic cotunneling process.

GENERAL APPROACH TO VARIABLE-RANGE COTUNNELING

The Hamiltonian of the system has the form $\hat{H} = \hat{H}_0 + \hat{H}_{\rm tun} + \hat{H}_C$. Here, the single-grain hamiltonian $\hat{H}_0 = \sum_i \hat{H}_0^{(i)}$, and the inter-grain tunneling hamiltonian $\hat{H}_{\rm tun} = \sum_{\langle ij \rangle} \hat{H}_{\rm tun}^{(ij)}$; in the latter, the summation runs over the pairs $\langle ij \rangle$ of neighboring grains

$$\hat{H}_0^{(i)} = \sum_{\alpha_i, \sigma} \epsilon_{\alpha_i} a^+_{\alpha_i \sigma} a_{\alpha_i \sigma}, \quad \hat{H}_{\rm tun}^{(ij)} = \sum_{\alpha_i, \alpha_j, \sigma} t_{\alpha_i \alpha_j} a^+_{\alpha_i \sigma} a_{\alpha_j \sigma},$$

where the operator $a^+_{\alpha_i \sigma}$ creates an electron in a single-particle orbital eigenstate α_i with a spin projection σ on a grain i. The Coulomb interaction hamiltonian

$$\hat{H}_C = \frac{1}{2} \sum_{ij} E_c^{(ij)} (\hat{n}_i - q_i)(\hat{n}_j - q_j), \qquad (2)$$

$\hat{n}_i = \sum_{\alpha_i, \sigma} a^+_{\alpha_i \sigma} a_{\alpha_i \sigma} - n_i^{(0)}$, being the operator of the excess number of electrons at the grain i, $n_i^{(0)}$, corresponds to the minimum of $\hat{H}_0 + \hat{H}_C$. The variables q_i (which are not necessarily integer!) are the so-called background charges (in the units of e). We will treat them as independent continuous random variables $-1/2 < q_i < 1/2$ with symmetric distribution $P(q)$. Two different limits should be distinguished: (i) the case of strong charge disorder, when the background charges are large, so that q_i is distributed homogeneously in the interval $-1/2 < q_i < 1/2$; and (ii) the case of weak disorder, when the charges are small, so that $q_0 \equiv (\overline{q^2})^{1/2} \ll 1$ and the probability to have $q = 1/2$, which is related to the bare density of ground states at the Fermi level (cf. [6]), is small: $P_{1/2} \equiv P(1/2) \ll 1$. While the former case seems to be most appropriate for a naturally disordered granular material, the latter one may be relevant for high quality artificial arrays of quantum dots.

If the tunnel matrix elements $t_{\alpha_i \alpha_j}$ are small enough, the rate w_{ij} of cotunneling between distant grains i and j can be found in the high order perturbation theory in $\hat{H}_{\rm tun}$:

$$w_{ij} = 2\pi f_F(\varepsilon_i) f_F(-\varepsilon_j) \sum_{\mathcal{P}} \sum_{\sigma_0, \{\sigma_l\}\{p_l, h_l\}\{\alpha_m\}} \sum_{k=1}^{N+1} \prod |t_{h_k p_{k-1}}|^2 f_F(\epsilon_{p_0}) f_F(-\epsilon_{h_{N+1}}) \prod_l f_F(\epsilon_{pl}) f_F(-\epsilon_{h_l})$$
$$\times \delta\left[\epsilon_{p_0} - \epsilon_{h_{N+1}} + \sum_l (\epsilon_{p_l} - \epsilon_{h_l}) - \Delta_{ij}\right] \sum_{\mathcal{T}, \mathcal{T}'} (-1)^{K(\mathcal{T}) - K(\mathcal{T}')} \prod_m \delta_{\lambda_m(\mathcal{T})\lambda_m(\mathcal{T}')} f_F[\lambda_m(\mathcal{T})\epsilon_{\alpha_m}] Q(\mathcal{T}) Q(\mathcal{T}'). \quad (3)$$

Here, we have assumed that the $i \longrightarrow j$ transition is dominated by tunneling along a unique string—a chain of neighboring grains denoted by the numbers $k = 0, 1, \ldots, N, N+1$, so that $0 \equiv i$ is the initial grain; $N+1 \equiv j$ is the final grain; and each pair k, $k+1$ are in contact. The possibility for several relevant strings to exist and the effect of interference of their contributions will be discussed in the last section of this Letter. The summation runs over all possible partitions $\mathcal{P}$ of the string into two subsets: $\{k\} = \{m\} \cup \{l\}$; on the grains $\{m\}$, elastic cotunneling (via a state h_m, $p_m \equiv \alpha_m$) occurs, while, at the grains $\{l\}$, inelastic cotunneling with the creation of an electron-hole pair with quantum numbers h_l, p_l takes place. The summation over all eigen-states α_m and pairs of eigenstates $h_l \neq p_l$ is assumed. The energies ϵ_{pl}, ϵ_{hl} are measured with respect to the Fermi level. The spin variable σ_0 corresponds to the state p_0 variables, and σ_l corresponds to the p_l components of electron-hole pairs. All the other spin variables are not independent because of the spin conservation by the tunneling hamiltonian. The spin summation gives the factor $2^{L(\mathcal{P})}$, where $L(\mathcal{P})$ is the number of inelastic grains in the partition $\mathcal{P}$. The interference cross terms between the processes with different α_m are neglected because of violent sign fluctuations of $t_{h_k p_{k-1}}$.

The time orderings $\mathcal{T}$ are all the possible orderings $\{k_1, k_2, \ldots, k_r, k_{N+1}\}$ of the set of grains $k = 0, \ldots, N$ (note that there is no final grain $N+1$ in this set!). The contribution to the composite transition amplitude $\hat{H}_{\text{eff}}^{(ij)}$ corresponding to particular $\mathcal{T}$ has the structure

$$\hat{H}_{\text{eff}}^{(ij)}(\mathcal{T}) = \hat{H}_{\text{tun}}^{(k_{N+1}k_{N+1}+1)} \hat{\mathcal{G}} \hat{H}_{\text{tun}}^{(k_N k_N+1)} \hat{\mathcal{G}} \ldots \hat{\mathcal{G}} \hat{H}_{\text{tun}}^{(k_1 k_1+1)},$$

where the many-particle Green's function $\hat{\mathcal{G}} = [\hat{H}_0 + \hat{H}_C]^{-1}$. The function $\lambda_k(\mathcal{T}) = 1$ if, in the ordering $\mathcal{T}$, the grain $k-1$ comes earlier than the grain k, and $\lambda_k(\mathcal{T}) = -1$ otherwise. The sign factor $(-1)^{K(\mathcal{T})}$ arises due to permutations of fermionic operators. The Fermi functions $f_F(\epsilon)$ take into account the Fermi filling factors. The δ function ensures the energy conservation, and $\Delta_{ij} = \varepsilon_j - \varepsilon_i - E_c^{(ij)}$ is the difference of the energies of the initial and the final state. The factors

$$Q(\mathcal{T}) = \prod_{r=1}^{N} \left[H_C\{n(r)\} + \sum_{r'=1}^{r} (\epsilon_{h_{k_{r'}+1}} - \epsilon_{p_{k_{r'}}}) \right]^{-1} \quad (4)$$

are products of energy denominators appearing in $\hat{\mathcal{G}}$. Here, n_k are the numbers of excess electrons on the kth grain after p local hops; they can be found from the following recursion formula:

$$n_k(r) = \begin{cases} n_k(r-1) - 1, & \text{if } k = k_r, \\ n_k(r-1) + 1, & \text{if } k = k_r + 1, \\ n_k(r-1), & \text{otherwise,} \end{cases} \quad (5)$$

while $n_k(0) = n_k^{(0)}$ is the equilibrium distribution.

Inspecting expression (3), we see that the characteristic value $\bar{\epsilon}_{\text{inel}}$ of the inelastic energies ϵ_{pl}, ϵ_{hl} is controlled by the combination of the δ function in (3) and the product of the corresponding Fermi functions. As a result, $\bar{\epsilon}_{\text{inel}} \sim \Delta_{ij}/\bar{L}$, where $\bar{L}$ (which is T dependent) is the number of inelastic cotunneling events in the total process. Actually $T \ll \bar{\epsilon}_{\text{inel}} \ll E_C$; consequently, in particular, the dependence of $Q(\mathcal{T})$ on the inelastic energies can be neglected. On the other hand, the characteristic value of $\bar{\epsilon}_{\text{el}}$ of the elastic energies $\epsilon_{\alpha m}$ is limited only by the energy denominators $Q(\mathcal{T})$, so that $\bar{\epsilon}_{\text{el}} \sim E_C$.

Thus, performing the integration over ϵ_{pl}, ϵ_{hl} and $\epsilon_{\alpha m}$, we obtain for the effective Miller–Abrahams dimensionless conductance g_{ij} between two distant grains i and j the following:

$$g_{ij} \propto e^{-\frac{\varepsilon_{ij}}{T}} \left(\frac{t}{E_C}\right)^{2N} \sum_{L=0}^{N} \frac{\left(\frac{2|\Delta_{ij}|^2}{\delta^2}\right)^L \left(\frac{E_C}{\delta}\right)^{N-L}}{(2L+1)!} F_{NL}. \quad (6)$$

Here $\delta = E_0 e^{-\overline{\ln(E_0 \nu v)}}$ is the mean level spacing (ν is the electronic density of states per one spin projection at the Fermi level in a particular grain, v is the volume of the grains, and E_0 is an arbitrary energy unit). The characteristic Coulomb energy $E_C = E_0 e^{-\overline{\ln(E_{kk}/E_0)}}$ (normally $E_C \sim e^2/\kappa_{\text{eff}} a$, where a is the average diameter of the grains, and κ_{eff} is the effective dielectric permeability of the material; see [6]). Finally, the mean tunneling amplitude $t = E_0 e^{1/2\overline{\ln(|t_{kk+1}|^2/E_0^2)}}$, where $|t_{kk+1}|^2$ is the coarse grained (i.e., averaged over an interval of ener-

gies near the Fermi level; large compared to the level spacing but small compared to any other relevant scale) value of $|t_{\alpha_k, \alpha'_{k+1}}|^2$. The averaging of the logarithm rule appearing in the above definitions of mean values arises as a result of self-averaging of a large ($\sim N$) number of similar independent random factors with identical distributions. Note also the presence of the spin-factors 2 in the multipliers corresponding to inelastic processes and the absence of such factors for the elastic processes.

The local activation energy ε_{ij} for the ij hop is the combination of ε_i, ε_j and $E_c^{(ij)}$, which is standard for the hopping conductivity theory (see [5] for the explicit definition).

The weight function $F_{NL} = \sum_{\mathcal{P}} \delta_{L, L(\mathcal{P})} C(\mathcal{P})$, where $C(\mathcal{P})$ are numerical coefficients depending only on the partition $\mathcal{P}$ and on the explicit form of the charging energy matrix $E_c^{(kk')}$:

$$C(\mathcal{P}) = \sum_{\mathcal{T}, \mathcal{T}'} (-1)^{K(\mathcal{T}) - K(\mathcal{T}')} \times \int \prod_m d\tilde{\epsilon}_m \delta_{\lambda_m(\mathcal{T})\lambda_m(\mathcal{T}')} \theta[-\lambda_m(\mathcal{T})\tilde{\epsilon}_{\alpha_m}] \tilde{Q}(\mathcal{T})\tilde{Q}(\mathcal{T}'), \quad (7)$$

$\tilde{\epsilon}_m \equiv \epsilon_m/E_C$ and $\tilde{Q}(\mathcal{T}) \equiv Q(\mathcal{T})E_C^N$ being the dimensionless variables.

The explicit form of the weight function $F_{N,L}$ for general $E_c^{(kk')}$ can not be found. However, as it is argued below, the asymptotics of F relevant for the purely elastic and purely inelastic limits are $F_{N,0} \approx \tilde{A}_1^N$ and $F_{N,N} \approx \tilde{A}_2^N$, correspondingly. The numerical constants $\tilde{A}_1$ and $\tilde{A}_2$ are not known. As a result,

$$g_{ij} \propto \exp\left\{-\frac{\varepsilon_{ij}}{T}\right\} \begin{cases} \left(\dfrac{\tilde{A}_1 g\delta}{8\pi^2 E_C}\right)^{N_{ij}}, & \text{elastic}, \\ \left(\dfrac{e^2\tilde{A}_2 g|\Delta_{ij}|^2}{16\pi^2 N_{ij}^2 E_C^2}\right)^{N_{ij}}, & \text{inelastic}, \end{cases} \quad (8)$$

where $g \equiv Gh/e^2 = 8\pi^2(t/\delta)^2 \ll 1$ is the average dimensionless conductance of a contact between two adjacent grains. Note that this definition of g differs from that in [8, 9]. Applying standard Mott–Efros–Shklovskii arguments to the random network with conductances (8), we obtain Eq. (1) with $T_{ES} = \mathcal{L}(T)E_C$

$$\mathcal{L}(T) = \begin{cases} c_1 \ln\left(\dfrac{8\pi^2 E_C}{\tilde{A}_1 g\delta}\right), & T \ll T_c, \\ c_1 \ln\left(\dfrac{16\pi^2 E_C^2}{e^2\tilde{A}_2 g T^2 \mathcal{L}^2}\right), & T \gg T_c, \end{cases} \quad (9)$$

where the crossover temperature $T_c \sim \sqrt{E_C\delta}/\mathcal{L}$, and $c_1 \sim 1$ is an unknown constant depending on the statistical geometry of the granular material. Since $E_C \propto a^{-1}$ and $\delta \propto a^{-3}$, we conclude that roughly $T_{ES} \propto a^{-1}$ and $T_c \propto a^{-2}$.

It should be noted that the above consideration is justified and the VRH regime is actual only if the characteristic length of the hop is large: $\bar{N} \sim (E_C/\mathcal{L}T)^{1/2} \gg 1$. For $\bar{N} < 1$, the nearest neighbor hopping regime characterized by the Arrhenius law $\sigma \propto \exp(-E_A/T)$ with the activation energy $E_A \sim E_C$ should be observed. The crossover temperature between the two regimes is controlled by the intergrain conductance g; the NNH is likely to be found in the samples with very low g.

MODEL OF LOCAL REPULSION: MOTT LAW FOR GRANULAR ARRAY

The expression (7) can be explicitly evaluated for the model case of the short range Coulomb interaction $E_c^{(kk')} = E_k\delta_{kk'}$. Then, the dimensionless local energies of the charged states are $\tilde{E}_k^{(\pm)} = (E_k/E_C)[1/2 \mp q_k]$, and $\varepsilon_i = E_k\left(\frac{1}{2} - |q_i|\right)\mathrm{sgn}(q_i)$. In this case, (7) can be written as a product of single particle Green functions with energies depending on the local charge. As a result,

$$C(\mathcal{P}) = \prod_m \left(\frac{1}{\tilde{E}_m^{(+)}} + \frac{1}{\tilde{E}_m^{(-)}}\right) \prod_l \left(\frac{1}{\tilde{E}_l^{(+)}} - \frac{1}{\tilde{E}_l^{(-)}}\right)^2,$$

so that, for $N \gg 1$, when the number of similar factors in (10) is large and an effective self-averaging takes place,

$$F_{NL} = C_N^L A_1^{N-L} A_2^L, \quad (10)$$

$$A_1 \equiv e^{-\overline{\ln(1/4 - q^2)}}, \quad A_2 \equiv 4e^{\overline{\ln q^2} - 2\overline{\ln(1/4 - q^2)}}, \quad (11)$$

C_N^L being binomial coefficients. The constant A_1 does not show any dramatic dependence on the strength of the random potentials: $A_1 = e^2 \approx 7.4$ for strong charge disorder, and $A_1 = 4$ for a weak one. The constant $A_2 = e^2$ for a strong disorder, while, for a weak one,

$A_1 \sim q_0^2 \ll 1$. The reason is the destructive interference between the two possible processes of the pair production: in the *e–h* process, the electron is created first and the hole is created second, while, in the *h–e*-process, the order is inverted. As a result, for $q_0 \ll 1$, the crossover temperature strongly depends on q_0: $T_c(q_0) \sim (q_0\mathcal{L})^{-1}\sqrt{E_C\delta}$. The growth of T_c is saturated at $T_c^{\max} \sim (\mathcal{L})^{-1}(E_C^3\delta)^{1/4}$ for $q_0 \lesssim (\delta/E_C)^{1/4}$ when the energies ϵ_{pl}, ϵ_{hl} of the pairs come into play. Thus, we conclude that, for the case of weak charge disorder, the inelastic cotunneling is suppressed and the crossover between the elastic and inelastic cotunneling is shifted to higher temperatures.

Unfortunately, the result (10) can not be generalized for the case of nonlocal interaction $E_c^{(ij)}$. It can be shown, however, that $F_{N,0} \approx \tilde{A}_1^N$, and $F_{N,N} \approx \tilde{A}_2^N$ with certain renormalized constants $\tilde{A}_1$ and $\tilde{A}_2$. Roughly, the reason is as follows (the details will be presented elsewhere): the simple exponential form of the F function holds for any effectively short-range interaction (not necessarily a strictly local one), while, for an effectively long-range one, the functional form of F can be changed dramatically. The clue is that, despite the long-range character of the Coulomb potential, the interaction of effective degrees of freedom, in our case, is the short-range one. Indeed, the actual charge configurations relevant to our problem are those generated by local electronic hops between neighboring grains. These hops create local dipoles, and the dipole–dipole interaction decays with distance r as r^{-3}.

With the explicit formula (10) at hand, one can perform the summation in (6) and find

$$\ln g_{ij} = N_{ij}\left\{\ln\left(\frac{A_1 g\delta}{8\pi^2 E_C}\right) + \varphi\left(\frac{|\varepsilon_i - \varepsilon_j|}{2N_{ij}}\sqrt{\frac{2A_2}{A_1 E_C\delta}}\right)\right\} - \frac{\varepsilon_{ij}}{T},$$

where the function $\varphi(z)$ is implicitly defined by the relations $\varphi(z) = 2y - \ln(1-y)$, $y^3 = (1-y)z^2$. The function $y(z) \equiv \bar{L}/N$ (with the asymptotics $y(z) \approx z^{2/3}$ at $z \ll 1$) has the meaning of a relative fraction of inelastic events.

The average number of grains N_{ij} in a string connecting two distant grains is proportional to the distance r_{ij} between them: $N_{ij} = c_2 n_g^{1/d} r_{ij}$, where n_g is the concentration of grains, and $c_2 \sim 1$ is a geometric constant depending only on the statistics of the grain packing. The estimates made for c_2 for several two-dimensional models show that $c_2 \approx 1$. Thus, we have arrived at the $d+1$ dimensional percolation problem in the $\mathbf{r}_i$ and ε_i space. The density of sites $\nu_{d+1} = n_g P_{1/2}/E_C$ in this space is the density of marginal grains whose ground states are almost degenerate. The connectivity criterion reads

$$\xi(\mathbf{r}_i, \varepsilon_i|\mathbf{r}_j, \varepsilon_j) < \xi, \quad \text{where}$$

$$\xi(\mathbf{r}_i, \varepsilon_i|\mathbf{r}_j, \varepsilon_j) = \frac{\varepsilon_{ij}}{T} + c_2 n_g^{1/d} \times r_{ij}\left\{\ln\left(\frac{8\pi^2 E_C}{A_1 g\delta}\right) - \varphi\left(\frac{|\varepsilon_i - \varepsilon_j|}{2c_2 n_g^{1/d} r_{ij}}\sqrt{\frac{2A_2}{A_1 E_C\delta}}\right)\right\}. \quad (12)$$

As usual (see [5]), one should find a value $\xi = \xi_c$ corresponding to the first appearance of an infinite cluster of grains connected according to the criterion (12). Then, with the exponential accuracy, the global conductivity of the system $\sigma \propto \exp(-\xi_c)$.

The arising percolational model differs, however, from the standard VRH one (see [5, 16]) due to an additional dependence on r_{ij} and ε_i, ε_j appearing in the argument of the function φ. However, since the variation of this function on the relevant scale of it's argument is $\delta\varphi \sim 1 \ll \mathcal{L}$, the corresponding relative variation of $\xi(\mathbf{r}_i, \varepsilon_i|\mathbf{r}_j, \varepsilon_j)$ is small and can be treated by the standard perturbational method (see [5]). As a result, we obtain the Mott law

$$\sigma \sim \exp\{-(T_M/T)^{1/(d+1)}\}, \quad (13)$$

with T_M, which is slightly temperature-dependent:

$$T_M = \frac{\mathcal{L}^d(T/T_c)n_c}{2P_{1/2}}E_C, \quad T_c = \frac{2c_2}{\mathcal{L}}\sqrt{\frac{A_1 E_C\delta}{2A_2}}, \quad (14)$$

$$\mathcal{L}(T/T_c) = c_2\left\{\ln\left(\frac{8\pi^2 E_C}{A_1 g\delta}\right) - \chi(T/T_c)\right\}. \quad (15)$$

The universal percolation constant $n_c \approx 5.7$ for $d = 3$ and $n_c \approx 3.5$ for $d = 2$. The function $\chi(z)$ is related to $\varphi(z)$ by

$$\chi(z) = \langle s\rangle_{\text{perc}}^{-1}\left\langle s\varphi\left(\frac{|\zeta - \zeta'|}{s}z\right)\right\rangle_{\text{perc}}, \quad (16)$$

where the averaging over the percolation hypersurface in the space of the dimensionless energy ζ and dimensionless coordinate s has the following explicit meaning:

$$\langle F\rangle_{\text{perc}} \equiv \frac{\int d\zeta d\zeta' \int d\mathbf{s} F(\zeta, \zeta', s)\delta\left(1 - s - \frac{|\zeta| + |\zeta'| + |\zeta - \zeta'|}{2}\right)}{\int d\zeta d\zeta' \int d\mathbf{s}\,\delta\left(1 - s - \frac{|\zeta| + |\zeta'| + |\zeta - \zeta'|}{2}\right)}.$$

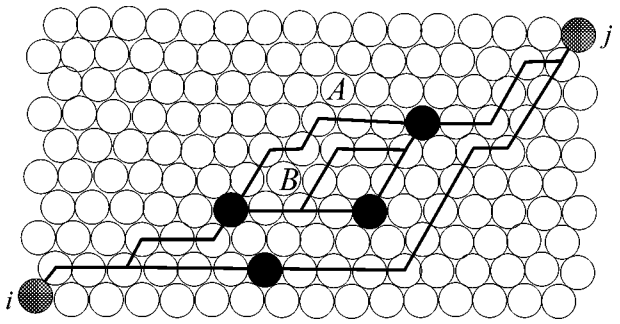

Four different strings contributing to the $i \longrightarrow j$ transition in a particular realization of an array. For the partition shown (the inelastic grains $\{l\}$ are depicted as filled circles and the elastic grains $\{m\}$ as open ones), only two strings (A and B) contribute to the interference effects.

The asymptotics of the function $\chi(z)$ are

$$\chi(z) \approx \begin{cases} b_1 z^{2/3} & \text{for } z \ll 1, \\ 2(\ln z + b_2 + \ldots) & \text{for } z \gg 1, \end{cases} \quad (17)$$

where b_1, b_2 are universal constants depending only on the space dimensionality d. In particular, $b_2 = -1/6$ for $d = 2$ and $b_2 = -1/2$ for $d = 3$.

Experimentally, the Mott law (13) is likely to be observed in materials with weak charge disorder, where the density of states at $\varepsilon = 0$ is very small because of the factor $P_{1/2} \ll 1$, and the Coulomb gap is irrelevant, except for extremely low T range. In such materials, however, T_M is very large (cf. (14)) and the crossover between the Mott and the Arrhenius laws should take place at relatively low T.

MAGNETORESISTANCE

In the entire above consideration, we have neglected the possible interference between contributions of different strings (if any) connecting the same pair ij. The main reason for this approximation is the strong sign fluctuations of the matrix elements $t_{h_h p_{h-1}}$: even in the coherent (purely elastic) limit, the signs of the contributions of different strings to the composite amplitude of the $i \longrightarrow j$ transition fluctuate independently. The interference effects, although irrelevant to the zero-field effects, are sensitive to a magnetic field; as a result, they may be the source for a low temperature effect of a negative orbital magnetoresistance similar to the one discussed in [10–13] for the case of VRH in conventional disordered semiconductors. The key component of this effect is the interference between the contributions of different spatial paths leading from i to j. In our case, this means the existence of several strings $i \longrightarrow j$ giving comparable contributions to g_{ij}. For a fairly homogeneous material, where all g_{kk+1} are of the same order of magnitude, one can expect such different strings to exist already for $N_{ij} \gtrsim 1$. For a strongly disordered material (with exponentially large fluctuations of g_{kk+1}), there is typically only one leading string for $N_{ij} < N_{\min}$, and only for $N_{ij} > N_{\min}$ do several strings act in parallel. The crossover length $N_{\min}$ is a function of the magnitude of the fluctuations $D = \overline{(\ln g - \overline{\ln g})^2}$; the explicit form of this function is model-dependent, and we will not discuss it in the present letter. For us, it is only important that $N_{\min}(D) \sim 1$ for $D \sim 1$, and $N_{\min}(D) \gg 1$ for $D \gg 1$.

Apparently, the magnetoresistance is controlled by the typical area $S(N_{\text{loop}})$ of the interference loop (N_{loop} being the length of this loop). Loops with $N_{\text{loop}} < N_{\min}$ are extremely rare and can be ignored. For $N_{\text{loop}} > N_{\min}$, the scaling law $S(N_{\text{loop}}) \sim N_{\text{loop}}^u$ with an unknown exponent $u < 2$ holds. The problem of the statistics of loops is closely related to the well-studied theory of directed polymers in a random field [17].

One of the essential ingredients of our cotunneling process is the presence of inelastic events, which certainly destroy the interference and suppress the magnetoresistance. Namely, the interference between two different strings A and B is possible only if the cotunneling at all grains of A and B that are not common for them is elastic (see figure). Since the relative fraction of inelastic cotunnelings y depends on the temperature, so does the length $M_{\text{el}} \sim 1/y$ of a typical stretch on a string containing only elastic grains. It is just M_{el}, not the entire length N of the distant hop, that should play the role of the effective length N_{loop} of the interference loop. Clearly, for $T \gtrsim T_c$, one has $M_{\text{el}} \sim 1$, while $M_{\text{el}} \sim (T_c/T)^{2/3} \gg 1$ for $T \ll T_c$.

Thus, we can conclude that, for temperatures $T > T_{\text{mag}} \sim T_c N_{\min}^{-3/2}(D) < T_c$, the orbital magnetoresistance is strongly suppressed (since the typical elastic stretch is shorter than $N_{\min}$), while, at $T \ll T_{\text{mag}}$, it can be relatively strong: the characteristic magnetic field H_c at which the conductivity would saturate at $\sigma(H \gg H_c) \sim \sqrt{2}\,\sigma(H = 0)$ (cf. [12]) is

$$H_c \sim \Phi_0 / S(M_{\text{el}}) \sim H_c^{(0)} (T/T_c)^{2u/3}, \quad (18)$$

where $H_c^{(0)} = \Phi_0 n_g^{2/d}$ is the field corresponding to a flux Φ_0 through an elementary triangle of neighboring grains. The dependence $\sigma(H)$ at $H < H_c$ can be different in different ranges of H: either $\Delta\sigma \propto H^2$ (at the smallest fields, see [11, 13]) or $\Delta\sigma \propto H$ (at the intermediate fields, see [10, 13]) or $\Delta\sigma \propto H^{1/2}$ (at relatively high fields, see [12]).

CONCLUSIONS

In conclusion, we have developed a theory of variable-range hopping in granular arrays with poor inter-

grain coupling. Long-range hopping of electrons is provided by the multiple cotunneling strings that contain both elastic and inelastic processes within individual grains. In the presence of long-range Coulomb interaction, the Efros–Shklovskii law for the temperature dependence of conductivity is derived in the asymptotic limits of purely inelastic or purely elastic cotunneling. Upon temperature decrease, the relative contribution of elastic cotunneling increases; for the model case of local (screened) Coulomb interaction, the general situation of partially elastic cotunneling was studied and the crossover temperature T_c was determined; cf. Eqs. (9), (14). For real granular metals, this crossover temperature happens to be rather low. In particular, for Al grains of size $a \sim 20$ nm, one estimates $E_C \sim 500$ K and $\delta \sim 0.05$ K, which leads (at $g \sim 0.3$, consequently, $\mathcal{L} \sim 12$) to $T_c \sim 0.5$ K. For $a \sim 10$ nm, the same estimates give $T_c \sim 2$K. Therefore, the major part of the experimental temperature range (from room to liquid helium temperatures) is dominated by inelastic cotunneling. This is the reason why the magnetoresistance is very weak in granular metals, contrary to disordered semiconductors. The observation of noticeable negative magnetoresistance due to interference of different tunneling strings might be possible with granular media made of small (≤10 nm) grains of nonsuperconductive metals such as copper, silver, or gold at temperatures below 1 K. In the inelastic regime (at $T > T_c$), the constant T_{ES} entering Eq. (1) is itself T dependent: it logarithmically increases with the decrease of T. This dependence should lead to somewhat faster growth of the resistivity upon lowering T than that predicted by the standard Efros–Shklovskii law.

After the present study was completed, we became aware of a preprint [18] where purely elastic variable-range cotunneling was proposed as the conduction mechanism for granular metals; their results seem to agree with ours as long as inelastic processes are neglected.

We are grateful to A.L. Efros, T. Grenet, L.B. Ioffe, and Z. Ovadyahu for many useful discussions. This research was supported by the program "Quantum Macrophysics" of the Russian Academy of Sciences and by the Russian Foundation for Basic Research (project nos. 04-02-16348 and 04-02-08159).

REFERENCES

1. T. Chui *et al.*, Phys. Rev. B **23**, 6172 (1981).
2. R. W. Simon *et al.*, Phys. Rev. B **36**, 1962 (1987).
3. A. Gerber, A. Milner, G. Deutscher, *et al.*, Phys. Rev. Lett. **78**, 4277 (1997).
4. A. L. Efros and B. I. Shklovskii, J. Phys. C **8**, L49 (1975).
5. B. I. Shklovskiĭ and A. L. Éfros, *Electronic Properties of Doped Semiconductors* (Nauka, Moscow, 1979; Springer, New York, 1984).
6. J. Zhang and B. I. Shklovskii, Phys. Rev. B **70**, 115317 (2004).
7. D. A. Averin and Yu. V. Nazarov, Phys. Rev. Lett. **65**, 2446 (1990).
8. K. B. Efetov and A. Tschersich, Europhys. Lett. **59**, 114 (2002); Phys. Rev. B **67**, 174205 (2003).
9. M. V. Feigel'man, A. S. Ioselevich, and M. A. Skvortsov, Phys. Rev. Lett. **93**, 136403 (2004).
10. V. L. Nguen, B. Z. Spivak, and B. I. Shklovskii, JETP Lett. **41**, 42 (1985).
11. U. Sivan, O. Entin-Wohlman, and Y. Imry, Phys. Rev. Lett. **60**, 1566 (1988).
12. H. L. Zhao, B. Z. Spivak, M. P. Celfand, and S. Feng, Phys. Rev. B **44**, 10760 (1991).
13. B. I. Shklovskii and B. Z. Spivak, in *Hopping Transport in Solids*, Ed. by M. Pollak and B. Shklovskii (Elsevier, Amsterdam, 1991), p. 271.
14. L. I. Glazman and M. Pustilnik, cond-mat/0501007.
15. D. V. Averin and K. K. Likharev, in *Mesoscopic Phenomena in Solids*, Ed. by B. L. Altshuler, P. A. Lee, and R. A. Webb (Elsevier, Amsterdam, 1991).
16. V. Ambegokar, B. I. Halperin, and J. S. Langer, Phys. Rev. B **4**, 2612 (1971).
17. T. Hwa and D. S. Fisher, Phys. Rev. B **49**, 3136 (1994), and references therein.
18. I. S. Beloborodov, A. V. Lopatin, V. M. Vinokur, and V. I. Kozub, cond-mat/0501094.

JETP Letters, Vol. 81, No. 6, 2005, pp. 284–286. Translated from Pis'ma v Zhurnal Éksperimental'noĭ i Teoreticheskoĭ Fiziki, Vol. 81, No. 6, 2005, pp. 348–350.

Oscillations of the Magnetoresistance of a Two-Dimensional Electron Gas in a GaAs Quantum Well with AlAs/GaAs Superlattice Barriers in a Microwave Field

A. A. Bykov, A. K. Bakarov, A. K. Kalagin, and A. I. Toropov

Institute of Semiconductor Physics, Siberian Division, Russian Academy of Sciences, Novosibirsk, 630090 Russia
e-mail: bykov@thermo.isp.nsc.ru

Received February 24, 2005

The effect of microwave radiation in the frequency range from 1.2 to 10 GHz on the magnetoresistance of a high-mobility two-dimensional electron gas has been studied in a GaAs quantum well with AlAs/GaAs superlattice barriers. It has been found that the microwave field induces oscillations of this magnetoresistance, which are periodic in the reciprocal magnetic field (1/*B*). It has been shown that the period of these oscillations in the frequency range under study depends on the microwave radiation power. © *2005 Pleiades Publishing, Inc.*

PACS numbers: 73.23.–b, 73.40.Gk

Magnetoresistance (MR) oscillations that have recently been discovered in a high-mobility two-dimensional electron gas (2DEG) in a GaAs/AlGaAs heterojunction are induced by microwave radiation in the magnetic field region preceding the region of the appearance of the Shubnikov–de Haas (SdH) oscillations [1]. It was found that the positions of oscillation peaks on the magnetic field scale are determined by the ratio $\omega/\omega_c = N$, where $\omega/2\pi$ is the microwave frequency; ω_c is the cyclotron frequency of electrons in a magnetic field B; and $N = 1, 2, 3, \ldots$. These oscillations were predicted theoretically more than 30 years ago [2] and were observed experimentally due mainly to advances in preparing high-quality semiconducting structures with modulated doping.

Soon after the publication of [1], it was shown that, in a magnetic field range preceding the region of SdH oscillations, MR oscillations are also induced by a constant driving current I_{dc} [3], i.e., by a zero-frequency electric field. These oscillations are associated with tunneling of charge carriers between the Landau levels tilted under the action of the electric field. The period of these oscillations depends on the ratio I_{dc}/B, while the positions of the oscillation peaks that are associated with microwave radiation are determined by the frequency, but they are independent of the power [4].

Obviously, with decreasing the microwave field frequency, the oscillations that are caused by vertical transitions between the Landau levels [5] must change to oscillations associated with "horizontal" tunneling [3]. In other words, below a certain characteristic frequency, the positions of the oscillation peaks on the magnetic field scale must depend on the microwave radiation power. It follows from general considerations that this boundary frequency must be a function of the mobility of 2DEG and the quantity kT, where k is the Boltzmann constant and T is the temperature.

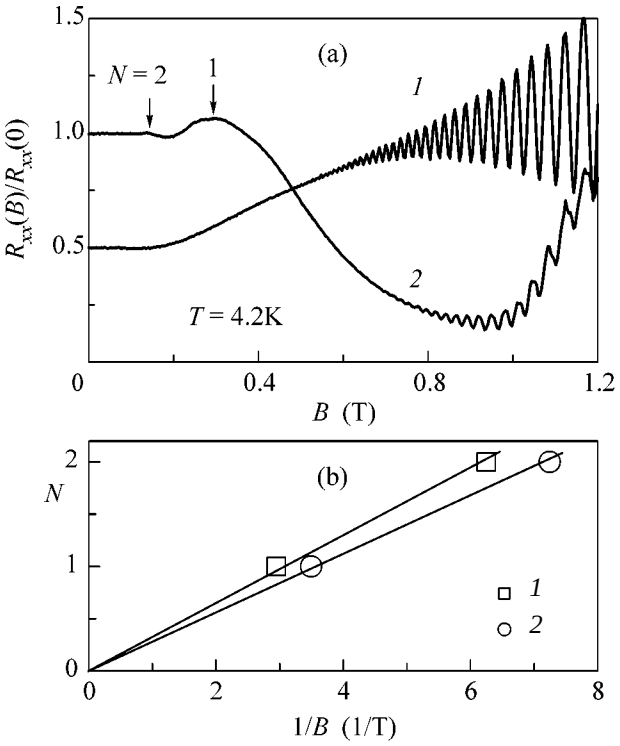

Fig. 1. (a) Magnetic field dependence of relative MR at T = 4.2 K for I_{dc} = (*1*) 0 and (*2*) 1.2×10^{-4} A. The digits on curve *2* show the numbers (N) of oscillation peaks. For better visualization, curve *1* is displaced downwards along the y axis. (b) The positions of oscillation peaks vs. 1/B for I_{dc} = (*1*) 1.4×10^{-4} and (*2*) 1.2×10^{-4} A.

0021-3640/05/8106-0284$26.00

Here, we study the effect of microwave radiation on the MR of a high-mobility 2DEG in a GaAs quantum well with AlAs/GaAs superlattice barriers. In such selectively doped structures, we observed MR oscillations induced by microwave radiation in the range of classically strong magnetic fields. We proved experimentally that the positions of the peaks of these oscillations in a magnetic field in the microwave radiation range under study depend on the power of the microwave field.

The structures under study were grown by molecular beam epitaxy (MBE) on (100) GaAs substrates. The width of the GaAs quantum well was 13 nm. AlAs/GaAs type-II superlattices served as the barriers, which made it possible to obtain a high-mobility 2DEG with a high concentration [6, 7]. The mobility of 2DEG in the MBE structure at the liquid helium temperature and a concentration of 1.3×10^{12} cm^{-2} was 10^6 cm^2/V s. Measurements were carried out at $T = 4.2$ K in magnetic fields up to 2 T on 50-μm-wide Hall bridges with distances of 100, 200, 300, and 400 μm between the potentiometer leads. Microwave radiation was supplied to the sample through a coaxial cable and was fed to the 2DEG through current contacts of the Hall bridge. The resistance was measured using a 10^{-6}-A alternating current with a frequency of 777 Hz.

Figure 1a shows the dependences of the relative MR for (curve *1*) zero dc I_{dc} and (curve *2*) a nonzero dc. It is clearly seen that, as compared to curve *1*, the direct current reduces the amplitude of the SdH oscillations in fields exceeding 0.5 T, while oscillating MR appears in the field range below 0.5 T. Analysis of the curves shows that MR oscillations induced by current I_{dc} are periodic in the reciprocal magnetic field to within experimental error. Figure 1b shows that the positions of the peaks of these oscillations depend on I_{dc}, which is completely consistent with the results obtained in [3]. The position of the brightest peak on curve *1* (Fig. 1a) corresponds to the integer $N = 1$, which also agrees with the results obtained in [3].

Figure 2 shows the relative MR curves for various powers P of 1.2-GHz microwave radiation. It is seen that oscillations whose position on the magnetic field scale depends on power P are induced by microwave radiation in the region preceding the SdH oscillations. The analysis of the positions of the peaks of these oscillations in a magnetic field is presented in Fig. 3 for various values of P and frequencies of 1.2 and 10 GHz. Analogously to oscillations induced by I_{dc}, these oscillations are periodic in $1/B$, which is consistent with the results obtained in [1], but the position of the first peak on the magnetic field scale corresponds to the integer $N = 3$ rather than to $N = 1$.

The experimental data that are presented in Fig. 3 show that the behaviors observed at frequencies of 1.2 and 10 GHz are qualitatively similar to each other. This means that the dependence of the magnetic field positions of the peaks on the frequency of the microwave

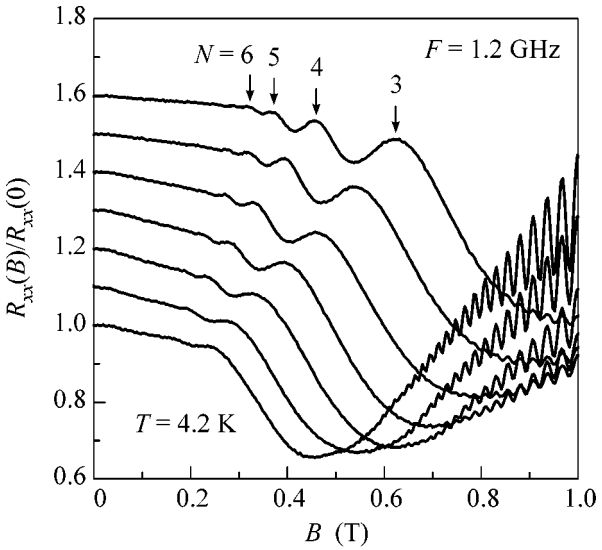

Fig. 2. Magnetic field dependence of the relative MR at $T = 4.2$ K for the microwave field frequency $F = 1.2$ GHz for various powers P. The lower and upper curves correspond to the minimum and maximum P values, respectively. For better visualization, the curves, beginning with the lower one, are displaced upwards along the y axis. Numbers N denoted oscillation peaks.

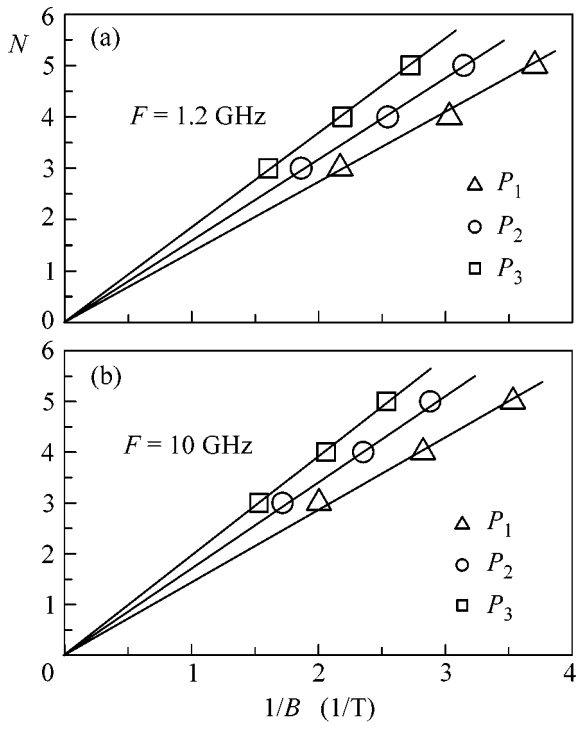

Fig. 3. Positions of the oscillation peaks vs. $1/B$ for various powers P ($P_1 > P_2 > P_3$) and for frequencies F = (a) 1.2 and (b) 10 GHz.

field begins at higher frequencies at $T = 4.2$ K. It was shown in [4] that a noticeable frequency dependence of the positions of oscillation peaks for samples with a higher mobility and a substantially lower concentration of the 2DEG begins above 7.5 GHz at a temperature of 280 mK. Our results can be explained qualitatively by the fact that the MR oscillations in the 2DEG in the samples studied at $T = 4.2$ K in a frequency range up to 10 GHz are due to tunneling between the Landau levels tilted in the electric field [3].

Thus, we observed experimentally the MR oscillations of a 2DEG that are induced in a GaAs quantum well with AlAs/GaAs superlattice barriers by microwave radiation. Their period in the reciprocal magnetic field has been shown to depend on the microwave power in a frequency range up to 10 GHz.

We are grateful to M.V. Entin for fruitful discussions of the results. This work was supported by the Russian Foundation for Basic Research (project no. 04-02-16789) and INTAS (grant no. 03-51-6453).

REFERENCES

1. M. A. Zudov *et al.*, Phys. Rev. B **64**, 201 311(R) (2001).
2. V. I. Ryzhii, Sov. Phys. Solid State **11**, 2078 (1970).
3. C. L. Yang *et al.*, Phys. Rev. Lett. **89**, 076801 (2002).
4. R. L. Willett *et al.*, Phys. Rev. Lett. **93**, 026804 (2004).
5. V. Rizhii, A. Chaplik, and R. Suris, Pis'ma Zh. Éksp. Teor. Fiz. **80**, 412 (2004) [JETP Lett. **80**, 363 (2004)].
6. K.-J. Friedland *et al.*, Phys. Rev. Lett. **77**, 4616 (1996).
7. A. A. Bykov, A. K. Bakarov, L. V. Litvin, and A. I. Toropov, Pis'ma Zh. Éksp. Teor. Fiz. **72**, 300 (2000) [JETP Lett. **72**, 209 (2000)].

Translated by N. Wadhwa

JETP Letters, Vol. 81, No. 6, 2005, pp. 287–291. From Pis'ma v Zhurnal Éksperimental'noĭ i Teoreticheskoĭ Fiziki, Vol. 81, No. 6, 2005, pp. 351–355.

Spin Fluctuations in the Stacked-Triangular Antiferromagnet $YMnO_3$¶

B. Roessli[1], S. N. Gvasaliya[1, 2], E. Pomjakushina[1, 3], and K. Conder[3]

[1] *Laboratory for Neutron Scattering ETHZ and Paul Scherrer Institute, CH-5232 Villigen PSI, Switzerland*

[2] *Ioffe Physical Technical Institute, St. Petersburg, 194021 Russia*

[3] *Laboratory for Development and Methods, Paul Scherrer Institute, CH-5232 Villigen PSI, Switzerland*

Received February 24, 2005

The spectrum of spin fluctuations in the stacked-triangular antiferromagnet $YMnO_3$ was studied above the Néel temperature using both unpolarized and polarized inelastic neutron scattering. We find an in-plane and an out-of-plane excitation. The in-plane mode has two components just above T_N: a resolution-limited central peak and a Debye-like contribution. The quasi-elastic fluctuations have a line width that increases with q as Dq^z and the dynamical exponent $z = 2.3$. The out-of-plane fluctuations have a gap at the magnetic zone center and do not show any appreciable q dependence at small wave vectors. © *2005 Pleiades Publishing, Inc.*

PACS numbers: 75.40.–s, 78.70.Nx

1. INTRODUCTION

$YMnO_3$ belongs to the family of $RMnO_3$ (R = Rare-earth) manganite ferroelectric compounds that crystallize in the hexagonal space group $P6_3cm$ below the paraelectric–ferroelectric phase transition (~900 K). In $YMnO_3$, the Mn^{3+} ions form triangular layers well separated from each other by *Y* layers. Because, in the ferroelectric phase, the lattice is distorted, the Mn ions are slightly trimerized. The large separation between adjacent layers suggests that $YMnO_3$ forms a good candidate for a geometrically frustrated 2-Dimensional (2D) antiferromagnet.

The magnetic structure of hexagonal $YMnO_3$ was first investigated by Bertaut and Mercier [1] and reinvestigated later in more details by Munoz *et al.* [2]. Below $T_N \sim 70$ K, the $S = 2$ magnetic moment of Mn ions are arranged in a 120° magnetic structure with the triangular layers at $z = 0$ and $z = 1/2$ being antiferromagnetically coupled. At saturation, the magnetic moment is $\mu = 2.9\mu_B$; i.e., it is significantly reduced from the expected $4\mu_B$ of Mn^{3+} spins, which was taken as evidence that, even in the ordered phase, strong spin fluctuations are present as a consequence of geometrical frustration [3]. Analysis of the spin-wave spectrum has confirmed the 2D character of the magnetic exchange interactions in $YMnO_3$ [4] with the ratio of the intra- to interplane exchange interactions being on the order $\sim 2 \times 10^2$. Whereas well-defined excitations are observed below the ordering temperature, a broad inelastic signal, as well as short-range correlations between the Mn magnetic moments within the triangular layers, persists well above T_N [3].

In this work, we investigate the q and temperature dependence of the spin excitations in $YMnO_3$ close to the Néel temperature. We were motivated by the fact that the nature of the phase transition of frustrated magnets is still not completely understood and that the critical properties of stacked triangular antiferromagnets have received special attention since Kawamura [5] proposed that the critical exponents in these systems form a new universality class. Experimental confirmation of the new class of (chiral) exponents was found in $CsMnBr_3$ by unpolarized [6] and polarized neutron scattering [7] measurements as well as in Ho [8]. Second, an anomaly in the dielectric constant ε with the electric field applied in the *ab* plane was found in $YMnO_3$ [9] at T_N. The nature of the coupling between the electric and magnetic properties in hexagonal manganites is a subject of intense debate [10]. Clearly, it is required to characterise the behavior of the magnetic fluctuations in the vicinity of T_N to understand the possible relationship with the magneto-dielectric effect in $YMnO_3$ [11].

2. EXPERIMENTAL

Polycrystalline $YMnO_3$ was prepared using a solid state reaction. The starting materials of Y_2O_3 and MnO_2 with 99.99% purity were mixed and grounded and then treated at 1000–1200°C in air for at least 70 h with several intermediate grindings. The phase purity of the compound was checked with a conventional *x*-ray diffractometer (SIEMENS D500). The powder was hydrostatically pressed in the form of rods (8 mm in diameter and ~60 mm in length). The rods were subsequently sintered at 1300°C for 30 h. The crystal growth was carried out using an optical floating zone furnace (FZ-T-

¶ This article was submitted by the authors in English.

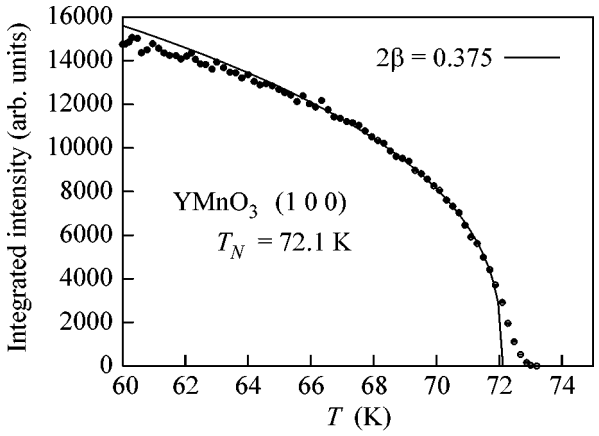

Fig. 1. Temperature dependence of the intensity of the (1 0 0) magnetic Bragg peak. The line is a fit to the data with a power law.

10000-H-IV-VP-PC, Crystal System Corp., Japan) with four 1000 W halogen lamps as a heat source. The growth rate was 1.5 mm/h and both rods (the feeding and seeding rod) were rotated at about 20 rpm in opposite directions to ensure the liquid homogeneity. A mixture of argon with 2% oxygen at 5.5 bar was applied during the growing. The crystal has the shape of a rod 6 mm in diameter and 2 cm in height and a mosaic spread better than 1°.

The measurements were performed at triple-axis TASP located on the cold source of the neutron spallation source SINQ. The sample was mounted inside an He-flow cryostat with the crystallographic axis a^* and c^* in the scattering plane. The spectrometer was operated with the energy of the scattered neutrons kept fixed at $k_f = 1.47$ Å^{-1} for measurements with unpolarized neutrons. 80' Soller collimators were installed in the incident beam and before the analyzer and the detector. With that configuration the energy resolution at zero energy transfer is 180 μeV. To reduce both the background and contamination by higher wavelength neutrons a cold Be filter was installed in the scattered beam. The inelastic polarized neutron measurements were performed at $k_f = 1.51$ Å^{-1} along $(1 \pm q, 0, 0.1)$ and at different temperatures above T_N. To perform longitudinal-polarization analysis, remanent supermirror benders [12] were inserted after the monochromator and before the analyzer. The orientation of the polarization was chosen perpendicular to the scattering plane. Because magnetic fluctuations with a polarization factor parallel to the neutron spin occur in the nonspin flip channel, the nonspin flip data (NSF) contains the in-plane fluctuations, and, in the spin-flip channel (SF), only out-of-plane fluctuations are present, as will be shown below.

3. RESULTS AND DISCUSSION

Figure 1 shows the intensity of the (1 0 0) magnetic Bragg reflection as a function of the temperature, which mirrors the square of the staggered magnetization. The transition temperature, as determined by taking the derivative of the magnetization curve [13], is $T_N = 72.1 \pm 0.05$ K. The intensity of the Bragg peak follows the power law $I \propto |(T/T_N - 1)|^{2\beta}$ with $\beta = 0.187(2)$. This value is lower than that reported for the case of typical stacked-triangular antiferromagnet $RbNiCl_3$ ($\beta = 0.28$), $CsNiCl_3$ ($\beta = 0.28$), and $CsMnBr_3$ ($0.21 < \beta < 0.25$) and close to the critical exponent obtained in VCl_2 ($\beta = 0.20$) [5, 14]. Typical 2D *XY*-antiferromagnets ($BaNi_2(PO_4)_2$) or ferromagnets (Rb_2CrCl_4, K_2CuF_4) have a magnetization exponent that corresponds to the expected theoretical value $\beta = 0.23$ [15]. We note that $\beta = 0.19$ in the 3D triangular Ising antiferromagnet [16].

Figure 2a shows elastic scans along the [1 0 *l*] direction as a function of temperature. Close to the Néel temperature, correlations between adjacent hexagonal planes give rise to broad magnetic scattering along c^* that eventually appears to condense into the magnetic Bragg peak at T_N. From Fig. 2b, we see that this diffuse scattering is static on the time scale of our experiment and corresponds to slow fluctuations of in-plane character, as will be shown below. With increasing temperature, these correlations disappear and only scattering across the [1 0 *l*] direction show a peak in the neutron cross section. Hence, well above T_N, correlations persist only between the Mn moments located in the hexagonal plane, as shown in Fig. 3. Here, we describe the line shape of the diffuse intensity by a Lorentzian profile convoluted with the resolution function of the spectrometer:

$$\chi_c(\mathbf{Q}) = \frac{\chi_0}{\pi}\frac{\kappa_\parallel^2}{(\mathbf{q}_\parallel - \mathbf{Q}_0) + \kappa_\parallel^2}\frac{\kappa_\perp^2}{(\mathbf{q}_\perp - \mathbf{Q}_0)^2 + \kappa_\perp^2}\delta(\omega), \quad (1)$$

where $\mathbf{Q}_0$ is the position of the magnetic rod in reciprocal space, $\parallel$ and $\perp$ denote the direction along and perpendicular to the magnetic rod, and $\kappa_\parallel$ denotes the inverse of the correlation length ξ between Mn spins in the hexagonal plane. Close to the Néel temperature, the temperature dependence of ξ behaves similar to $\xi(T) = 0.038(\pm 0.005)(T - T_N)^\nu$ with $\nu = 0.57(\pm 0.06)$ as shown in Fig. 3b. We now turn to the behavior of the paramagnetic fluctuations in $YMnO_3$. Figure 4 shows typical energy scans performed at $\mathbf{Q} = (1 - q, 0, -3.8)$ and $T = 73.6$ K. The inelastic cross-section for an unpolarized neutron beam is given by

$$\frac{d^2\sigma}{d\Omega d\omega} \propto \sum_{\alpha\beta}(\delta_{\alpha\beta} - \hat{Q}_\alpha\hat{Q}_\beta)S^{\alpha\beta}(\mathbf{Q}, \omega), \quad (2)$$

where $\delta_{\alpha\beta}$ is the Kronecker symbol; α, β are the Cartesian coordinates *x*, *y*, *z*, ($\mathbf{Q}$, ω) that denote the momen-

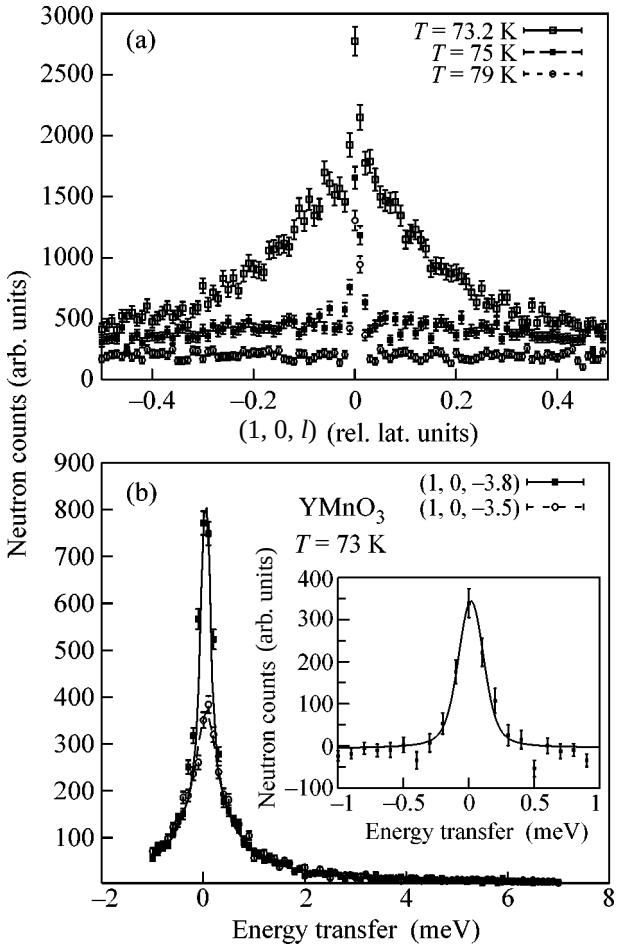

Fig. 2. (a) Elastic scans along (1, 0, *l*) that show the increase of diffuse magnetic scattering in $YMnO_3$ when the temperature approaches T_N. (b) Inelastic scan that shows the presence of the central peak in $YMnO_3$. The insert shows the difference between scans measured at (1, 0, –3.8) and (1, 0, –3.5) that emphasizes the resolution-limited component.

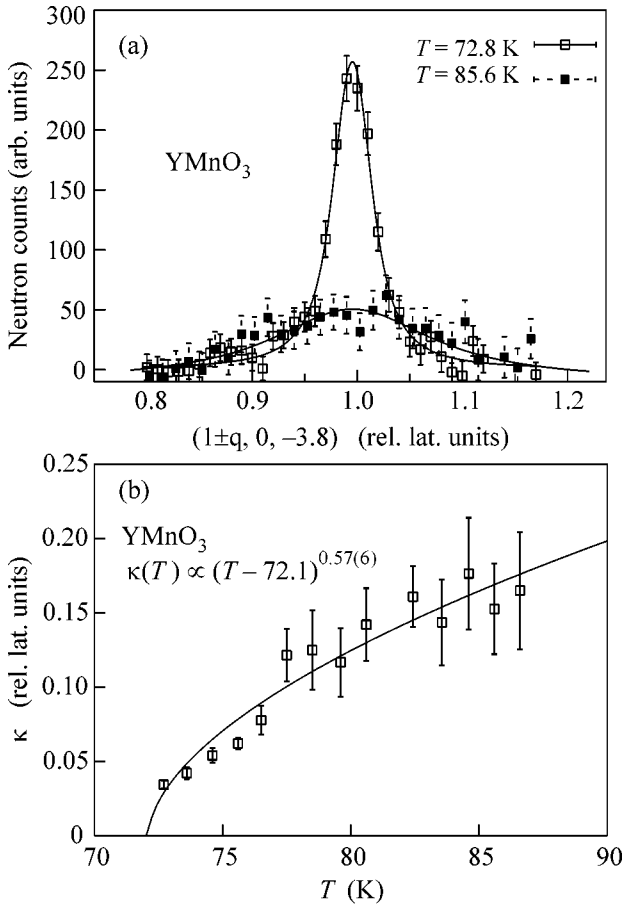

Fig. 3. (a) Neutron diffuse intensity in $YMnO_3$. The background was measured at $T = 300$ K and has been subtracted. (b) Temperature dependence of the inverse of the correlation length. The line is a fit to the data with a power law.

tum and energy transfers from the neutron to the sample; and $\hat{Q} = \mathbf{Q}/|\mathbf{Q}|$. The first term in Eq. (2) is a selection rule that implies that only spin components perpendicular to the scattering vector contribute to the neutron scattering cross section. Hence, for scattering vectors with large l components such as $\mathbf{Q} = (1 \pm q, 0, -3.8)$, the inelastic spectrum contains essentially paramagnetic fluctuations with in-plane character (||). In addition, close to the Néel temperature, inelastic scans through the magnetic rod show the resolution-limited central peak described by Eq. (1) as shown in Fig. 2. Thus, to analyze the data shown in Fig. 4, we modeled the inelastic intensity $I(\mathbf{Q}, \omega)$ in the following way:

$$I(\mathbf{Q}, \omega) = (S^{\parallel}_{\text{para}}(\mathbf{Q}, \omega) + S_{\text{inc}}(\omega) + S\chi_c(\mathbf{Q})) \otimes R(\mathbf{Q}, \omega) + Bck, \quad (3)$$

where $S_{\text{inc}} = A\delta(\omega)$ refers to the resolution-limited incoherent scattering that was measured at high temperature and S is a scale factor. The neutron scattering function $S^{\parallel}_{\text{para}}(\mathbf{Q}, \omega)$, which is related to the imaginary part of the dynamical susceptibility through $\pi(g\mu_B)^2 S^{\parallel}_{\text{para}}(\mathbf{Q}, \omega) = F^2(Q)(1 - \exp(-\hbar\omega/k_BT))^{-1}\Im\chi''(\mathbf{Q}, \omega)$, describes the line shape of the paramagnetic scattering as a function of momentum ($\mathbf{Q}$) and energy ($\hbar\omega$) transfer, respectively; $F(Q)$ is the magnetic form factor of Mn. In Eq. (3), the symbol $\otimes$ stands for the convolution with the spectrometer resolution function $R(\mathbf{Q}, \omega)$ [17] and *Bck* denotes the background level. We find that a Debye-like quasi-elastic line shape for the imaginary part of the dynamical susceptibility

$$\Im\chi''(\mathbf{Q}_0 + \mathbf{q}, \omega) = \omega\chi(\mathbf{Q}_0 + \mathbf{q})\frac{\Gamma(\mathbf{q})}{\omega^2 + \Gamma(\mathbf{q})^2} \quad (4)$$

reproduces the data adequately. $\chi(\mathbf{q})$ is the static susceptibility as in Eq. (1) taken relative to the antiferromagnetic zone center ($\mathbf{Q}_0 = (1, 0, 0)$), and $\Gamma(\mathbf{q})$ is the damping of the paramagnetic fluctuations. Figure 4

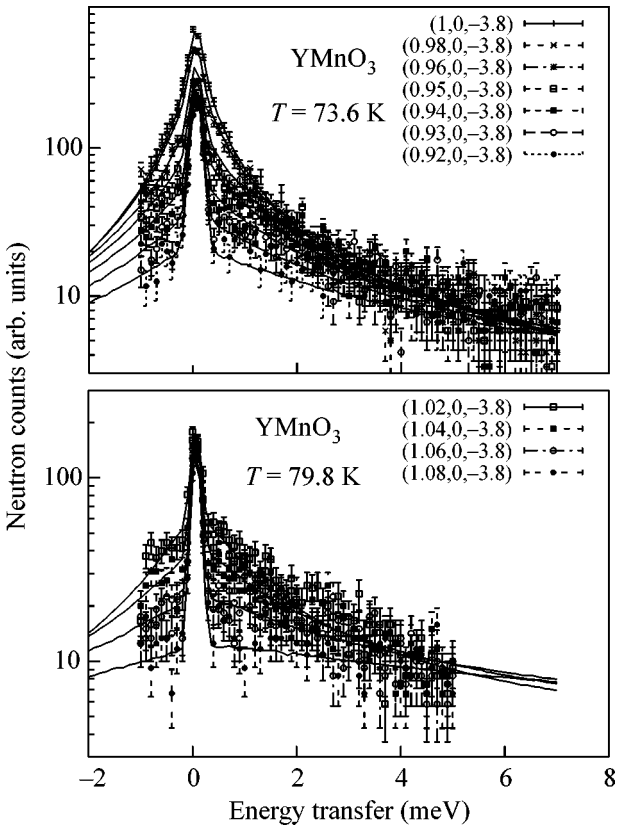

Fig. 4. Constant q-scans in $YMnO_3$ at $T = 73.6$ K and 79.8 K that show the in-plane fluctuations, as explained in the text. The lines are the result of fit to the data using Eq. (3).

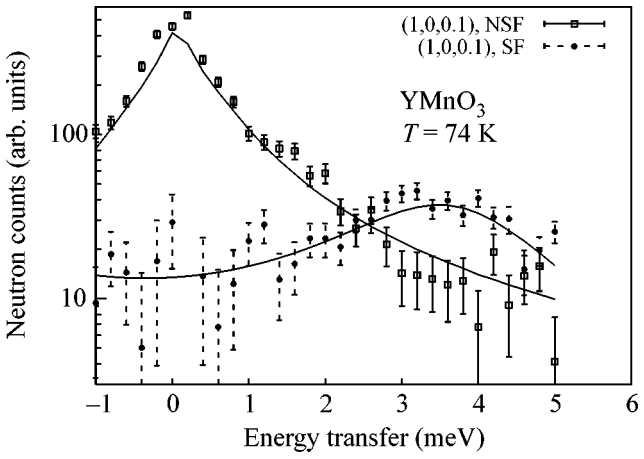

Fig. 5. Constant q-scans in $YMnO_3$ at $T = 73.6$ K that show the in-plane fluctuations in the non-spin flip (NSF) and the out-of-plane component in the spin-flip channel (SF), respectively. The lines are the result of fit to the data as described in the text.

shows the results of fits to the data at $T = 73.6$ K from which we extract that the damping of the in-plane fluctuations $\Gamma(\mathbf{q})$ evolves similar to $\Gamma(0, T) + (1450 \pm 90)q^z$ (meV) with $\Gamma(0, 73.6\text{ K}) = 0.23 \pm 0.07$ (meV), and $z = 2.26 \pm 0.07$. In contrast with data taken around $(1 \pm q, 0, 3.8)$, the inelastic spectra around $(1 \pm q, 0, 0.1)$ cannot be fitted with Eq. (4). This is an indication that the spectrum of paramagnetic fluctuations in $YMnO_3$ consists of 2 modes, an in-plane (||) as well as an out-of-plane component ($\perp$). To separate the || from the $\perp$ fluctuations, it is necessary to use polarization analysis. A typical inelastic spectrum measured with polarization analysis is shown in Fig. 5 that reveals an out-of-plane excitation in the spin-flip channel. In contrast with the || fluctuations, the $\perp$ component is inelastic and is best described by a damped-harmonic oscillator function

$$S^{\perp}_{DHO} \propto \frac{\omega}{1 - \exp(-\omega/T)} \frac{\gamma_q}{(\omega^2 - \Omega_q^2)^2 + \omega^2\gamma_q^2}, \qquad (5)$$

where Ω_q is the renormalized frequency and γ_q the damping of the excitation. Within the precision of the measurements, we find that $\Omega_q = 3.9 \pm 0.3$ (meV) and $\gamma_q = 2 \pm 0.5$ (meV) in the range of momentum values reached in the present experiment ($q \leq 0.1$).

The analysis of the data in the non-spin-flip channel yields the same q dependence for the || fluctuations that was obtained with the unpolarized set up. The results are summarized in the table. The mean value for the dynamical exponent of the || fluctuations in $YMnO_3$ yields $z \sim 2.3$ and does not agree with the theoretical dynamical exponent $z = 1$ for the classical 2D triangular antiferromagnet [18]. Also, the value obtained in $YMnO_3$ is quite different from the dynamical exponents $z = 1.5$ expected for the 3D Heisenberg antiferromagnet and measured, e.g., in $RbMnF_3$ [19] and $CsMnBr_3$ [20]. Finally, we show the temperature dependence of $\Gamma(0, T)$ in Fig. 6, which increases almost linearly above T_N, $\Gamma(0, T) = 0.4 + 0.07(T - T_N)^{1.1 \pm 0.2}$.

Parameter values for the damping ($\Gamma(\mathbf{q}) = \gamma q^z$ (meV)) and the critical exponent (z) of the ||-fluctuation in $YMnO_3$

	T(K)	γ	$\Delta\gamma$	z	Δz
Unpol.	73.6	1450	90	2.26	0.07
	79.8	1283	272	2.29	0.16
Pol.	74	1306	277	2.53	0.25
	78	1028	313	2.40	0.4

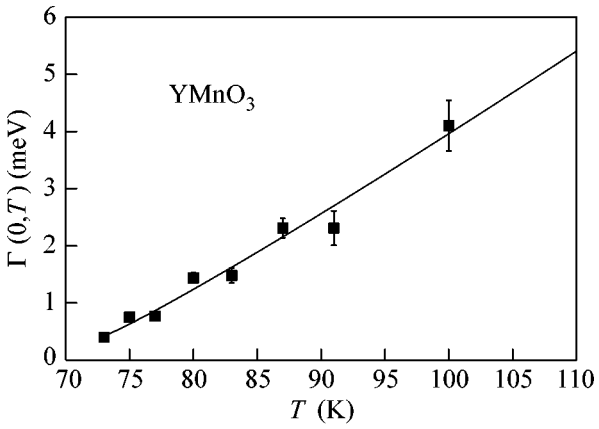

Fig. 6. Temperature dependence of the damping of the paramagnetic fluctuations with in-plane polarization as measured with polarized neutrons. The line is a fit to the data as explained in the text.

4. CONCLUSIONS

To conclude, using both unpolarized and polarized inelastic neutron scattering, we showed that there are two magnetic excitations in the paramagnetic regime of $YMnO_3$ that have in-plane and out-of-plane polarization, respectively. The in-plane mode has a resolution-limited central peak and a quasi-elastic component with a line width that increases as a function of momentum transfer q similar to $\propto q^z$ with the dynamical exponent $z = 2.3$. The presence of two time scales in the spectrum of in-plane fluctuations might be the signature for the coexistence of 2D and 3D fluctuations in the vicinity of T_N [21]. The out-of-plane fluctuations are inelastic at the magnetic zone center and do not show any q dependence for small wave vectors.

This work was performed at the Neutron Spallation Source SINQ, Paul Scherrer Institut, Switzerland and was partly supported by the NCCR MaNEP project.

REFERENCES

1. B. Bertaut and M. Mercier, Phys. Lett. **5**, 27 (1963).
2. A. Munoz, J. A. Alonso, M. J. Martínez-Lope, *et al.*, Phys. Rev. B **62**, 9498 (2000).
3. Junghwan Park, J.-G. Park, Gun Sang Jeon, *et al.*, Phys. Rev. B **68**, 104426 (2003).
4. T. J. Sato, S. H. Lee, T. Katsufuji, *et al.*, Phys. Rev. B **68**, 014432 (2003).
5. For a recent review see H. Kawamura, J. Phys.: Condens. Matter **10**, 4707 (1998).
6. T. E. Mason, B. D. Gaulin, and M. F. Collins, Phys. Rev. B **39**, 586 (1989).
7. V. P. Plakhty *et al.*, Europhys. Lett. **48**, 215 (1999); Phys. Rev. Lett. **85**, 3942 (2000).
8. V. P. Plakhty, W. Schweika, Th. Brückel, *et al.*, Phys. Rev. B **64**, 100402 (2001).
9. Z. J. Huang *et al.*, Phys. Rev. B **56**, 2623 (1997); T. Katsufuji *et al.*, Phys. Rev. B **64**, 104419 (2001).
10. T. Kimura *et al.*, Nature **426**, 55 (2003); D. V. Efremov *et al.*, Nat. Mater. **3**, 853 (2004); B. Lorenz *et al.*, Phys. Rev. Lett. **92**, 087204 (2004).
11. G. Laws, A. P. Ramirez, C. M. Varma, *et al.*, Phys. Rev. Lett. **91**, 257208 (2003).
12. F. Semadeni, B. Roessli, and P. Böni, Physica B (Amsterdam) **297**, 152 (2001).
13. A. D. Bruce, J. Phys. C **14**, 193 (1982).
14. M. F. Collins and O. A. Petranko, Can. J. Phys. **75**, 605 (1997).
15. S. T. Bramwell and P. C. W. Holdsworth, J. Phys.: Condens. Matter **5**, L53 (1993).
16. O. Heinonen and R. G. Petschek, Phys. Rev. B **40**, 9052 (1989).
17. M. Popovichi, Acta Crystallogr. A **31**, 507 (1975).
18. Kwangsik Nho and D. P. Landau, Phys. Rev. B **66**, 174403 (2002).
19. R. Coldea, R. A. Cowley, T. G. Perring, *et al.*, Phys. Rev. B **57**, 5281 (1998).
20. T. E. Mason, Y. S. Yang, M. F. Collins, *et al.*, J. Magn. Magn. Mater. **104–107**, 197 (1992).
21. L. P. Regnault, C. Lartigue, J. F. Legrand, *et al.*, Physica B (Amsterdam) **156–157**, 298 (1989); A. R. Völkel, A. R. Bishop, F. G. Mertens, *et al.*, J. Phys.: Condens. Matter **4**, 9411 (1992).

JETP Letters, Vol. 81, No. 6, 2005, pp. 292–295. Translated from Pis'ma v Zhurnal Éksperimental'noĭ i Teoreticheskoĭ Fiziki, Vol. 81, No. 6, 2005, pp. 356–359.

Effect of the Spin Short-Range Order on Electron Transport and Neutron Scattering in Amorphous Alloys Gd_xSi_{1-x}

N. K. Chumakov, V. V. Tugushev, S. V. Gudenko, O. A. Nikolaeva, V. N. Lazukov, I. N. Goncharenko, and P. A. Alekseev

Russian Research Center Kurchatov Institute, pl. Kurchatova 1, Moscow, 123182 Russia

e-mail: chumakov@imp.kiae.ru

Received February 24, 2005

Direct experimental evidence has been obtained for the existence of short-range ferromagnetic order in Gd_xSi_{1-x} alloys. Along with the standard magnetotransport measurements, a "local" experimental method of the elastic scattering of thermal neutrons on the magnetic moment of Gd is applied. The measurement results provide the conclusion that short-range ferromagnetic order is formed in nanoclusters with an increased content of Gd ions. We consider the amorphous alloy Gd_xSi_{1-x} as a new magnetic material with unique properties characteristic of both strongly inhomogeneous alloys and nanocomposite compounds. © *2005 Pleiades Publishing, Inc.*

PACS numbers: 72.15.Gd, 75.25.+z, 75.47.De, 75.50.–y

1. INTRODUCTION

Amorphous alloys Gd_xSi_{1-x} ($0.1 < x < 0.2$) have been actively studied and discussed in recent years. When the temperature and magnetic field vary, electron and magnetic phase transformations occur in these alloys and giant negative magnetoresistance is observed. The standard classification of these materials among completely disordered magnetic semiconductors appeared to fail to explain the anomalies in their transport and magnetic properties over wide ranges of temperatures and magnetic fields.

It follows from experiments [1, 2] that, in Gd_xSi_{1-x} alloys, doping effects that are responsible for the metal–insulator transition in disordered materials are in complex combination with the spin-correlation effects that are responsible for both the short-range order in disordered magnetic materials and transition to the spin-glass phase. For $T > 50$ K, the temperature dependence of the conductivity $\sigma(T)$ of Gd_xSi_{1-x} is the same as in its nonmagnetic structure analogue Y_xSi_{1-x}. For $T < 50$ K, negative magnetoresistance appears and the conductivity decreases much faster with temperature than the conductivity of Y_xSi_{1-x}. In the framework of the model of the Mott–Anderson transition that is induced by magnetic disorder, Kumar and Majumdar [3] attempted to qualitatively describe such a situation, but that work has not provided a complete understanding of the properties of real materials.

As was shown in [4], the change in conductivity under the variation of the temperature and magnetic field is primarily caused by a change in the concentration of free carriers. When the temperature decreases below a certain critical value $T_c \approx 50$–70 K, the magnetic susceptibility increases sharply and this increase is accompanied by a shift of the spin resonance line. These results provided the assumption that the system contains nanometer objects in which the ferromagnetic resonance occurs due to magnetic ordering for $T < T_c$. In [5, 6], a fundamental statement is formulated that structural and magnetic disorder in Gd_xSi_{1-x} alloys is more complex than was traditionally expected previously. Namely, in addition to ordinary "microscopic" fluctuations (at a scale of several interatomic distances) of the content, there are "nanoscopic" fluctuations (at a scale of ten or more interatomic distances) of the content. The latter fluctuations are nanoclusters (nanoclusters) with an increased content of Gd ions and strong ferromagnetic short-range order. Around these nanoclusters, regions with an increased electron density ("droplets") are formed and they play an important role in the transport properties of the system. An adequate theoretical model has been developed and numerous magnetic, transport, and magnetotransport measurements have indirectly corroborated the hypothesis of the formation of ferromagnetic droplets below T_c. The features of the transport and magnetic properties of Gd_xSi_{1-x} alloys have been successfully interpreted. In particular, giant negative magnetoresistance was attributed both to the orientation of the magnetic moments of individual nanoclusters and to lowering of the threshold of the flowing of the system in the external magnetic field, and an increase in the magnetic susceptibility when the temperature decreases was attributed to the superparamagnetic behavior of nanoclusters.

In this work, direct experimental evidence has been obtained for the appearance of local ferromagnetic order in Gd_xSi_{1-x} alloys. In order to observe nanoclus-

ters and to determine their magnetic state, a "local" experimental method of the elastic scattering of thermal neutrons on the magnetic moment of Gd is applied along with the standard magnetotransport measurements.

2. MAGNETOTRANSPORT PROPERTIES

The magnetotransport measurements for amorphous films of Gd_xSi_{1-x} approximately 1000 Å in thickness, which were prepared at the laboratory headed by Prof. F. Hellman by the method of joint deposition by an electron beam [2], were carried out in the temperature range 5–300 K and in magnetic fields to 40 kG. The magnetic-field dependences were measured for transverse R_{xx} and Hall R_{xy} magnetoresistances in van der Pauw geometry for various temperatures. Before analyzing the measurement results, it is necessary to make one remark.

We assumed that the conductivity in the system under study is primarily ensured by electrons moving in wide bands formed by *s–p* hybridized orbitals of Si. According to [7], Gd enters into the matrix of amorphous Si in the form of a trivalent ion that closes broken bonds between two neighboring Si ions and gives electrons of its outer *s–d* shells to these bonds. Owing to such a specificity of the chemical bond in *a*-Gd_xSi_{1-x}, the anomalous contribution to R_{xy} due to the spin–orbit interaction between band *s–p* states of Si and localized *f* states of Gd is likely insignificant. For this reason, we will take into account only the normal component of R_{xy} and assume that the components of the tensors (R_{xx}, R_{xy}) are related to the free-carrier concentration and the average magnetic field B_{in} inside the current-flowing regions as $1/R_{xx} \propto n$ and $R_{Hall} = R_{xy}/B_{in} \propto 1/n$.

Under this assumption, the dependence of $B_{in} \propto R_{xy}/R_{xx}$ on the external magnetic field H can be plotted in arbitrary units (see Fig. 1). It is seen that the dependence $B_{in}(H)$ is strongly nonlinear as a whole. However, in the region $H > 20$ kG, it is almost linear and contains a constant contribution that, as we believe, is attributed to the saturation magnetization M_s^{exp} of the sample. Taking into account the saturation of the magnetization in strong magnetic fields, we normalize the slope of the dependence $B_{in}(H)$ ($H > 20$ kG) to unity and thereby determine the absolute value of B_{in}. This method makes it possible to estimate the magnetization of the material, and it serves as a Hall magnetometer sensitive to the local magnetization of the material in the current-flowing region. From the relation $B_{in}(H > 20) \simeq H + 4\pi M_s^{exp}$, we obtain the rough estimate $M_s^{exp} \simeq 2$ kG. As is easily seen, this value significantly exceeds the theoretical estimate of the saturation magnetization under the assumption of the uniform distribution of Gd atoms over the sample volume: $M_s^{theor} = N_m \mu_B sg \simeq 450$ G,

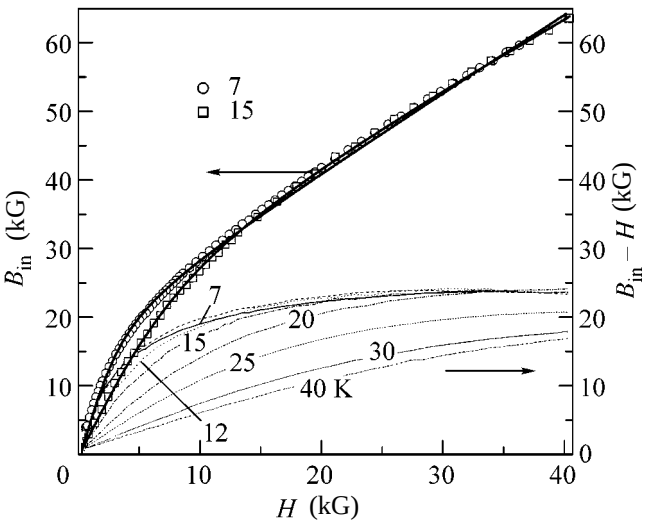

Fig. 1. Local magnetic field and magnetization inside current-flowing regions vs. the external magnetic field in the $Gd_{0.145}Si_{0.855}$ sample for various temperatures. The line is the approximation by function (2).

where $N_m = 7 \times 10^{21}$ cm^{-3} is the average Gd concentration corresponding to the content of $Gd_{0.14}Si_{0.86}$, μ_B is the Bohr magneton, $s = 7/2$ is the spin of the Gd^{3+}, and $g = 2$ is the spectroscopic-splitting factor of the Gd^{3+} ions. Thus, the simplest interpretation of the experimental results is not obvious, and a finer analysis of the situation is necessary.

Taking into account a conclusion made in [8] that the metal–insulator transition in Gd_xSi_{1-x} is of percolation character, we assume that the conductivity in the material under investigation occurs through the circuit that is formed by nanoclusters inside which Gd spins are ferromagnetically ordered. The average magnetic field for the current that flows over nanoclusters in a thin-film sample in the presence of the external magnetic field H perpendicular to the film plane is given by the expression

$$\begin{aligned} B_{in} &= H_{in} + (4\pi - \langle N_c \rangle) M_c \\ &= H - (4\pi - 4\pi/3) f M_c + (4\pi - \langle N_c \rangle) M_c. \end{aligned} \quad (1)$$

Here, H_{in} is the magnetic field averaged over the nanocluster volume, f is the volume fraction of the nanoclusters, $\langle N_c \rangle$ is the average demagnetization coefficient, $M_c = M_{cs}\mathcal{L}(K\mu_B sgH_{in}/k_BT)$ is the average magnetization of the nanoclusters along the field, $M_{cs} = N_c\mu_B sg$ is the saturation magnetization of the nanoclusters, K is the number of Gd ions in the nanoclusters, N_c is the concentration of Gd ions in the nanoclusters, $\mathcal{L}(y) = \coth(y) - 1/y$ is the Langevin function, and k_B is the Boltzmann constant.

For chaotically oriented clusters that are not too anisotropic in shape, the approximation $\langle N_c \rangle \approx 4\pi/3$ can

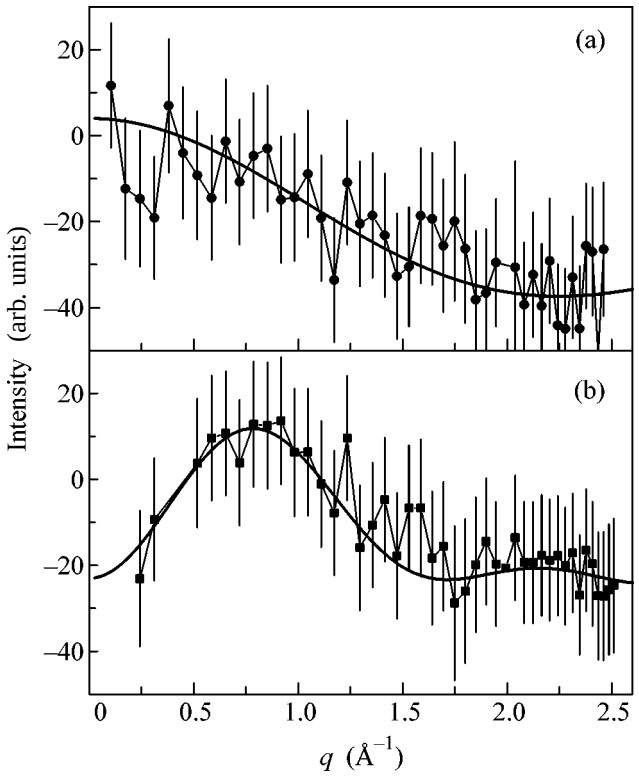

Fig. 2. Magnetic neutron diffraction patterns of the $Gd_{0.14}Si_{0.86}$ sample for temperatures of (a) 4.2 and (b) 1.7 K. The lines are the approximations by the functions (a) $F(q) = A + B\sin(rq)/rq$, where r = 2 Å, and (b) $F(q) = A + B\sin(r_1q)/r_1q + C(1 - \sin(r_2q)/r_2q)$, where r_1 = 2 and r_2 = 5 Å.

be used, and, taking into account that $f \ll 1$ (since $f < x$, measurements were carried out on Gd_xSi_{1-x} samples for x = 0.1–0.2), we obtain $H_{in} \approx H$. In this case, formula (1) assumes the form

$$B_{in} \simeq H + \frac{8\pi M_c}{3} \simeq H + \frac{8\pi M_{cs}}{3}\mathcal{L}\left(\frac{K\mu_B sgH}{k_B T}\right). \quad (2)$$

The solid lines in Fig. 1 are plotted according to formula (2) with optimally fitted parameters M_{cs} and K. It is seen that experimental dependences $B_{in}(H)$ are well approximated by the model of the current that flows through ferromagnetic nanoclusters. A value of $M_{cs} \approx$ 2.8 kG is obtained for the saturation magnetization, and, when the temperature decreases, K increases gradually and smoothly approaches the value $K \approx$ 10–15. This behavior implies that the local concentration of Gd atoms in the network that is formed by nanoclusters in which the current flows is higher than N_m by a factor of approximately 6. Taking into account the range of possible values of the demagnetization factor $\langle N_c\rangle$ = 0–2π, we estimate the maximum and minimum concentrations of Gd atoms in nanoclusters on the flowing paths as $N_{cs} \approx (2–4) \times 10^{22}$ cm^{-3}. Knowing the mean number $K \approx$ 10–15 of Gd atoms in a cluster, one can determine its characteristic volume as ≈300–800 Å^3. We note that the saturation magnetization is approximately the same in samples with significantly different contents. Therefore, the densities of Gd atoms in ferromagnetic nanoclusters are also nearly the same. The mean spacing between Gd atoms in nanoclusters is approximately equal to 3 Å, which is close to the lattice parameter in $GdSi_2$ crystals. These circumstances provide an assumption on the chemical nature of ferromagnetic nanoclusters. Ferromagnetic nanoclusters are possibly $GdSi_2$ inclusions formed during the material synthesis.

3. NEUTRON DIFFRACTION

The assumptions that were based on magnetotransport measurements are corroborated by the results of the neutron-diffraction experiment that was carried out in order to reveal the local ferromagnetic order. In order to obtain the material amount necessary for the neutron experiment, a $Gd_{0.14}Si_{0.86}$ sample 1.3 μm thick was grown on an NaCl crystal substrate. The material that was formed after the dissolution of the substrate was studied using neutron measurements on a G6.1 high-flux neuron diffractometer mounted at the ORPHEE reactor (Laboratory Leon Brillouin, Sacley, France). The measurements were carried out with 4.741-Å (3.6-meV) incident neutrons in the scattering angle range 2θ = 5°–140° and for the temperatures T = 1.7, 4.3, 15, 40, and 80 K. The chosen scattering angles correspond to the neutron momentum transfer q = 0.25–2.5 Å^{-1}. This choice allows the determination of the magnetic correlation regions in the range 3–30 Å. The magnetic-diffraction data for low temperatures were obtained by the subtraction of the data that were obtained at a temperature of T = 80 K (below which correlations between magnetic Gd ions appear) from the corresponding diffraction pattern.

Figure 2 shows the results thus obtained for T = 1.7 and 4.2 K. For these temperatures, the modulation of the magnetic signal is observed in the dependence on the wave vector. This modulation changes significantly when the temperature increases, and the magnetic scattering was not observed for T = 15 K. Only ferromagnetic correlations are observed between Gd ions for T = 4.2 K. From the approximation by the function $F(q) = A + B\sin(rq)/rq$, where r = 2 Å, the ferromagnetic correlation length is estimated as ≈5 Å for a distance of about 2 Å between Gd ions. The data obtained for the lowest temperature, T = 1.7 K, exhibit the existence of antiferromagnetic correlations. At the same time, the best fit is obtained under the assumption that antiferromagnetic correlations coexist with ferromagnetic correlations. The use of the function $F(q) = A + B\sin(r_1q)/r_1q + C(1 - \sin(r_2q)/r_2q)$, where r_1 = 2 Å and r_2 = 5 Å, made it possible to estimate the antiferromagnetic correlation length as ≈15 Å. This result can be treated as the appearance of antiferromagnetic correlations between ferromagnetic droplets.

Thus, these data provide direct experimental evidence that droplets with short-range ferromagnetic correlations really exist in the sample for $T < 15$ K and increase the magnetization.

The considerable decrease in the magnetization that is observed for the lowest temperature ($T < 2$ K) is associated with antiferromagnetic correlations between ferromagnetic droplets. Analysis of the intensity of the elastic magnetic scattering of neutrons provides a conclusion that nearly all Gd ions are involved in antiferromagnetic correlations.

4. CONCLUSIONS

We think that the amorphous compound Gd_xSi_{1-x} is a new magnetic material with unique properties characteristic of both strongly inhomogeneous alloys and nanocomposite compounds. The system under consideration has percolation conductivity over the network of nanoconductors formed by ferromagnetic particles of nanometer sizes with a high concentration of Gd ions incorporated into the matrix of amorphous silicon with significantly lower concentration of Gd. The existence of regions with a high concentration of Gd, as well as the local ferromagnetic order in them, is corroborated by the experiments on the diffraction of thermal neutrons and the Hall effect, as well as by the self-consistent numerical simulation [5, 6].

We are grateful to V.B. Preobrazhenskiĭ, A.V. Inyushkin, A.N. Taldenkov, V.V. Ryl'kov, and V.I. Ozhogin for assistance and stimulating discussions and to F. Hellman for the preparation of the samples and critical remarks. This work was supported by the US Civilian Research and Development Foundation for the Independent States of the Former Soviet Union (grant no. RP2-2402-MO-02), the Russian Foundation for Basic Research (project no. 03-02-17467), and the Council of the President of the Russian Federation for Support of Young Russian Scientists and Leading Scientific Schools (project no. NSh-2037.2003.2).

REFERENCES

1. F. Hellman, M. Q. Tran, A. E. Gebala, *et al.*, Phys. Rev. Lett. **77**, 4652 (1996).
2. W. Teizer, F. Hellman, and R. C. Dynes, Phys. Rev. Lett. **85**, 848 (2000).
3. S. Kumar and P. Majumdar, Int. J. Mod. Phys. B **15**, 2683 (2001).
4. N. K. Chumakov, S. V. Gudenko, V. V. Tugushev, *et al.*, J. Magn. Magn. Mater. **272–276**, 1351 (2004).
5. S. Caprara and V. V. Tugushev, Microelectron. Eng. (2005) (in press).
6. S. Caprara, V. V. Tugushev, and N. K. Chumakov, Zh. Éksp. Teor. Fiz. (2005) [JETP (2005)] (in press).
7. M. Sercheli, C. Rettori, and A. Zanatta, Braz. J. Phys. **32**, 409 (2002).
8. L. Bokacheva, W. Teizer, F. Hellman, and R. C. Dyne, Phys. Rev. B **69**, 235 111 (2004).

Translated by R. Tyapaev

JETP Letters, Vol. 81, No. 6, 2005, pp. 296–297. From Pis'ma v Zhurnal Éksperimental'noĭ i Teoreticheskoĭ Fiziki, Vol. 81, No. 6, 2005, pp. 360–361.

Comment on "Order Parameter of *A*-like ^{3}He Phase in Aerogel"¶

V. P. Mineev and M. E. Zhitomirsky

Commissariat á l'Energie Atomique, DSM/DRFMC/SPSMS 38054 Grenoble, France

e-mail: mineev@drfmc.ceng.cea.fr

Received February 24, 2005

We argue that the inhomogeneous *A* phase in aerogel is energetically more preferable than the "robust" phase suggested by Fomin [5]. © *2005 Pleiades Publishing, Inc.*

PACS numbers: 67.57.–z

Experimental investigation of the superfluid phases of ^{3}He in aerogel is at present a hot subject in low temperature physics (see the most recent publications [1, 2] and references therein). In view of its anisotropic properties, special interest has been attracted to the *A*-like superfluid phase. As was pointed out by Volovik [3], such a phase corresponds at short-length scale to the ordinary *A*-phase, while, at larger distances, it represents a kind of superfluid glass with irregular distribution of the direction of Cooper pairs angular momentum and absence of superfluid properties. Volovik's derivation was based on the general analysis of Imry and Ma of phase transitions with breaking of a continuous symmetry in the presence of random local anisotropy [4]. Recently, Fomin published a series of papers [5–7] where he claimed that "the general argument of Imry and Ma does not directly apply to the superfluid ^{3}He in aerogel." He introduced anisotropic interaction of the superfluid ^{3}He with aerogel

$$F_\eta = \int \eta_{ij}^{(a)}(\mathbf{r}) A_{\mu i}(\mathbf{r}) A_{\mu j}^*(\mathbf{r}) d^3r, \quad (1)$$

where $A_{\mu i}$ is the superfluid order parameter and a traceless position-dependent tensor $\eta_{ij}^{(a)} = \eta_{ij} - \frac{1}{3}\eta_{ll}\delta_{ij}$ describes the local splitting of T_c for different projections of angular momenta because of anisotropic suppression of superfluidity by aerogel strands. The isotropic part of this tensor subtracted here is included in a term that produces a local shift of the critical temperature. Due to the time reversal invariance of the energy F_η, the tensor $\eta_{ij}^{(a)}$ obeys the symmetry $\eta_{ij}^{(a)} = \eta_{ji}^{(a)}$.

According to Fomin [7], the interaction (1) plays the role of the "surface" energy that is lost for any superfluid phase except for the case when there is an average value of the order parameter $\bar{A}_{\mu i}$ such that

$$\eta_{ij}^{(a)} \bar{A}_{\mu i} \bar{A}_{\mu j}^* = 0 \quad (2)$$

or, equivalently,

$$\bar{A}_{\mu i}\bar{A}_{\mu j}^* + \bar{A}_{\mu j}\bar{A}_{\mu i}^* \propto \delta_{ij}. \quad (3)$$

The above constraint removes the "surface" term $F_\eta \equiv 0$ and leads to the conclusion [7] that superfluid phases of ^{3}He in aerogel below the second order transition from the normal state should satisfy Eq. (3). The *B* phase with $A_{\mu i}^B = \Delta_B R_{\mu i} e^{i\varphi}$ does satisfy this condition; however, for the ordinary *A* phase, Eq. (3) is not fulfilled. The *A* phase order parameter is given by

$$A_{\mu i}^A = \Delta_A V_\mu (m_i + i n_i), \quad (4)$$

where a unit vector V_μ determines the orientation of the spin quantization axis, while two orthogonal vectors **m** and **n** yield the direction of the orbital momentum $\mathbf{l} = \mathbf{m} \times \mathbf{n}$. As a result, it has been proposed to consider, instead of the *A* phase, a class of so called "robust" phases satisfying Eq. (3) [5–7].

Let us, nevertheless, substitute the *A* phase order parameter into Eq. (1):

$$F_\eta = \Delta_A^2 \int \eta_{ij}^{(a)} [m_i(\mathbf{r}) m_j(\mathbf{r}) + n_i(\mathbf{r}) n_j(\mathbf{r})] d^3r. \quad (5)$$

Using the identity $m_i(\mathbf{r})m_j(\mathbf{r}) + n_i(\mathbf{r})n_j(\mathbf{r}) + l_i(\mathbf{r})l_j(\mathbf{r}) = \delta_{ij}$, we obtain

$$F_\eta = -\Delta_A^2 \int \eta_{ij}^{(a)} l_i(\mathbf{r}) l_j(\mathbf{r}) d^3r. \quad (6)$$

Any uniform state of the *A* phase has $F_\eta = 0$, since $\int \eta_{ij} d^3r = 0$. This is, actually, true for an arbitrary homogeneous phase that is effectively "robust" on average and has the same transition temperature as the states (3). The "nonrobust" *A* phase can further gain energy from long-scale fluctuations of the random anisotropy by adjusting the direction of vector **l** on a certain length-scale *L*. Consequently, we just return to the standard Imry–Ma picture described for application to the super-fluid ^{3}He by Volovik [3]. The only difference with the Imry–Ma scenario is that space variations

¶ This article was submitted by the authors in English.

of the vector $\mathbf{l}(\mathbf{r})$ do not destroy the phase transition: the complex superfluid order parameter $A_{\mu i}(\mathbf{r})$ breaks additional spin-rotational symmetry and, partly, the gauge symmetry [3]. Thus, the adjustment of vector $\mathbf{l}$ to the long-scale fluctuations of the anisotropic energy leads to an enhancement of the transition temperature of the generalized *A* phase compared to the critical temperature of the "robust" axiplanar state suggested by Fomin. The proper estimate of the domain-size *L* can be found in [3].

As for the superfluid properties, the randomness of the distribution of the $\mathbf{l}(\mathbf{r})$ vector does not destroy the superfluid flow in ^{3}He-*A* in aerogel. There is, in fact, just the opposite effect: fixing of the $\mathbf{l}$ direction prevents the phase slippage processes and makes the *A* phase in aerogel an even better superfluid than in the bulk.

In conclusion, there is no reason for the stability of the "robust" phases, which have a higher energy than the locally homogeneous (on length scale *L*) *A* phase.

REFERENCES

1. J. E. Baumgardner and D. D. Osheroff, Phys. Rev. Lett. **93**, 155301 (2004).
2. H. C. Choi, A. J. Gray, C. L. Vincente, *et al.*, Phys. Rev. Lett. **93**, 145302 (2004).
3. G. E. Volovik, Pis'ma Zh. Éksp. Teor. Fiz. **63**, 281 (1996) [JETP Lett. **63**, 301 (1996)].
4. Y. Imry and S. Ma, Phys. Rev. Lett. **35**, 1399 (1975).
5. I. A. Fomin, Pis'ma Zh. Éksp. Teor. Fiz. **77**, 285 (2003) [JETP Lett. **77**, 240 (2003)].
6. I. A. Fomin, J. Low Temp. Phys. **134**, 769 (2004).
7. I. A. Fomin, Zh. Éksp. Teor. Fiz. **125**, 1115 (2004) [JETP **98**, 974 (2004)]; cond-mat/0401639.

JETP Letters, Vol. 81, No. 6, 2005, p. 298. Translated from Pis'ma v Zhurnal Éksperimental'noĭ i Teoreticheskoĭ Fiziki, Vol. 81, No. 6, 2005, p. 362.

Answer to the Comment on "Order Parameter of A-Like ^{3}He Phase in Aerogel" by Mineev and Zhitomirsky

I. A. Fomin

Kapitza Institute for Physical Problems, Russian Academy of Sciences, ul. Kosygina 2, Moscow, 119334 Russia

Received February 28, 2005

The reasons that are presented by Mineev and Zhitomirsky are based on the unjustified neglect of the contribution from fluctuations to the free energy of superfluid ^{3}He in an aerogel. © *2005 Pleiades Publishing, Inc.*

PACS numbers: 67.57.–z

A random tensor field $\eta_{jl}(\mathbf{r})$ that is introduced in [C5–C7] (C stands for the references cited in the comment under discussion) induces spatial fluctuations of the order parameter. It is convenient to decompose the order parameter into two components as $A_{mj}(\mathbf{r}) = \bar{A}_{\mu j} + a_{mj}(\mathbf{r})$, where $\bar{A}_{\mu j} \neq 0$ is the mean value of the order parameter. In this case, the free energy of superfluid ^{3}He can be represented in the form of the sum

$$F = F_0(\bar{A}_{\mu j}) + F_{\text{fl}}(\bar{A}_{\mu j}, a_{\mu j}),$$

where $F_0(\bar{A}_{\mu j})$ is obtained by substituting $\bar{A}_{\mu j}$ into the Ginzburg–Landau functional and F_{fl} contains nonzero means of fluctuation additions $\overline{a_{\mu j}, a_{\nu e}}$, etc.

Mineev and Zhitomirsky ignore the presence of F_{fl} and, following argumentation by Imry and Ma [C4] and Volovik [C3], conclude that quasi-isotropic A-like phases that were proposed in [C5–C7] are energetically unfavorable. However, the fluctuation contribution to the energy is leading for the case under discussion. It is easy to verify this statement by estimating both contributions. The energy $F_0(\bar{A}_{\mu j})$ decreases due to the adjustment of the order parameter orientation to fluctuations of the random field at a certain scale L. This scale for superfluid ^{3}He-A was estimated by Volovik [C3] as $L \sim \xi_0/\eta^2$ in terms of the field η_{jl}. The energy F_0 decreases due to such an adjustment by $\delta F_0 \sim N(0)\tau T_c^2 \eta^4$, where $N(0)$ is the density of states and $\tau = (T_c - T)/T_c$.

When estimating the fluctuation contribution to the energy, it is necessary to distinguish fluctuations along directions in which the order parameter is degenerate and along directions perpendicular to them. The contribution from fluctuations of the second type does not differ in essence from the corresponding contribution for superconductors with the scalar order parameter ψ. If this order parameter is represented as the sum of the mean $\bar{\psi}$ and fluctuation addition ξ, then, according to Larkin and Ovchinnikov [1], $\overline{\xi^2} \sim \bar{\psi}^2(\eta^2/\sqrt{\tau})$ and the corresponding addition to the energy is $\delta F_\perp \sim N(0)\tau^{3/2} T_c^2 \eta^2$. Even this addition is larger than δF_0 by a factor of $\sqrt{\tau}/\eta^2$ (the condition $\eta^2/\sqrt{\tau} \ll 1$ is necessary for fluctuations of the order parameter to remain small compared to its mean value).

The contribution to the energy from fluctuations in the direction of the degeneracy of the order parameter includes an additional large factor of $\sim \frac{1}{\xi_0}\int \frac{dk}{k^2}$, where k is the wavenumber of the corresponding fluctuations. The integral diverging in the lower limit should be cut at a scale of l_Δ at which fluctuations of the order parameter are on the order of its value, i.e., $l_\Delta \sim \xi_0(\sqrt{\tau}/\eta^2)$. In this case, the fluctuation terms can compete with the fourth order terms in the energy $F_0(\bar{A}_{\mu j})$ and the equilibrium order parameter need not coincide with the minimum in $F_0(\bar{A}_{\mu j})$. A criterion that was proposed in [C5–C7] for choosing phases was the condition of the exclusion of diverging terms in fluctuation energy. This criterion ensures a much larger gain than that discussed in the comment. This criterion separates the family of quasi-isotropic A-like order parameters that are proposed as the zeroth approximation for the observed A-like phase.

Note that the exclusion of diverging terms for the vector order parameter that is used as an example by Imry and Ma [C4] is possible only when the mean order parameter vanishes. In view of the above discussion, the reasons that are presented by Mineev and Zhitomirsky in their comment do not provide the basis for the revision of the results obtained in [C5–C7].

I am grateful to E.I. Kats and D.E. Khmel'nitskiĭ for stimulating discussion and to Institute Laue–Langevin (Grenoble, France) for hospitality.

REFERENCES

1. A. I. Larkin and Yu. N. Ovchinnikov, Zh. Éksp. Teor. Fiz. **61**, 1221 (1971) [Sov. Phys. JETP **34**, 651 (1972)].

Translated by R. Tyapaev

0021-3640/05/8106-0298$26.00 © 2005 Pleiades Publishing, Inc.